

# ENERGY AND PARTICLE TECHNOLOGY LABORATORY

RESEARCH GROUP AT MECHANICAL ENGINEERING DEPARTMENT  
CARLETON UNIVERSITY

## Designing a Common Platform for Modelling Soot in Flames and Reactors

Author:  
Mohammad ADIB  
[moadib@cmail.carleton.ca](mailto:moadib@cmail.carleton.ca)

Supervisor: Dr. Reza Kholghy

Last time updated on:  
August 3, 2024

# Contents

<b>1</b>	<b>Introduction</b>	<b>11</b>
1.1	Motivation . . . . .	11
1.2	Background . . . . .	12
1.2.1	Soot inception and surface growth . . . . .	12
1.3	Coagulation and agglomeration . . . . .	15
1.4	Soot maturity and its optical properties . . . . .	17
1.5	Oxidation . . . . .	18
1.6	Research objectives . . . . .	18
<b>2</b>	<b>Theoretical Model</b>	<b>21</b>
2.1	Assumptions and conventions . . . . .	21
2.2	Flames . . . . .	22
2.3	Reactors . . . . .	23
2.3.1	Constant Volume Reactor . . . . .	23
2.3.2	Perfectly Stirred Reactor . . . . .	24
2.3.3	Plug Flow Reactor . . . . .	25
2.4	Particle Dynamics . . . . .	26
2.4.1	Soot Morphology . . . . .	26
2.4.2	Diffusion of soot particles . . . . .	28
2.4.3	Soot Composition . . . . .	28
2.4.4	Monodisperse Population Balance Model . . . . .	29
2.4.4.1	Coagulation . . . . .	29
2.4.4.2	Source terms . . . . .	29
2.4.5	Sectional Population Balance Model . . . . .	30
2.4.5.1	Coagulation . . . . .	30
2.4.5.2	Source terms . . . . .	32
2.5	Surface reactions model . . . . .	33
2.6	PAH growth models . . . . .	35
2.6.1	Irreversible Dimerization . . . . .	36
2.6.2	Reactive Dimerization . . . . .	37
2.6.3	Dimer Coalescence . . . . .	39
2.6.4	E-Bridge Formation . . . . .	41
2.7	Gas scrubbing rates . . . . .	43
<b>3</b>	<b>Results</b>	<b>44</b>
3.1	Validation . . . . .	44
3.1.1	Collision Frequency . . . . .	44
3.1.2	Coagulation . . . . .	45
3.1.3	Constant Volume Reactor . . . . .	47
3.1.4	Plug Flow Reactor . . . . .	48
3.2	Soot yield and morphology during methane pyrolysis in shock-tubes . . . . .	49
3.2.1	Experimental setup and data collection . . . . .	51

3.2.2	30% Methane Data-set . . . . .	51
3.2.3	10% Methane Data-set . . . . .	57
3.2.3.1	Reaction Mechanism Assessment . . . . .	57
3.2.3.2	Characterization of soot morphology in methane pyrolysis shock-tube	59
3.2.3.3	Modelling soot yield and morphology . . . . .	61
<b>A</b>	<b>Derivation of Transport Equations</b>	<b>80</b>
A.1	Constant Volume Reactor . . . . .	80
A.1.1	Continuity . . . . .	80
A.1.2	Species . . . . .	80
A.1.3	Energy . . . . .	81
A.1.4	Soot Variables . . . . .	82
A.2	Plug Flow Reactor . . . . .	83
A.2.1	Continuity . . . . .	83
A.2.2	Momentum . . . . .	83
A.2.3	Species . . . . .	84
A.2.4	Energy . . . . .	84
A.3	Perfectly Stirred Reactor . . . . .	85
A.3.1	Continuity . . . . .	85
A.3.2	Species . . . . .	86
A.3.3	Energy . . . . .	86
<b>B</b>	<b>Additional Results</b>	<b>89</b>
B.1	Methane pyrolysis data from Hanson Research Group . . . . .	89
B.1.1	30% CH <sub>4</sub> dataset . . . . .	89
B.1.2	10% CH <sub>4</sub> dataset . . . . .	100
B.2	Methane pyrolysis data of Agafonov et al. [1] . . . . .	103

# List of Figures

1.1	The TEM images of Carbon black (a & c) [13] and soot (b & d) [14, 15] that shows soot and CB has similar morphology and structure . . . . .	12
1.2	Standard enthalpy ( $\Delta H$ ) and entropy ( $T\Delta S$ ) contributions to Gibbs function of reaction $\Delta G$ at 1600 K for carbon formation from propane(reprinted from Ref. [21]) . . . . .	13
1.3	The range of time and length scales of the processes involved in soot formation from molecular reactions to particle-fluid interaction in flames . . . . .	14
1.4	The HRTEM image of (a) a nascent soot primary particle with disordered internal nanostructure juxtaposed with that of (b) a mature soot primary particle with well-organized cluster near the shell sampled from soot generated by pyrolysis of ethanol at 1250 and 1650, respectively. Reprinted from Ref.[100] . . . . .	17
1.5	The conceptual structure of developed process design tool that account for gas mixture properties, and soot chemistry involving inception, surface growth and oxidation as well as its coagulation leading to the fractal-like morphology of soot particles . . . . .	19
1.6	The timeline for the next steps of the project in 2024-2025 . . . . .	20
2.1	The schematics of control volume considered for the constant volume reactor that encompasses the gas mixture and excludes the soot particles. Mass and energy are transferred between gas and soot particles. . . . .	23
2.2	The schematics of control volume considered for the perfectly stirred reactor that encompasses the gas mixture and excludes the soot particles. Mass and energy are transferred between gas and soot particles. The inlet flow brings species and enthalpy into the control volume and the outflow discharges them. The outflow mass flow is less than inflow mass flow due to soot formation. . . . .	24
2.3	The schematics of control volume for a differential element along PFR that includes the gas mixture and excludes the soot particles considering wall heat transfer. Mass and energy are transferred between gas and soot. . . . .	25
2.4	The schematics of a soot agglomerates with 12 primary particles ( $n_p = 12$ ). Primary particle ( $d_p$ ), mobility ( $d_m$ ), and gyration ( $d_g$ ) are shown. . . . .	27
2.5	The illustration of sections of SPBM. The mass of sections grows progressively by the scale factor of SF. Inception introduces new particles to the first section that propagate to the upper section via coagulation and surface growth and return to lower sections by oxidation. Carbon and hydrogen pass from gas to solid phase through inception and surface growth and goes back via oxidation. . . . .	30
3.1	The comparison of collision frequency, $\beta$ , obtained by omnisoott using harmonic mean (red solid line) and Fuchs interpolation (green dashed line) with DEM results (symbols) [155] . . . . .	45
3.2	The schematic of agglomeration process in the coagulation test cases where initially spherical particle collide and form agglomerate . . . . .	45

3.3	The total number concentration of agglomerates and primary particles (a), and mobility and gyration diameter (b) obtained with omnisoot using MPBM and SPBM that are in close agreement with the DEM results [156] indicating the validation of coagulation sub-model . . . . .	46
3.4	The standard deviation (residual) of mobility diameter, $\sigma_g$ obtained with SPBM in close agreement with DEM results [156] (left pane) that reaches $\sigma_{g,fm} = 2.03$ characteristic of the free molecular regime [157]; the particle size distribution (normalized number concentration of agglomerates is plotted against non-dimensional volume in the right pane) at different residence times that overlaps after initial transient phase marking the attainment of self-preserving size distribution in good agreement with DEM results [155] . . . . .	47
3.5	The relative error (residual) of total carbon (red line) and hydrogen (green line) mass, and total internal energy residual of gas and soot (blue line) plotted against residence time during pyrolysis of 30% CH <sub>4</sub> -N <sub>2</sub> at 2455 K and 3.47 atm in the constant volume reactor simulated using different PAH growth models along with MPBM (solid line) and SPBM (dashed line) . . . . .	48
3.6	The relative error (residual) of total carbon (red line) and hydrogen (green line) mass, and total internal energy residual of gas and soot (blue line) plotted against reactor length (cm) in the adiabatic flow reactor during pyrolysis of 30% CH <sub>4</sub> -N <sub>2</sub> at 2100 K and 1 atm simulated using different PAH growth models and MPBM (solid line) and SPBM (dashed line) . . . . .	49
3.7	Different stages of shock wave propagation during shock-tube test from (a) before rupture of diaphragm leading to (b) propagation of incident shock towards the end of shock-tube and (c) its reflection from the end wall that increases pressure and temperature of test gas (Reprinted from Ref. [160]) . . . . .	50
3.8	Layout of the laser diagnostics and shock-tube setup. Spatial and spectral filtering is employed to ensure high-quality absorbance measurements to infer species mole fractions and soot volume fraction. Soot samples are collected at the shock-tube endwall. All lasers are aligned in a plane 1 cm from the endwall . . . . .	51
3.9	The time history of carbon mass fraction of CH <sub>4</sub> of 30% CH <sub>4</sub> pyrolysis at T=1861, 2083, and 2375 K using Caltech, KAUST, and ABF mechanisms compared with laser diagnostics data . . . . .	52
3.10	The time history of carbon mass fraction of C <sub>2</sub> H <sub>4</sub> of 30% CH <sub>4</sub> pyrolysis at T=1861, 2083, and 2375 K using Caltech, KAUST, and ABF mechanisms compared with laser diagnostics data . . . . .	53
3.11	The time history of carbon mass fraction of C <sub>2</sub> H <sub>2</sub> of 30% CH <sub>4</sub> pyrolysis at T=1861, 2083, and 2375 K using Caltech, KAUST, and ABF mechanisms compared with laser diagnostics data . . . . .	53
3.12	The time history of carbon mass fraction of CH <sub>4</sub> , C <sub>2</sub> H <sub>4</sub> , C <sub>2</sub> H <sub>2</sub> of 30% CH <sub>4</sub> pyrolysis at T=1861, 2083, and 2375 K using Caltech, KAUST, and ABF . . . . .	53
3.13	The time history of carbon mass fraction of soot precursors, A2, A3, A4 and A2R5 of 30% CH <sub>4</sub> pyrolysis at T=1861, 2083, and 2375 K using Caltech, KAUST, and ABF mechanisms . . . . .	54
3.14	The time history of soot volume fraction of 30% CH <sub>4</sub> pyrolysis at T=2375 K and P=3.75 atm using Caltech, KAUST, and ABF mechanism and different PAH growth and particle dynamics models . . . . .	54
3.15	The time history soot volume fraction, $f_v$ of 30% CH <sub>4</sub> pyrolysis for T=2155, 2313, and 2455 K using KAUST with different combinations of PAH growth and particle dynamics models compared with extinction measurements . . . . .	55
3.16	The soot volume fraction, $f_v$ at 1.5 ms increasing with temperature during 30% CH <sub>4</sub> pyrolysis using KAUST and SPBM. The dashed lines are added to guide the eye . . . . .	55
3.17	The time history of primary particle diameter, $d_p$ of 30% CH <sub>4</sub> pyrolysis for T=2155, 2313, and 2455 K using KAUST with different combinations of PAH growth and particle dynamics models . . . . .	55

3.18 The primary particle diameter, $d_p$ at 1.5 ms increasing with temperature during 30% CH <sub>4</sub> pyrolysis using KAUST with MPBM and SPBM. The dashed lines are added to guide the eye . . . . .	56
3.19 The time history of inception flux, $I_{inc}$ of 30% CH <sub>4</sub> pyrolysis for T=2155, 2313, and 2455 K using KAUST with different combinations of PAH growth and particle dynamics models . . . . .	56
3.20 The time history of mobility diameter, $d_m$ of 30% CH <sub>4</sub> pyrolysis for T=2155, 2313, and 2455 K using KAUST with different combinations of PAH growth and particle dynamics models . . . . .	56
3.21 The time history of rate of carbon mass addition by (a) HACA and (b) PAH adsorption at T=2313 K using KAUST with different combinations of PAH growth and particle dynamics models . . . . .	57
3.22 The time history of mole fraction of CH <sub>4</sub> of 10% CH <sub>4</sub> pyrolysis at T=1897, 2217, and 2406 K using Caltech, KAUST, and ABF mechanisms compared with laser diagnostics data . . . . .	58
3.23 The time history of mole fraction of C <sub>2</sub> H <sub>4</sub> of 10% CH <sub>4</sub> pyrolysis at T=1897, 2217, and 2406 K using Caltech, KAUST, and ABF mechanisms compared with laser diagnostics data . . . . .	58
3.24 The time history of mole fraction of C <sub>2</sub> H <sub>2</sub> of 10% CH <sub>4</sub> pyrolysis at T=1897, 2217, and 2406 K using Caltech, KAUST, and ABF mechanisms compared with laser diagnostics data . . . . .	59
3.25 The time history of carbon mass fraction of CH <sub>4</sub> C <sub>2</sub> H <sub>4</sub> , C <sub>2</sub> H <sub>2</sub> of 10% CH <sub>4</sub> pyrolysis at T=1897, 2217, and 2406 K using Caltech, KAUST, and ABF mechanisms compared with laser diagnostics data . . . . .	59
3.26 The time history of carbon mass fraction of A2, A3, A4, A2R5 of 10% CH <sub>4</sub> pyrolysis at T=1897, 2217, and 2406 K using Caltech, KAUST, and ABF mechanisms compared with laser diagnostics data . . . . .	59
3.27 A TEM image provided by Stanford group (left pane) with the generated binary map (middle pane) and detected agglomerates using the segmentation algorithm (right pane) . . . . .	60
3.28 Agglomerates in single TEM image segmented by K-means clustering (left pane) and otsu thresholding (right pane) . . . . .	60
3.29 The $d_m$ as a function of $d_p$ from TEM image obtained by atems [167] (symbols) compared with the power law in Eq. (3.2) . . . . .	61
3.30 The soot volume fraction, $f_v$ and number of primary particles, $N_{pri}$ (left pane), and , the soot inception flux, $I_{inc}$ and the primary particle diameter, $d_p$ predicted by KAUST mechanism, SPBM, and different PAH growth models at T=2230 K, P=4.5 atm that corresponds to shock-tube conditions of TEM measurement . . . . .	62
3.31 The variation of surface reactivity, $\alpha$ , as a function of temperature for different values of $\zeta$ and primary particle size of 2 nm (dashed lines) and 6 nm (solid lines) . . . . .	63
3.32 The effect of reducing $\zeta$ leading to larger HACA rates on soot volume fraction, $f_v$ using KAUST, SPBM and different PAH growth model . . . . .	63
3.33 The effect of reducing $\zeta$ leading to larger HACA rates on primary particle diameter, $d_p$ using KAUST and MPBM and different PAH growth model . . . . .	63
3.34 The effect of coalescence onsoot volume fraction, $f_v$ using KAUST, SPBM and different PAH growth model . . . . .	64
3.35 The effect of coalescence on primary particle diameter, $d_p$ using KAUST and SPBM and different PAH growth model . . . . .	64
3.36 The effect of inception flux and PAH adsorption rate on soot volume fraction, $f_v$ , using KAUST, Reactive Dimerization and SPBM . . . . .	65
3.37 The effect of inception flux and PAH adsorption rate on primary particle diameter, $d_p$ using KAUST, Reactive Dimerization and SPBM . . . . .	65

3.38 The soot volume fraction, $f_v$ and number of primary particles, $N_{pri}$ (left pane), the soot inception flux, $I_{inc}$ and the primary particle diameter, $d_p$ predicted by KAUST mechanism, SPBM, and different PAH growth models with optimized rate at T=2230 K, P=4.5 atm that corresponds to shock-tube conditions of TEM measurement . . . . .	66
3.39 The soot volume fraction, $f_v$ over 2000 K<T<2400 K, using KAUST, SPBM, and optimized inception models . . . . .	66
3.40 The primary particle diameter, $d_p$ over 2000 K<T<2400 K, using KAUST, SPBM, and optimized inception models . . . . .	67
3.41 The primary particle diameter, $d_p$ at t=2 ms over the studied temperature range using KAUST, SPBM, and optimized inception models. The dashed line is added to guide the eye. . . . .	67
B.1 The time history of temperature of 30% CH <sub>4</sub> pyrolysis at T=2184 K and P=3.62 atm using Caltech, KAUST, and ABF mechanisms and different PAH growth and particle dynamics models compared with the simulation results reported by Hanson Research Group . . . . .	89
B.2 The time history of CH <sub>4</sub> mole fraction of 30% CH <sub>4</sub> pyrolysis for 1861 K< T <2155 K using Caltech, KAUST, and ABF mechanisms without soot (only chemistry) and with soot modeling described by different PAH growth and particle dynamics models compared with laser diagnostic data . . . . .	90
B.3 The time history of CH <sub>4</sub> mole fraction of 30% CH <sub>4</sub> pyrolysis for 2184 K< T <2455 K using Caltech, KAUST, and ABF mechanism without soot (only chemistry) and with soot modeling described by different PAH growth and particle dynamics models compared with laser diagnostic data . . . . .	91
B.4 The time history of C <sub>2</sub> H <sub>4</sub> mole fraction of 30% CH <sub>4</sub> pyrolysis for 1861 K< T <2155 K using Caltech, KAUST, and ABF mechanisms without soot (only chemistry) and with soot modeling described by different PAH growth and particle dynamics models compared with laser diagnostic data . . . . .	92
B.5 The time history of C <sub>2</sub> H <sub>4</sub> mole fraction of 30% CH <sub>4</sub> pyrolysis for 2184 K< T <2455 K using Caltech, KAUST, and ABF mechanism without soot (only chemistry) and with soot modeling described by different PAH growth and particle dynamics models compared with laser diagnostic data . . . . .	93
B.6 The time history of C <sub>2</sub> H <sub>2</sub> mole fraction of 30% CH <sub>4</sub> pyrolysis for 1861 K< T <2155 K using Caltech, KAUST, and ABF mechanisms without soot (only chemistry) and with soot modeling described by different PAH growth and particle dynamics models compared with laser diagnostic data . . . . .	94
B.7 The time history of C <sub>2</sub> H <sub>2</sub> mole fraction of 30% CH <sub>4</sub> pyrolysis for 2184 K< T <2455 K using Caltech, KAUST, and ABF mechanism without soot (only chemistry) and with soot modeling described by different PAH growth and particle dynamics models compared with laser diagnostic data . . . . .	95
B.8 The time history of CH <sub>4</sub> mole fraction of 30% CH <sub>4</sub> pyrolysis for 1861 K< T <2455 K using Caltech, KAUST, and ABF mechanisms without soot compared with laser diagnostic data . . . . .	96
B.9 The time history of C <sub>2</sub> H <sub>4</sub> mole fraction of 30% CH <sub>4</sub> pyrolysis for 1861 K< T <2455 K using Caltech, KAUST, and ABF mechanisms without soot compared with laser diagnostic data . . . . .	96
B.10 The time history of C <sub>2</sub> H <sub>2</sub> mole fraction of 30% CH <sub>4</sub> pyrolysis for 1861 K< T <2455 K using Caltech, KAUST, and ABF mechanisms without soot compared with laser diagnostic data . . . . .	97
B.11 The time history of carbon mass fraction of CH <sub>4</sub> , C <sub>2</sub> H <sub>4</sub> , C <sub>2</sub> H <sub>2</sub> of 30% CH <sub>4</sub> pyrolysis for 1861 K< T <2455 K using Caltech, KAUST, and ABF mechanisms without soot . . . . .	97
B.12 The time history of carbon mass fraction of soot precursors, A2, A3, A4, and A2R5 of 30% CH <sub>4</sub> pyrolysis for 1861 K< T <2455 K using Caltech, KAUST, and ABF mechanisms without soot . . . . .	98

B.13 The time history of soot volume fraction, $f_v$ of 30% CH <sub>4</sub> pyrolysis for 1861 K < T < 2455 K using KAUST with different combinations of PAH growth and particle dynamics models compared with extinction measurements . . . . .	98
B.14 The time history of primary particle diameter, $d_p$ of 30% CH <sub>4</sub> pyrolysis for 1861 K < T < 2455 K using KAUST with different combinations of PAH growth and particle dynamics models compared with extinction measurements . . . . .	99
B.15 The time history of inception flux, $I_{inc}$ of 30% CH <sub>4</sub> pyrolysis for 1861 K < T < 2455 K using KAUST with different combinations of PAH growth and particle dynamics models compared with extinction measurements . . . . .	99
B.16 The time history of mobility diameter, $d_m$ of 30% CH <sub>4</sub> pyrolysis for 1861 K < T < 2455 K using KAUST with different combinations of PAH growth and particle dynamics models compared with extinction measurements . . . . .	100
B.17 The time history of C <sub>2</sub> H <sub>2</sub> mole fraction of 30% CH <sub>4</sub> pyrolysis at T=2184 K and P=3.62 atm using Caltech, KAUST, and ABF mechanism and different PAH growth and particle dynamics models compared with laser diagnostic data . . . . .	100
B.18 The time history of CH <sub>4</sub> mole fraction of 10% CH <sub>4</sub> pyrolysis for 1861 K < T < 2455 K using Caltech, KAUST, and ABF mechanisms without soot compared with laser diagnostic data . . . . .	100
B.19 The time history of C <sub>2</sub> H <sub>4</sub> mole fraction of 10% CH <sub>4</sub> pyrolysis for 1861 K < T < 2455 K using Caltech, KAUST, and ABF mechanisms without soot compared with laser diagnostic data . . . . .	101
B.20 The time history of C <sub>2</sub> H <sub>2</sub> mole fraction of 10% CH <sub>4</sub> pyrolysis for 1861 K < T < 2455 K using Caltech, KAUST, and ABF mechanisms without soot compared with laser diagnostic data . . . . .	101
B.21 The time history of carbon mass fraction of CH <sub>4</sub> , C <sub>2</sub> H <sub>4</sub> , C <sub>2</sub> H <sub>2</sub> of 10% CH <sub>4</sub> pyrolysis for 1861 K < T < 2455 K using Caltech, KAUST, and ABF mechanisms without soot . . . . .	102
B.22 The time history of carbon mass fraction of soot precursors, A2, A3, A4, and A2R5 of 10% CH <sub>4</sub> pyrolysis for 1861 K < T < 2455 K using Caltech, KAUST, and ABF mechanisms without soot . . . . .	102
B.23 The soot volume fraction, $f_v$ over 1800 K < T < 2400 K and P near 1 and 4 atm for 10% CH <sub>4</sub> pyrolysis using KAUST, SPBM and optimized PAH growth models that minimizes $f_v$ and $d_p$ at T=2217 and P=4.43 atm . . . . .	103
B.24 The primary particle diameter, $d_p$ over 1800 K < T < 2400 K and P near 1 and 4 atm for 10% CH <sub>4</sub> pyrolysis using KAUST, SPBM and optimized PAH growth models that minimizes $f_v$ and $d_p$ at T=2217 and P=4.43 atm . . . . .	103
B.25 The temperature dependence of soot yield during pyrolysis of 5% CH <sub>4</sub> -Ar (left pane) and 10% CH <sub>4</sub> -Ar (right pane) at P = 4.5–6.7 bar obtained using Caltech mechanism and different inception models compared with measurements at 1.5ms [1] where the absorption funtion of E(m)=0.37 is used to estimate soot yield. . . . .	104
B.26 The temperature dependence of carbon mass fraction of soot precursors (A2, A2R5, A3, and A4) combined during pyrolysis of 5% CH <sub>4</sub> -Ar (left pane) and 10% CH <sub>4</sub> -Ar (right pane) at P = 4.5–6.7 bar obtained using Caltech mechanism and different inception models at t=1.5 ms . . . . .	105
B.27 The temperature dependence of carbon mass fraction of C <sub>2</sub> H <sub>2</sub> during pyrolysis of 5% CH <sub>4</sub> -Ar (left pane) and 10% CH <sub>4</sub> -Ar (right pane) at P = 4.5–6.7 bar obtained using Caltech mechanism and different inception models at t=1.5 ms . . . . .	105
B.28 The temperature dependence of average number of primary particle per agglomerate, $n_p$ during pyrolysis of 5% CH <sub>4</sub> -Ar (left pane) and 10% CH <sub>4</sub> -Ar (right pane) at P = 4.5–6.7 bar obtained using Caltech mechanism and different inception models at t=1.5 ms . . . . .	106
B.29 The time variation of standard geometric deviation of mobility diameter, $\sigma_g$ during pyrolysis of 5% CH <sub>4</sub> -Ar (left pane) and 10% CH <sub>4</sub> -Ar (right pane) at P = 4.5–6.7 bar obtained using Caltech mechanism and different inception models at t=1.5 ms . . . . .	106

- 
- B.30 The temperature dependence of standard geometric deviation of mobility diameter,  $\sigma_g$  during pyrolysis of 10% CH<sub>4</sub>-Ar at T=2500 K (left pane) and T=2700 K (right pane) . . . . . 107

# Nomenclature

## Acronyms

CFD	Computational Fluid Dynamics
DEM	Discrete Element Modelling
HACA	Hydrogen abstraction carbon addition
MPBM	Monodisperse Population Balance Model
SPBM	Sectional Population Balance Model

## Constants

$Av$	Avogadro's number .....	$6.02214076 \times 10^{23}$	1/mol
$k_B$	Boltzmann constant .....	$1.3806488 \times 10^{-23}$	$\text{m}^2\text{kg/s}^2\text{--K}$

## English symbols

$C_{tot}$	Totla carbon content of soot particles (per section) .....	mol/kg
$D$	Diffusion coefficient of particles .....	$\text{m}^2/\text{s}$
$d$	diameter .....	m
$d_c$	Collision diameter .....	m
$d_g$	Gyration diameter .....	m
$D_H$	Duct hydraulic diameter .....	—
$d_m$	Mobility diameter .....	m
$d_p$	Primary particle diameter .....	m
$f$	Friction factor .....	—
$H_{tot}$	Totla hydrogen content of soot particles (per section) .....	mol/kg
$I$	Source terms for soot variables .....	$\text{mol}/(\text{kg} \cdot \text{s})$
$k$	reaction rate constant .....	$\text{m}^3/(\text{mol} \cdot \text{s})$
$Kn$	Knudsen number .....	—
$m$	mass .....	kg
$n_p$	Number of primary particles of per agglomerate .....	—
$N_{agg}$	Number density of agglomerates .....	mol/kg
$N_{pri}$	Number density of primary particles .....	mol/kg
$R_H$	Duct hydraulic radius .....	—
$SF$	Sectional spacing factor .....	—
$T$	Temperature .....	K
$W$	Molecular weight .....	kg

## Greek symbols

$\beta$	Collision frequency .....	$\text{m}^3/\text{s}$
$\delta_a$	Mean distance of particles .....	m
$\lambda$	Mean free path .....	m
$\lambda_a$	Mean stopping distance of particles .....	m
$\nu$	Gas kinematic viscosity .....	$\text{m}^2/\text{s}$
$\rho$	Gas density .....	$\text{kg}/\text{m}^3$

---

$\rho_{soot}$	Soot density .....	kg/m <sup>3</sup>
$\varphi$	Soot volume fraction .....	m <sup>3</sup> /m <sup>3</sup>

**Subscripts**

ads	Adsorption
agg	Agglomerate
coag	Coagulation
cont	Continuum
f	forward
fm	Free molecular
g	Gyration
grow	Surface growth
inc	Inception
m	Mobility
ox	Oxidation
pri	Primary particle
r	reverse
reac	reactive

# Chapter 1

## Introduction

### 1.1 Motivation

Carbonaceous nanoparticles, such as Carbon Black (CB) and soot, are widely encountered in nature and engineering. Every year, nearly 9.5 megatons of soot (black carbon) is emitted into the atmosphere from anthropogenic activities and natural sources such as wildfires and volcanoes [2]. The wide light absorption range of soot reduces the albedo of snow-covered area and alters the radiative forcing balance in the atmosphere making soot the third strongest contributor to climate change after methane and carbon dioxide [2]. Also, exposure to combustion-generated soot could promote respiratory and cardiovascular diseases [3]. So, strict regulations are targeting combustion engines to limit environmental and health risks from soot formation [4]. Accurate and affordable models are essential for the prediction of soot composition and morphology in combustion devices and the reduction of emissions in engines. They can also provide better understanding of soot optical properties that are major indicator of soot environmental effects.

On the other hand, CB with a similar synthesis process and structure to soot but higher elemental carbon to hydrogen ratios (>97%) [5] is commercially produced and sold in large scales. In fact, CB is the largest industrially produced nanomaterial by value and volume (~15 megatons per year with a value of \$17B) with applications as a reinforcing agent in rubber and tire industries [6], and conductive additive in lithium-ion batteries [7]. CB is primarily manufactured by the so-called furnace process in which about 50% of heavy fuel oil is partially combusted to convert the rest of it into CB [8]. This process suffers from low mass yield and excessive emission, generating 4 tons of CO<sub>2</sub> per each ton of product on average [9]. Plasma reactor is an emerging alternative production method with distinct advantages over flame-based methods: They can achieve 100% carbon yields with no direct CO<sub>2</sub> emission or other pollutants [10], and the energy required for pyrolysis is supplied by an electric arc that does not depend on the feedstock composition. Controlling CB properties such as its specific surface area (or primary particle diameter), hard agglomerate size (or gyration diameter of agglomerates with primary particles connected to each other by strong chemical bonds), and composition (or particle carbon to hydrogen ratio) is important to make the process economical and to achieve specific grades of CB for different target applications. However, this is a challenging task because of the complexity of CB formation and mass growth processes and its coupling with gas phase chemistry, dependence on local temperature and pressure. This requires accurate process design and optimization tools built on physics of CB formation and evolution to inform manufacturers' decisions for production of CB with desired grades [11].

The term "soot" usually refers to the unwanted particulate matter formed during incomplete combustion of any carbon-containing material from jet and diesel fuel to wood, heavy oil, and plastics with variable organic content and a large variation in C/H ratio [5], but this research focuses on soot particles generated under controlled laboratory conditions from fuels with known compositions. The mature soot formed in methane and ethylene premixed flame can reach 95% elemental C/H ratio [12], which is close to CB composition. The comparison of transmission electron microscopy (TEM) images of industrially produced CB [13] with soot sampled from diesel fuel [14, 15] shown in

Fig.1.1 indicates similarity of their morphology and structure. Hereafter, soot will be used to collectively refer to carbonaceous nanoparticles produced in flame/reactor during combustion/pyrolysis processes.

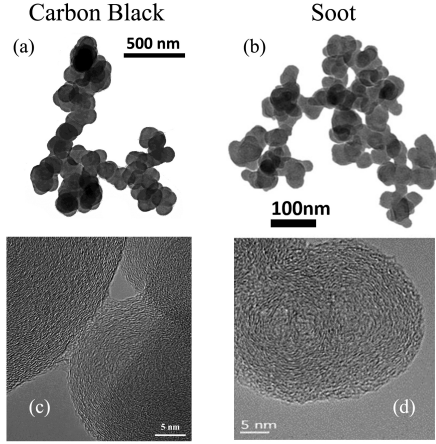


Figure 1.1: The TEM images of Carbon black (a & c) [13] and soot (b & d) [14, 15] that shows soot and CB has similar morphology and structure

## 1.2 Background

### 1.2.1 Soot inception and surface growth

Soot formation involves concurrent processes with different time and length scales starting from the breakdown of hydrocarbon molecules to formation of intermediate species and radicals that transition into soot particles and grow via heterogeneous reactions on the surface as well as coagulation [16]. The TEM analysis of soot sampled from flames [15], reactors [17], and engines [18] with different fuels and process conditions revealed a common fractal-like morphology, often characterized as agglomerates of primary particles. High resolution transmission electron microscopy (HRTEM) of soot primary particles showed clusters of precondensed Polycyclic Aromatic Hydrocarbons (PAHs) [19] pointing to PAHs as main soot precursors. This hypothesis was also supported by thermodynamic stability of PAHs enabling them to resist dissociation at high flame temperatures [20].

However, the transition of PAHs (soot precursors) to incipient soot, known as *soot inception* has not been well understood at the level of pathways and elementary reactions [21] primarily due to uncertainties in PAH (precursor) chemistry. The thermodynamics of PAH growth from acetylene ( $C_2H_2$ ) as the dominant hydrocarbon species in fuel pyrolysis and an intermediate of molecular growth does not experience a significant enthalpy release or entropy increase, so the path is driven by a gradual reduction in Gibbs free energy. As a result, the kinetics of PAH growth into subsequent soot particles can be highly reversible hence sensitive to local temperature, pressure and intermediate species concentration.

The growth of PAHs beyond first ring (benzene) is predominantly driven by so-called hydrogen abstraction carbon (acetylene) addition (HACA) mechanism [22] where a hydrogen radical abstracts an hydrogen atom at the edge of PAH, providing a reactive site for acetylene addition. The kinetic reversibility of HACA opens the door for competing pathways such as chain reactions of resonance-stabilized radical (RSR). Propargyl is a prominent example of these radicals, whose combination is known as a major contributor to benzene formation [23]. Built on this hypothesis, Johansson et al. [24] proposed a radical-driven growth mechanism by addition of vinyl ( $C_2H_3$ ) starting from cyclopentadienyl ( $C_5H_5$ ) to larger hydrocarbon radicals that can survive long enough in high temperatures to react with other radicals, PAHs and unsaturated aliphatic species, through radical chain reactions. However, low concentrations of these radicals limit the growth rate through RSR

pathways [25]. Moreover, some of the intermediate steps for radical regeneration such as formation of vinylcyclopentadienyl were shown to be kinetically unfavorable [25] compared to HACA. Regardless of their mechanistics, these sequential growth mechanisms, termed as *chemical growth* cannot account for rapid soot formation [22] and its nanostructure [26].

There is abundant but mostly indirect experimental and computational evidence pointing to an alternative collision-based mechanism for soot inception. HRTEM images of nascent and mature soot shows disordered PAH clusters highlighting the role of PAH collisions. The bimodality of particle size distribution (PSD) of nascent soot particles in premixed flames [27] indicates that the kinetics of inception is second order in precursor concentration [28]. The time-of-flight mass spectrometry (TOFMS) experiments in a 13 kPa acetylene-oxygen flame showed a series of peaks with a periodicity of 500 amu [29].

It is not clear how PAH clusters form and what forces allow the binding occur and resist dissociation at flames temperatures ( $T \geq 1600$  K). Frenklach [22] described clustering of PAHs as an irreversible process where two PAHs collide and stick upon collision forming dimers held together by Van der Waals (vdW). Herdman and Miller [30] found that the binding energy of PAHs dimers due to dispersive and electrostatic forces increases linearly with molecular mass and reaches the limit of exfoliation energy for graphite. However, the entropy barrier of dimerization increases with PAH size making them unfavorable under equilibrium conditions. So, PAHs as large as circumcoronene ( $C_{54}H_{18}$ ) can only form dimer to survive flame temperatures [21]. However, the concentration of large PAHs are too low to account for the observed number density of soot particles in flames [31].

There is also the possibility of PAH clustering governed by non-equilibrium kinetics. PAH molecules can form rovibrationally excited dimer with long enough life-time [32] to react with H atoms forming covalent bonds. There is another possibility for these clusters to be joined by aliphatic linkages. Micro-FT-IR spectroscopy analysis by Cain et al. [33] showed the ratio of aliphatic-to-aromatic C–H bonds can exceed unity at the flame temperature. Using these findings, they suggested that the aliphatic components in the form of alkyl and alkenyl can covalently bound to aromatic units in soot particles. Although such a mechanism is viable near the flame region, it cannot explain persistent soot inception in the post-flame zone [34] where the H atom concentration is too low to initiate H abstraction reactions that produce those radicals.

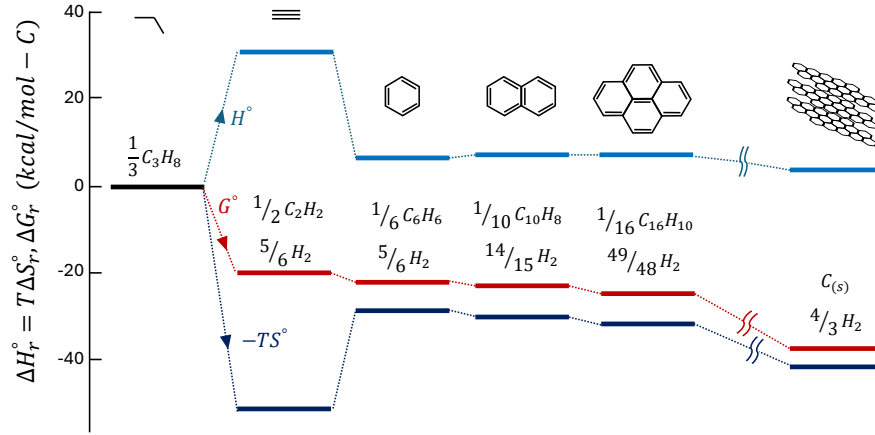


Figure 1.2: Standard enthalpy ( $\Delta H$ ) and entropy ( $T\Delta S$ ) contributions to Gibbs function of reaction  $\Delta G$  at 1600 K for carbon formation from propane(reprinted from Ref. [21])

There are other complicating factors that hinders the fundamental understanding of soot inception such as lack of a decisive criterion to distinguish gaseous molecules from particles [16], and the overlap of inception with surface growth and agglomeration [35]. Measurement techniques have limited capability in soot detection due to short time and length scales of soot inception and surface growth ranging from pico- to milliseconds and micro- to millimeter [36]. Fig. 1.3 demonstrates the length and time scales relevant to different stages of soot formation from PAH precursors to incipi-

ent, nascent and mature soot in flames. Moreover, the collected data from measurements might not be true representatives of soot formed at the probed location of the studied process. For example, intrusive diagnostic methods based on thermophoresis or dilution have a sampling probe that can perturb flow dynamics or alter structure and composition of soot [37]. Non-intrusive techniques such as optical methods also rely on assumptions about light absorption and scattering of soot [38] and its morphology [39].

Despite the gaps in fundamental understanding of soot formation and limitations of diagnostics methods, models have been developed describe the soot inception and growth. These models have been formulated as a set of clear pathways that explain soot inception based on collisions of PAH molecules. They have to be consistent with current knowledge of soot inception, feasible to be coupled with chemistry and particle dynamics models, and able to predict soot mass, PSD and morphology observed in flames and reactors.

The classic description of soot inception relies on PAH dimerization where collision of two PAH molecules (monomers in this context) forms a dimer held together by Van der Waals forces [40]. The dimerization is a irreversible process with an efficiency that accounts for the reversibility or dissociation of dimers. The theory postulates that PAH growth continues by sequential addition of a monomer (PAH molecule) forming stacks of dimers, trimers, tetramers and so on to reach a certain mass threshold that marks the emergence of incipient soot [40], but for practical purposes, a dimer is usually considered as an incipient soot. Here, we call this model *Irreversible Dimerization*. Irreversible Dimerization has been used to predict soot formation in burner-stabilized premixed [41, 42], counterflow diffusion flames [43, 44], coflow diffusion flames [45, 46]. A collision efficiency factor ranging between  $10^{-6}$  to 1 is also employed to adjust the inception flux and PAH adsorption rates to achieve desired soot mass and size distribution. PAHs of moderate sizes such as pyrene (4 rings) to coronene (7 rings) have been considered as the starting point of inception due to their thermodynamic instability that justifies the irreversibility at high temperatures [40]. However, the theoretical calculations [47] and experiments [48] indicated that PAH dimerization is highly reversible in flame conditions.

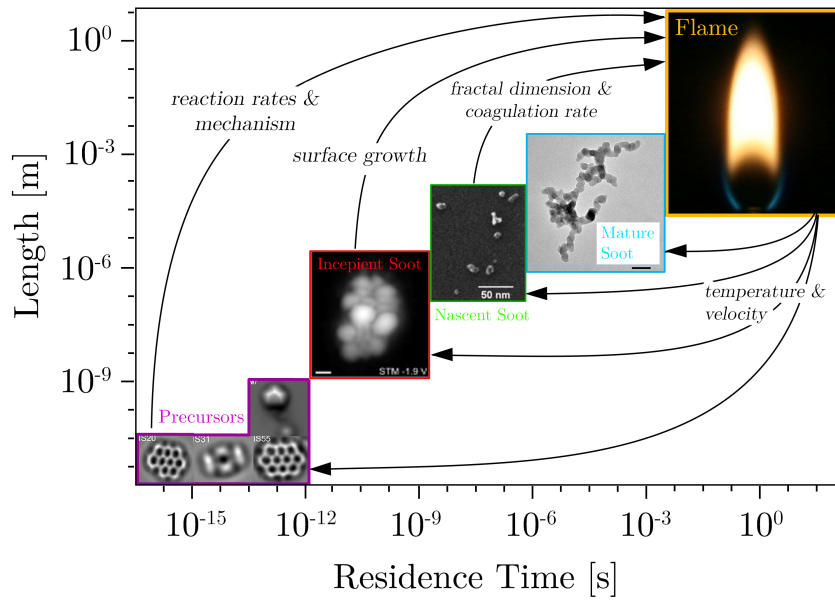


Figure 1.3: The range of time and length scales of the processes involved in soot formation from molecular reactions to particle-fluid interaction in flames

The inception flux of irreversible dimerization is determined from collision of PAHs, which is proportional to  $\sqrt{T}$ , so new particles can be formed at low temperatures (even less than 500 K) [49] despite experimental evidence for termination of inception below 1200 K [50, 51]. Moreover, the

arbitrary selection of efficiency factors alters the distribution of mass between inception of surface growth could significantly change soot mass, PSD, and morphology [52]. Miller [53] used equilibrium constant for PAH dimerization to calculate the net dimerization rate and demonstrated that the collision of PAHs larger than circumovalene ( $\sim 800$  amu) could last long enough grow into incipient soot. However, the concentration of PAHs drops rapidly with size [21]. The entropy barrier of dimerization is significant for larger PAHs [54].

Eaves et al. [55] relaxed the irreversibility assumption, and developed a reversible clustering model to simulate inception using an array of PAHs from naphthalene to benzo-pyrene. Building on that work, Kholghy et al. [56] emphasized on the necessity of chemical bond formation after physical PAH clustering for accurate prediction of volume fraction, primary particle diameter and PSD in ethylene coflow diffusion flames. Later, Kholghy et al. [57] proposed the "*Reactive Dimerization*" model which starts with reversible collision of PAHs leading to physical dimers held with vdW forces that are graphitized and form chemically-bonded dimers that serve as soot nuclei grow via surface reactions. They also performed a systematic analysis on the contribution of different PAHs, and concluded that one- and two-ring aromatics account for almost all of inception flux in the so-called "*sooting flame*" [42]. However, Frenklach and Mebel [25] pointed out that an inception model that initiated with a highly reversible step similar to Reactive Dimerization [57] cannot produce sufficient flux of particles to match measurements of the benchmark burner-stabilized stagnation flame [28]. Instead, they proposed a HACA-driven mechanism where addition of monomer molecule to its radical activated by hydrogen abstraction for a stable dimer via an E-Bridge bond formation, and this sequential process continues to form trimers, tetramers, and larger PAH clusters.

The gas-phase chemistry of aromatics can be extended to account for chemical growth of incipient soot via surface reactions [22]. This hypothesis, known as "chemical similarity" postulates that the reactions occurring on the soot surface are similar to those involving large molecules of PAHs in the gas phase. It also provides means to describe the rates of surface growth and particle oxidation in terms of elementary chemical reactions. In other words, it is assumed that the surface of soot particles is made up of lateral faces of large PAHs covered with C-H bonds. This is the basis for HACA mechanism [40, 58] that assumes the soot surface to consist of hydrogenated sites with a predefined density. Mass growth on soot surface requires H-abstraction to form a radical site, followed by acetylene attack similar to growth of PAH molecules in the gas-phase. The reactivity of these sites changes with time and temperature [59, 60], described as soot aging. For modelling purposes, a temperature-dependent multiplier, usually represented by  $\alpha$ , was introduced to account for these effects. Appel et al. [58] showed  $\alpha$  changes with temperature and particle size.

Adsorption of PAHs on the surface of soot particles is also a viable growth mechanism [40], more specifically called physisorption or chemisorption depending on the mechanisms driving the adsorption process [61]. There is still debate over the stability of adsorbed PAH molecules on soot surface [62]. Following the hypothesis that PAHs are building blocks of soot particles, a mechanism similar to inception is often used to describe PAH-soot growth.

## 1.3 Coagulation and agglomeration

In typical soot formation processes such as those occurring in flames and reactor, soot particles are formed at high number concentrations ( $10^{12}$  1/cm<sup>3</sup>), and inception and surface growth are relatively short compared to the total residence time of soot particles. As a result, coagulation becomes dominant rapidly attaining both [63] self-preserving size distribution (SPSD) [64] and asymptotic fractal-like structure [65]. The evolving fractal-like structure of agglomerates quantified by their mobility diameter normalized by primary particle,  $d_m/d_p$ , and gyration,  $d_m/d_g$ , diameters can be described with power laws derived from mesoscale simulations [66]. The collision frequency of agglomerates depends on their evolving fractal-like morphology. Also, polydisperse agglomerates collide more frequently than monodisperse ones. The enhancement in their collision frequency reaches an asymptotic value of 35% [63] or 82% [67] in the free molecular or transition regimes, respectively at SPSD regardless of the polydispersity in their constituent primary particles. Particle morphology formed by inception, surface growth and agglomeration can be tracked precisely by

mesoscale simulations, such as Discrete Element Modeling (DEM) [68] where each agglomerate is tracked separately. However, they are computationally expensive and interfacing them with chemical kinetics in computational fluid dynamics (CFD) is not trivial [69]. This limits their application in simulation of realistic flames and reactors. So, sectional population balance models (SPBM) are often used to track agglomerate and primary particle size distribution [70], morphology [71], and composition [45] in complex laminar [45] and turbulent flows [72]. Using the SPBMs coupled with relations for agglomerate fractal-like structure [73] and collision frequency [36], particle size distribution, morphology and composition can be tracked accurately. However, the computational cost of SPBMs increases exponentially with the number of sections [70] and particle properties [45] tracked. Thus, one property (e.g. agglomerate mass) is typically tracked with SPBMs to reduce computational cost. This does not allow to account for agglomerate fractal-like structure [74, 75] which limits SPBM accuracy in predicting surface growth and coagulation rate of agglomerates and their size distribution.

Alternatively, particle dynamics can be tracked by the method of moments (MOM) [76] or monodisperse population balance models (MPBM) [77]. Such models only track average particle properties (e.g. moment ratios) and their accuracy could be limited if unrealistic assumptions (e.g. approximating agglomerates as monodisperse and perfect spheres) are used. However, when inception and surface growth are short [78] and high particle (number) concentrations are formed [66], they lead to rapid attainment of self-preserving size distributions (SPSD) and agglomerates having asymptotic structure [63]. In this case a MPBM or MOM can be assembled on a firm scientific basis with accuracy on par with DEM [68], SPBM [79] and experimental data [80, 81, 82]. Such models can be readily interfaced with CFD simulations [83] without significant computational cost, making them ideal for three-dimensional and even turbulent flame simulations.

The MOM tracks moments of the PSD and estimates average particle properties such as mass [84], surface area [85], the number of constituent primary particles per agglomerate,  $n_p$  [76], or even particle composition [86] using the ratio of the moments. The MOM with four equations was used to describe synthesis of optical fibers by simultaneous reaction, diffusion, coagulation and thermophoresis of  $\text{SiO}_2$  in laminar flow reactors assuming a lognormal PSD [87]. The MOM with interpolative closure (MOMIC) was developed to predict simultaneous nucleation, surface growth and coagulation of soot agglomerates and estimate its PSD with six equations [76]. To calculate source terms of the transported moments, additional moments that are not tracked are needed preventing the closure of the system of differential equations with the MOM [84, 88]. Thus, often the PSD shape is assumed a priori [84] or extra equations are solved to estimate it [77].

The MPBMs do not have the closure problem and calculate average particle properties by tracking their total concentration, mass [77] and area [89, 90]. Leung et al. [91] used a 2-equation MPBM to track soot concentration and mass in (non-premixed) flames assuming spherical particles. Good agreement was achieved for measured soot mass. However, the specific surface area [90] and coagulation frequency of spheres are significantly smaller compared to that of agglomerates with the same mass underestimating their oxidation rate [79] and overestimating their concentration [77]. Kruis et al. [77] proposed a 3-equation MPBM to account for the fractal-like structure of nanoparticle agglomerates during coagulation and sintering. Agglomerate volume and area were used to obtain their equivalent primary particle diameter,  $d_p$ , and  $n_p$ . Then, agglomerate collision diameter, i.e.  $d_g$ , was calculated by  $D_f$ ,  $d_p$  and  $n_p$  to account for their fractal-like structure that affects their collision frequency. Tsantilis and Pratsinis [89] extended the MPBM to predict hard-(chemically-bonded) and soft- (physically-bonded) agglomerates during synthesis of  $\text{SiO}_2$  and  $\text{TiO}_2$  [92] nanoparticles with simultaneous reaction, surface growth, coagulation and sintering. Such a MPBM applies best at high concentrations when inception and surface growth are short [78] resulting in the dominance of coagulation where particles rapidly reach their SPSD and asymptotic fractal-like structure. This is often the case for soot emitted from a variety of combustion devices or CB reactors where inception and surface growth are limited to only a few milliseconds when temperature is very high (i.e.  $T \geq 1500\text{K}$ ) [57].

## 1.4 Soot maturity and its optical properties

The maturity level of soot is described as the evolution of physical and chemical properties from incipient to graphite-like mature soot [93]. It involves the growth of the graphitic crystallite fine structure of soot within, and perpendicular to, the aromatic layers [94, 95], known as graphitization, followed by increase in the size of the crystallite-layer planes and decrease of the interlayer spacing [19]. This process is accompanied by the pyrolytic conversion of hydrocarbon species and substituted hydrocarbons toward elemental carbon and increase in the carbon-to-hydrogen (C/H) ratio, known as carbonization. Soot maturity is closely associated with reactivity of surface sites [96]. Fig. 1.4 compares nanostructure of nascent soot composed of disoriented PAH clusters with that of mature soot with a core-shell pattern where disordered core is surrounded by concentrically oriented graphitic layers [29]. The core-shell nanostructure of mature soot strongly depends on process conditions such as pressure, fuel identity, temperature and residence time of the particles.

Evolution of soot maturity and morphology impacts its optical properties. Incipient and nascent soot absorb shorter wave lengths ( $\lambda < 600 \mu\text{m}$ ) as opposed to mature soot particles that are broad-band light absorbers [97]. Non-intrusive optical diagnostic methods such as light extinction (absorption and scattering) [98] and Laser Induced Incandescence (LII) [38] are widely utilized to measure soot volume fraction,  $f_v$  using extinction coefficient and the absorption function,  $E(m)$  that depends on soot refractive index,  $m$ , soot composition and morphology [99].

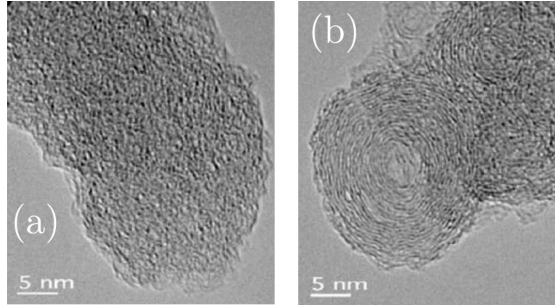


Figure 1.4: The HRTEM image of (a) a nascent soot primary particle with disordered internal nanostructure juxtaposed with that of (b) a mature soot primary particle with well-organized cluster near the shell sampled from soot generated by pyrolysis of ethanol at 1250 and 1650, respectively. Reprinted from Ref.[100]

However, the effects of soot composition, and morphology on its refractive index, and absorption function are not fully understood yet.  $E(m)$  of soot at  $\lambda = 1064 \text{ nm}$  measured by two-color LII measurements increases from 0.193 to 0.349, and 0.226 to 0.340 for ethylene premixed flames with equivalence ratio of  $\phi=2.1$  and  $\phi=2.3$ , respectively when height above burner (HAB) changes from 8 to 14 mm [101]. During acetylene pyrolysis in a shock tube,  $E(m)$  of soot particles increases from 0.05 to 0.25 as their primary particle diameter,  $d_p$ , grows to 20 nm within 1.6 ms [102]. Using  $m$  and  $E(m)$  of mature spherical soot [103] at different HABs neglecting the impact of soot morphology and composition on  $m$  [104] can overestimate soot volume fraction by 100% [105]. So, accurate estimation of the evolving optical properties of soot is essential to close the carbon mass balance in the measurements [105], and analyze reaction kinetics for soot inception [57] surface growth [58] and oxidation [106] that are essential for development and validation of aerosol dynamics models coupled with chemistry to predict soot formation.

The dependence of soot  $m$  on its morphology and composition can be quantified by soot optical band gap,  $E_g$  [107]. The optical band gap concept was originally proposed by Tauc et al. [108] for semi-conductors and later developed for amorphous carbon [109], and it can be used to describe the crystalline character of PAH clusters in soot [109]. Incipient flame-made soot with diameters less than 20 nm exhibit quantum dot behavior [110] with  $0.7 < E_g < 2 \text{ eV}$  that is larger than  $E_g$  of graphitized soot, 0.12 eV [110]. Optical band gap of organic carbon coated on soot remains nearly constant (1.8-1.9 eV) over soot evolution [111]. In contrast, Russo et al. [112] measured soot optical

band gap using ex-situ and in-situ methods and showed that  $E_g$  drops from 0.7 eV at HAB= 8 mm to 0.2 eV at HAB=14 mm in an ethylene premixed flame with  $\phi=2.3$  as particles grow and become more mature by carbonization. Kelesidis and Pratsinis [113] correlated the evolving refractive index of soot with its  $E_g$  obtained from quantum confinement theory (QCT) [110] for wavelengths of  $\lambda= 532$  and 1064 nm [113] by linear interpolations between that of nascent and mature soot. The proposed relations were then used with soot morphologies obtained from Discrete Element Modeling (DEM) simulations to obtain the evolving Mass Absorption Cross-section (MAC),  $E(m)$ , and the absorption function ratio of soot ( $E(\lambda=532\text{nm})/ E(\lambda=1024\text{nm})$ ) and compared with measurements [114, 115, 116]. Employing the relation in laser diagnostics to reprocess light extinction measurement data resulted in accurate prediction of  $f_v$  in moderate ( $\phi=2.34$ ) [105] and rich ( $\phi > 3$ ) ethylene premixed flames [117], and  $f_v$  along the centerline of a coflow ethylene diffusion flame [118] which is necessary to close the carbon mass balance in soot generating processes.

## 1.5 Oxidation

Soot oxidation is described as the removal of soot mass by reaction of molecular oxygen ( $O_2$ ), oxygen radical (O), and hydroxyl radical (OH) from soot surface. Because of its heterogeneous reaction kinetics and mechanisms, oxidation is expected to be sensitive to surface structure and composition. So, oxidation mechanisms depend on soot maturity and temperature-time history. In near stoichiometric and fuel-rich conditions, the contribution of OH radical to soot oxidation is predominant [119] compared to that of O radicals [120]. Femimore and Jones [121] investigated soot oxidation rate for low oxygen partial pressures and temperatures from 1530 to 1890 K, highlighted the importance of OH as a major oxidation agent, and attributed the faster rates compared to those predicted by Lee et al. [122], to OH oxidation. One approach for describing OH oxidation is by introducing collision efficiency representing the fraction of collisions of OH with soot particles that resulted in the removal of a carbon atom [119]. Scanning Mobility Particle Sizer (SMPS) with a two-stage burner also showed a collision efficiency of 0.13 [123].

The empirical relation of Nagle and Strickland-Constable (NSC) [124] originally developed for oxidation of pyrolytic graphite have been widely used to describe soot oxidation by  $O_2$ . It describes  $O_2$  oxidation rates based on partial pressure of  $O_2$  and the fraction of reactive edge sites to less reactive basal planes using the graphite analogy for soot. The dominance of edge sites in typical combustion conditions accounts for the relatively small reactivity of soot and basal planes become reactive at high temperature ( $>2500$  K) [120].  $O_2$  oxidation kinetics was also described with a power-law kinetics [122], and shown to be first order in oxygen concentration [125]. Alternatively, soot oxidation can be explained based on chemical similarity using HACA mechanism assuming that active site are attacked by  $O_2$  and OH leading to loss of carbon and release of CO.

A different oxidation regime has been identified for soot at low temperatures ( $T<1000$  K) where  $O_2$  diffuses and reacts with bulk soot accounting for most of soot mass consumption [81]. Internal oxidation compacts the pore network of soot resulting in hollow CB [126], diesel [127] and biodiesel [128] soot particles and increases their SSA up to a factor of four [127]. Oxidation can cause fragmentation of soot particles affecting their morphology. The increase in number concentration and the change of soot morphology in lean premixed flames [129] and in the oxidation region of diffusion flames [130] was attributed to fragmentation. Such a change in agglomerate morphology has not been observed in fuel-rich conditions, so fragmentation was linked to  $O_2$  oxidation.

## 1.6 Research objectives

The purpose of this project is developing a process design tool to predict the yield, morphology, composition and size distribution of soot particles in industrial flames and reactors under different temperatures, pressures and residence times. Integrating gas chemistry, all existing inception and surface growth models and particle dynamics in a single package provides a fully coupled soot description from breakdown of fuel to agglomeration and oxidation of particles that enables sensitivity analysis to shed light on key pathways for soot inception and surface growth in various targets. This

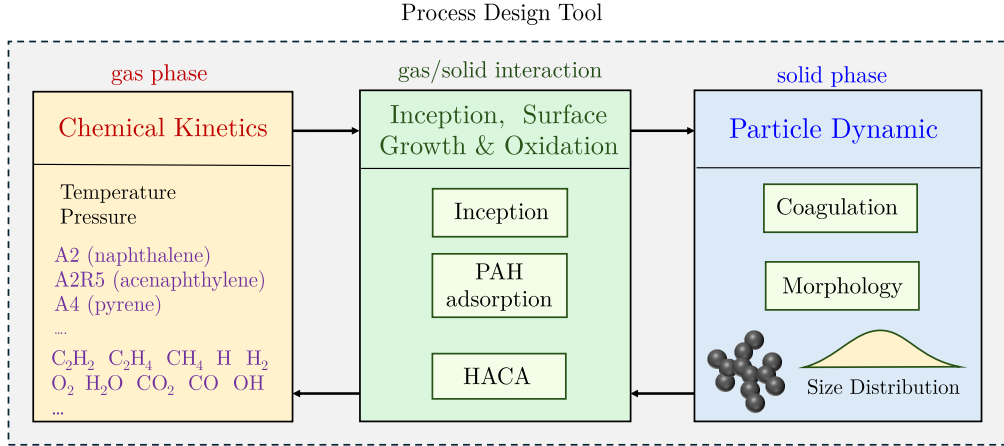


Figure 1.5: The conceptual structure of developed process design tool that account for gas mixture properties, and soot chemistry involving inception, surface growth and oxidation as well as its coagulation leading to the fractal-like morphology of soot particles

tool can also be used for rate constant optimization and mechanism reduction under soot forming conditions. The conceptual structure of this tool is shown in Fig 1.5 that includes a chemical kinetics unit coupled with Cantera [131] to compute thermal and physical properties of gas mixture such as temperature, pressure, density, and enthalpy based on ideal equation of state for the gas mixture. The chemistry of gas mixture is quantified using detail reaction mechanisms that enables tracking concentration of fuel, intermediate species such as  $C_2H_2$  and  $H_2$  essential to surface growth, and PAHs such as benzene (A1), naphthalene (A2) and pyrene (A4) known as building blocks of soot. The second unit accounts for soot inception and surface growth via PAH adsorption and HACA as well as surface oxidation. It accommodates the four inception models widely used in literature. The third unit deals with particle dynamics using a MPBM and SPBM to describe the coagulation of soot particles that results in the fractal-like structure of particle with an evolving size distribution. A multi-step validation procedure is followed to assess reliability of each sub-model that entails the comparison of collision frequency kernels and agglomerate morphology of different particle dynamics models with those of detailed DEM simulations and establishing energy and elemental carbon, and hydrogen balances for all combinations of particle dynamics and inception models with reactors and flames. This tool can be applied to a variety of experimental targets with different temperature- and pressure-time-histories, residence times, and fuel compositions.

The timeline for the future objectives of the project is shown in Fig. 1.6. As the first step, methane pyrolysis in shock-tube will be simulated using a constant volume reactor. The species measurements will be used to assess the reaction mechanism and examine carbon conversion flux from fuel to smaller intermediates and larger hydrocarbons. The inception flux and surface growth rates of the soot model strongly depend on the reaction mechanism employed to track the concentration of soot precursors. The performance of inception models will be analyzed by comparing the predicted soot volume fraction,  $f_v$  and primary particle diameter,  $d_p$ , with data collected from extinction and TEM measurements. A sensitivity analysis will be conducted on model parameters to identify the determining factors that control both  $f_v$  and  $d_p$  in the framework of shock-tube simulations with short residence time ( $t \approx 2$  ms) and high temperatures ( $\geq 2000K$ ). Then, the optimization of inception models will be performed by adjusting the rate constants within their physical limit (maximum collision rate of molecules) to minimize the prediction error for yield and morphology. This shows the range of inception flux that ensures the accurate prediction of soot yield and morphology represented by  $f_v$  and  $d_p$ , respectively in good agreement with measurements. Then, the optimized rates will be applied to shock-tube in a wide temperature range, and the  $f_v$  predictions will be compared with data. The measurement on shock-tube pyrolysis of methane with different  $H_2$  concentrations will be used to investigate the effect of hydrogen on pyrolysis chemistry as well

as soot yield and morphology. A main focus will be finding the reaction mechanism that describes methane decomposition rate and acetylene and PAH concentrations in good agreement with the data from absorbance measurements. The inception flux and surface growth rate that results in accurate prediction of soot yield and morphology will be estimated and compared with cases without hydrogen. A similar investigation will be conducted for flow reactors using plug flow reactor model of omnisoott at lower temperatures and longer residence times and then the range of expected inception flux will be compared with those of shock-tubes.

In the next step, a reactor network model based on omnisoott will be developed to enable building a series of plug flow reactors (PFR) and perfectly stirred reactor (PSR) models with multiple gas sources to more accurately represent complex industrial reactors. A set of tests will be developed to ensure gas and solid mass and energy balance during the development process. The connections between elements will be developed in a way that recognizes upstream and downstream flows. Moreover, safeguards will be put in place for the network to avoid faulty designs that can result in cyclical flows and detached networks. The performance of the reactor network will be evaluated using benchmark data from literature [132].

The flame solver of omnisoott will be developed from its current experimental stage to a functional level. After validation of the coagulation and surface growth sub-models and ensuring the conservation of carbon and hydrogen mass, and energy balances, the flame solver will be applied to a variety of counterflow diffusion [133, 134] and burner-stabilized premixed flames[28] with stagnation plate [82] at atmospheric and elevated pressures. The reaction mechanism study will be performed to reduce the uncertainty in tracking gas chemistry by comparing the model predictions of species concentration with measurements. The performance of the soot model will be evaluated by comparing the predicted soot volume fraction, agglomerate number concentration, PSD, mobility and primary particle diameters with those obtained from light extinction measurement, scanning mobility particle sizer (SMPS), and TEM samples, and the comparisons will be used to estimate the range of inception flux and surface growth rates that can predict soot mass, morphology and size distribution with minimum error compared to data.

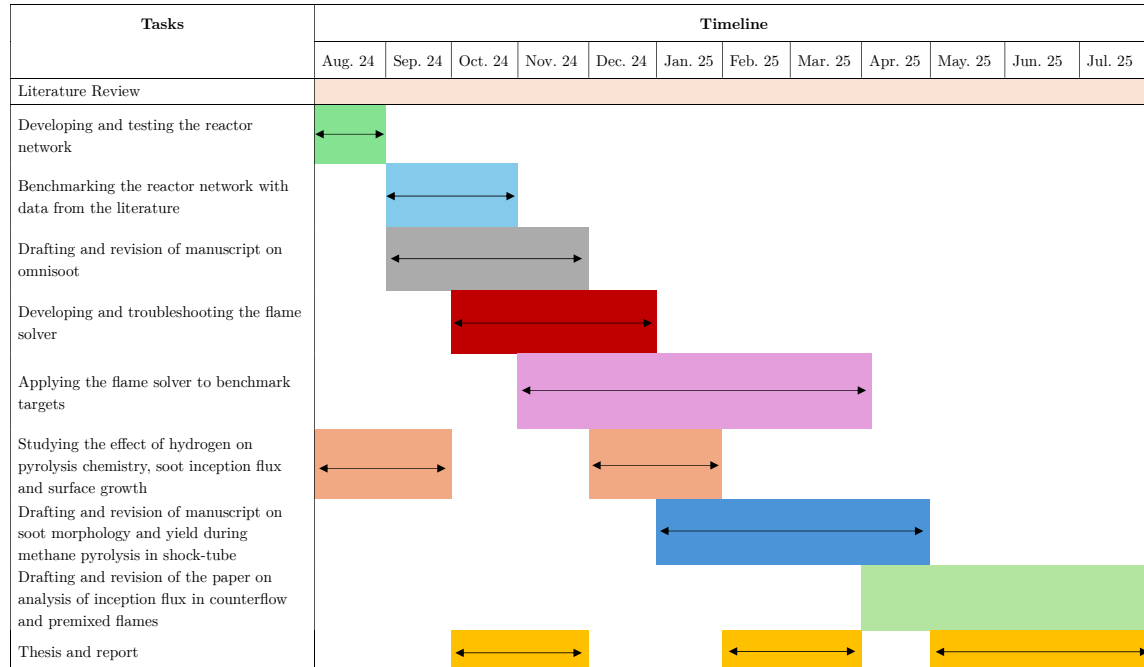


Figure 1.6: The timeline for the next steps of the project in 2024-2025

# Chapter 2

## Theoretical Model

In this chapter, the mathematical basis for *omnisoot* is explained in the top-to-bottom hierarchical order. The highest level is the reactors and flames that include the transport equations of gas mixture and "soot variables". Soot formation source terms are handled by the particle dynamics model that mainly addresses particle size distribution (PSD), morphology and coagulation rate. The "PAH growth model" computes the contribution of inception and adsorption to source terms based on PAHs designated as precursors. Similarly, the "surface reactions" model obtains the surface growth and oxidation rate by HACA mechanism and passes them to the particle dynamics model.

### 2.1 Assumptions and conventions

Here, the main conventions and assumptions used in the derivation of the mathematical model are listed below.

1. The ideal gas law is used to calculate physical, transport, and chemical properties of gas mixture.
2.  $\dot{s}_k$  denotes that rate production/consumption of  $k_{th}$  species due to soot formation. It is positive when the species is released to gas mixture.
3. Each soot agglomerate consists of spherical monodisperse primary particles in point contact.
4. The word "*particle*" refers to soot both in spherical and agglomerate shape.
5. The density of soot is assumed constant at the value of  $1800 \text{ kg/m}^3$ . This density represents an average between particles with small C/H ratio ( $\rho = 1600 \text{ kg/m}^3$ ) and large C/H ratios ( $\rho = 2000 \text{ kg/m}^3$ ) [135].
6. The incipient soot particles are 2 nm in diameter, so no particles could exist with a primary particle diameter smaller than 2 nm. The number of carbon atoms in the incipient soot particle is calculated from the mass of a sphere with the diameter of 2 nm assuming pure carbon content.

$$d_{p,min} = 2 \text{ nm}$$
$$n_{c,min} = \frac{\pi}{6} \rho_{soot} d_{p,min}^3 \frac{1}{MW_c} \approx 378. \quad (2.1)$$

7. The calculation of PAH adsorption and soot oxidation requires "*soot concentration*" which is defined as the number of soot agglomerates per unit volume of gas. The number density of agglomerates,  $N_{agg}$ , are tracked per unit mass of gas mixture i.e. #/kg<sub>gas</sub>. So, soot concentration can be calculated by multiplying agglomerate number density by gas density as:

$$[\text{soot}] = \rho \cdot N_{agg}. \quad (2.2)$$

8. The specific heat, internal energy and enthalpy of soot are approximated by those of pure graphite, and employed to close the energy balance in the system [136].
9. Soot particles and gas are in thermal equilibrium during studied processes.
10. There is no temperature gradient within each agglomerate.
11. *Soot variable* refers to the features/properties of soot particles tracked by the particle dynamics model and used in the soot transport equations.
12. *PAH growth* is a unit of the soot model with a set of pathways that determine the rate of inception and adsorption from PAHs in the gas mixture.
13. *Surface reactions* is a unit of the soot model that describes the addition of acetylene to soot surface, and removal of carbon via oxidation by OH and O<sub>2</sub> in the HACA scheme.
14. The superscript *i* denotes section number of a soot variable or property derived from variables. In the case of the monodisperse model, the section number can be ignored because it is equivalent to the sectional model with one section.
15. The computation of morphological parameters ( $d_p$ ,  $d_m$ ,  $d_g$ , and  $n_p$ ) and diffusion coefficient are done similarly by both particle dynamics models, so they are explained separately in standalone sections.

## 2.2 Flames

This research focuses on axisymmetric stagnation flames that reduces the laminar 3D steady-state equations in the cylindrical coordinates (r-z-θ system) to one-dimensional domain in r-z plane. The derivation of flow equations for a reacting gas is explained in detail in Section 7.2 of [137]. Here, the modified version of equations is provided that takes into account the mass and momentum of particles, the removal/release of species due to soot inception, surface growth and oxidation as well as the formation and sensible energy of soot.

Continuity:

$$\frac{\partial \rho u}{\partial z} = 2\rho V - \sum_j \dot{s}_j W_j, \quad (2.3)$$

Radial Momentum:

$$\rho u \frac{\partial V}{\partial z} + \rho V^2 = -\Lambda + \frac{\partial}{\partial z} \left( \mu \frac{\partial V}{\partial z} \right), \quad (2.4)$$

Energy:

$$[(1 - \varphi)\rho c_p + \varphi \rho_{soot} c_{p,soot}] u \frac{\partial T}{\partial z} = \frac{\partial}{\partial z} \left( K \frac{\partial T}{\partial z} \right) - \sum_k^{n_{sp}} J_k \frac{\partial h_k}{\partial z} - \sum_k^{n_{sp}} h_k W_k (\omega_k + \dot{s}_k), \quad (2.5)$$

Species:

$$\rho u \frac{\partial Y_k}{\partial z} = -\frac{\partial J_k}{\partial z} + W_j (\omega_k + \dot{s}_k), \quad (2.6)$$

where  $V = v/r$  is the scaled radial velocity, and  $\Lambda$  is the pressure eigenvalue.  $J_k$  denotes the diffusive flux of species  $k$  that is usually calculated using mixture averaged formulation.

$$J_K^* = -\rho \frac{W_k}{W_T} D'_{km} \frac{\partial X_k}{\partial z}, \quad (2.7)$$

$$J_K = J_K^* - Y_k \sum_{l=1}^{n_{sp}} J_l^*, \quad (2.8)$$

The details of calculation of mixture-averaged diffusive fluxes can be found in the documentation of `GasTransport::getMixDiffCoeffs()`<sup>1</sup> in Cantera [131]. Soot variables are treated similar to species, and their transport equations can be written as:

$$\rho u \frac{\partial \psi}{\partial z} = -\frac{\partial}{\partial z} \left( D \frac{\partial \psi}{\partial z} \right) + S_\psi, \quad (2.9)$$

where  $\psi$  is a generic soot variable that represents any of tracked soot variables.

## 2.3 Reactors

Zero-dimensional reactors are ideal representation of reactive systems typical in industrial applications. The strong mixing in the volume/cross-section allows description of thermal/chemical/hydrodynamic properties of mixture with a single variable that evolves in time. This section entails the conservation equations of mass, momentum (if applicable), species, energy, and soot for three reactor models.

### 2.3.1 Constant Volume Reactor

This reactor assumes that the volume of system does not change during the process. In the absence of soot, this leads to gas with constant density. However, soot formation converts part of gaseous species to solid particles thereby affecting its volume and density. Note that, continuity, species and energy transport equations only track gas mixture properties. Figure 2.1 illustrates the control volume over the gas mixture targeted by mass and energy balance equations. Any mass converted to solid soot particles leaves the control volume. Mass and energy passes through the control surface around solid particles by soot formation processes. Reactor volume is the sum of volume of gas mixture and solid particles.

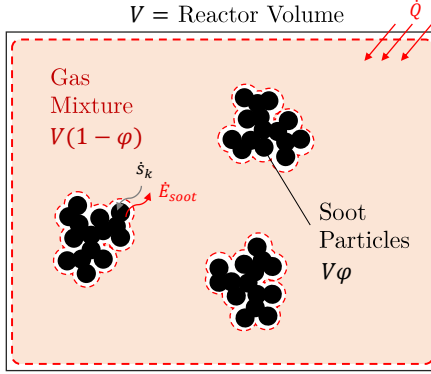


Figure 2.1: The schematics of control volume considered for the constant volume reactor that encompasses the gas mixture and excludes the soot particles. Mass and energy are transferred between gas and soot particles.

The continuity for this reactor can be written as:

$$\frac{d}{dt}(\rho(1 - \varphi)) = (1 - \varphi) \sum_i \dot{s}_i W_i. \quad (2.10)$$

Similarly, the species equation for species  $k$  is expressed as:

$$\frac{dY_k}{dt} = \frac{1}{\rho} (\dot{\omega}_k + \dot{s}_k) W_k - \frac{1}{\rho} Y_k \sum_i \dot{s}_i W_i. \quad (2.11)$$

<sup>1</sup>[https://cantera.org/documentation/docs-3.0/doxygen/html/d8/d58/classCantera\\_1\\_1GasTransport.html](https://cantera.org/documentation/docs-3.0/doxygen/html/d8/d58/classCantera_1_1GasTransport.html)

The energy balance for the gas mixture can be simplified to the rate of change of temperature. An external heat source of  $\dot{Q}$  is considered to account for possible heat loss/gain of the reactor.

$$\frac{dT}{dt} = \frac{1}{\rho(1-\varphi)c_v + \rho_{soot}\varphi c_{v,soot}} \left[ -(1-\varphi) \sum_k e_k (\dot{\omega}_k + \dot{s}_k) W_k + u_{soot}(1-\varphi) \sum_k \dot{s}_k W_k + \frac{\dot{Q}}{V} \right]. \quad (2.12)$$

The transport equation for a generic soot variable,  $\psi$  can be written as:

$$\frac{d\psi}{dt} = S_\psi - \frac{\psi}{\rho} \sum_i \dot{s}_i W_i. \quad (2.13)$$

### 2.3.2 Perfectly Stirred Reactor

In this reactor, gas enters with a mass flow rate  $\dot{m}_{in}$ , composition of  $Y^*$  and temperature of  $T^*$ , instantaneously mixes and homogeneously reacts with the mixture resident inside the reactor. The reacting gas reaches a spatially uniform temperature and composition described by  $T$ , and  $Y$ . It is assumed that temperature, composition and soot properties of the outflow are the same as reactor. Figure 2.2 illustrates the schematics of PSR.  $\dot{m}_{in}$  and  $\dot{m}_{out}$  refer to inflow and outflow gas mass flow rates, respectively. Under no-soot conditions, the inlet and outlet mass flow rates are equal, but the gas mixture loses mass by soot formation, so  $\dot{m}_{out}$  is slightly less than  $\dot{m}_{in}$ . The pressure of reactor is assumed to stay constant during the process [137]. The nominal residence time of gas mixture in the reactor is defined as:

$$\tau = \frac{\rho V}{\dot{m}_{in}}. \quad (2.14)$$

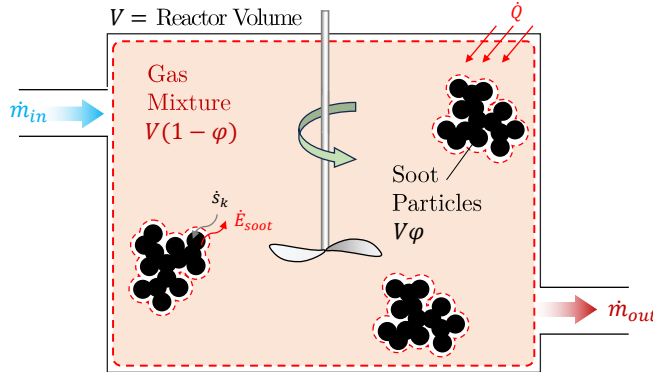


Figure 2.2: The schematics of control volume considered for the perfectly stirred reactor that encompasses the gas mixture and excludes the soot particles. Mass and energy are transferred between gas and soot particles. The inlet flow brings species and enthalpy into the control volume and the outflow discharges them. The outflow mass flow is less than inflow mass flow due to soot formation.

The conservation of mass can be written for PSR by considering the mass flux of in- and outflow, and the removal of mass due to soot generation as:

$$\frac{dm}{dt} = \dot{m}_{in} - \dot{m}_{out} + (1 - \varphi) \sum_i \dot{s}_i W_i. \quad (2.15)$$

The density is not determined by solving the continuity equation, but rather from ideal gas law and assuming a constant pressure and the composition from solving the species transport equations as:

$$\frac{dY_k}{dt} = \frac{1}{\tau} (Y_k^* - Y_k) + \frac{1}{\rho} \left[ (\dot{\omega}_k + \dot{s}_k) W_k - Y_k \sum_i \dot{s}_i W_i \right]. \quad (2.16)$$

The energy equation for this reactor is written as:

$$\frac{dT}{dt} = \frac{1}{\rho(1-\varphi)c_p + \rho_{soot}c_{p,soot}\varphi} \left[ \frac{\dot{m}_{in}}{V} (h^* - h) - \frac{\dot{m}_{in}}{V} \sum_k (Y_k^* - Y_k) h_k \right. \\ \left. - (1-\varphi) \sum_k (\dot{\omega}_k + \dot{s}_k) W_k h_k + (1-\varphi) \sum_i \dot{s}_i W_i h_{soot} + \frac{\dot{Q}}{V} \right]. \quad (2.17)$$

The soot transport equations can also be expressed as:

$$\frac{d\psi}{dt} = \frac{\dot{m}_{in}}{\rho V (1-\varphi)} (\psi^* - \psi) + S_\psi - \frac{1}{\rho} \psi \sum_i \dot{s}_i W_i. \quad (2.18)$$

### 2.3.3 Plug Flow Reactor

The plug flow reactor (PFR) is an ideal representation of a channel or duct with a constant cross-sectional area where a steady-state one-dimensional flow changes temperature, composition, and soot properties along the channel. There is no spatial gradient over the cross-section due to strong mixing. Diffusion along the channel is negligible. The pressure is assumed constant along the reactor.

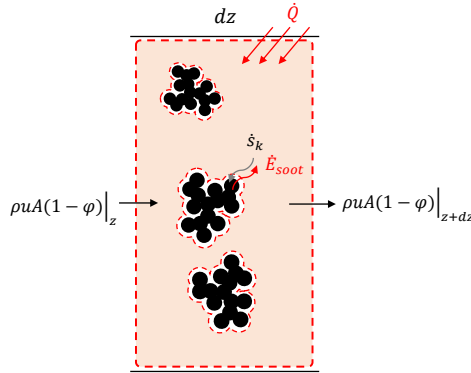


Figure 2.3: The schematics of control volume for a differential element along PFR that includes the gas mixture and excludes the soot particles considering wall heat transfer. Mass and energy are transferred between gas and soot.

The continuity equation for PFR is written as:

$$\frac{d}{dz}(\rho u(1-\varphi)) = (1-\varphi) \sum_i \dot{s}_i W_i. \quad (2.19)$$

The momentum equation can also be established as:

$$u(1-\varphi) \sum_i \dot{s}_i W_i + \rho u(1-\varphi) \frac{du}{dz} = -\frac{d}{dz}(P(1-\varphi)) - \frac{\tau_w}{R_H}. \quad (2.20)$$

where  $\tau_w$  is the wall shear stress can be determined from fraction factor,  $f$  as:

$$\tau_w = \frac{1}{2} \rho u^2 f. \quad (2.21)$$

The friction factor,  $f$  can be calculated with a good accuracy for the entire range of Reynolds number,  $Re$ , from laminar to turbulent flow using the explicit formula given by Haaland [138]:

$$\frac{1}{f^{1/2}} = -1.8 \log \left( \frac{6.9}{Re} + \left[ \frac{\epsilon/D_H}{3.7} \right]^{1.11} \right), \quad (2.22)$$

where  $\epsilon$  is the roughness of reactor wall.  $R_H$  and  $D_H$  are hydraulic radius and diameter, respectively that can be determined from cross-section geometry of reactor as:

$$D_H = 4R_H = \frac{4A_c}{P_c}, \quad (2.23)$$

$A_c$  and  $P_c$  are cross-sectional area and wetted perimeter of the reactor. The species equation can be expressed as:

$$\frac{dY_k}{dz} = \frac{1}{\rho u} \left[ (\dot{\omega}_k + \dot{s}_k) W_k - Y_k \sum_i \dot{s}_i W_i \right]. \quad (2.24)$$

The energy equation can be expressed as:

$$\frac{dT}{dz} = \frac{1}{\rho u (1 - \varphi) c_p + \rho_{soot} u \varphi c_{p, soot}} \left[ -(1 - \varphi) \sum_k h_k (\dot{\omega}_k + \dot{s}_k) W_k + h_{soot} (1 - \varphi) \sum_k \dot{s}_k W_k + \dot{q}' \right]. \quad (2.25)$$

The soot transport equations can also be written as:

$$\frac{d\psi}{dz} = \frac{S_\psi}{u} - \frac{\psi}{\rho u} \sum_i \dot{s}_i W_i. \quad (2.26)$$

## 2.4 Particle Dynamics

Population balance models rely on the Eulerian description of particles where bulk properties of particle population such as number density, mass or surface area are treated as continuous quantities and tracked by solving scalar transport equations. These methods are computationally cheaper compared with mesoscale models such as DEM, and can be easily interfaced with chemical kinetics in CFD solvers to simulate soot formation in turbulent configurations. Here, we use two particle dynamics models: a monodisperse population balance model (MPBM) based on four variables leading to 4 transport equations in total, and a fixed sectional population balance model (SPBM) tracking three variables per section. The total number of transport equations in the sectional model is determined by the number of sections and number of equations solved per section. The first two/three variables in the MPBM/SPBM enables description of number, mass, and evolving fractal-like morphology of soot agglomerates that are necessary to accurately predict collision frequency of agglomerates [139] as well as oxidation and surface growth rates [79]. The last variable tracks the number of hydrogen atoms in agglomerates that allows the model to capture the soot composition, thereby its maturity [45], and surface reactivity [86]. The tracked variables are used to address particle dynamics that includes (i) reconstructing particles morphology by determining characteristic diameters from tracked soot variables, (ii) calculating collision frequency and coagulation source term, (iii) combining the contribution of inception, PAH adsorption, surface growth and oxidation into source terms. First, common features of both particle dynamics models are reviewed. As mentioned before, any parameter with superscript  $i$  denotes the section number, which can be ignored/dropped for the MPBM that only has one section. For example,  $d_m^i$  can be replaced with  $d_m$ .

### 2.4.1 Soot Morphology

The evolving fractal-like structure of agglomerates is quantified by their mobility diameter normalized by primary particle,  $d_m/d_p$ , and gyration,  $d_m/d_g$ , diameters that can be described with

power-laws derived from mesoscale simulations. Incipient soot is initially a sphere formed of PAHs with constant density that grows in size by surface reactions and forms agglomerates by coagulation. The collision frequency of particles depends on their evolving fractal-like structure [139]. Some simplifying assumptions are made to reconstruct the particle morphology from tracked variables. The primary particles of each agglomerate are similar enough that can be described by mean size and composition. They also stay in point contact during surface growth and agglomeration i.e. the necking is ignored. Mobility and gyration diameters are the diameter of a sphere with the same translational and rotational properties of the agglomerate, respectively. The employed power-laws have been shown to describe the morphology of soot from premixed [80], diffusion [140] flames, and diesel engines [141]. Figure 2.4 illustrates the schematics of a soot agglomerates with 12 primary particles and depicted  $d_p$ ,  $d_m$ , and  $d_g$ .

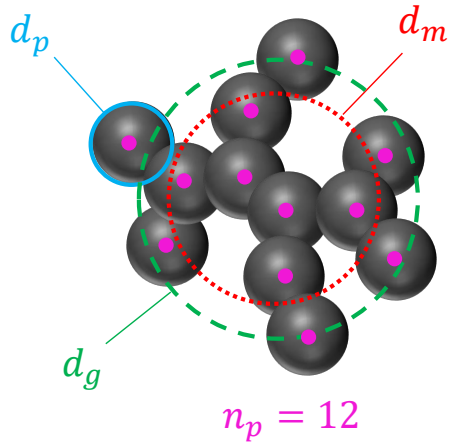


Figure 2.4: The schematics of a soot agglomerates with 12 primary particles ( $n_p = 12$ ). Primary particle ( $d_p$ ), mobility ( $d_m$ ), and gyration ( $d_g$ ) are shown.

$n_p^i$  is the number of primary particles per agglomerate for  $i^{\text{th}}$  section that can be obtained by dividing the number density of primary particles by the the number density of agglomerates of that section as:

$$n_p^i = \frac{N_{pri}^i}{N_{agg}^i}. \quad (2.27)$$

Primary particle diameter,  $d_p^i$ , can be obtained from total carbon content and number density of primary particles using

$$d_p^i = \left( \frac{6 C_{tot}^i \cdot W_{carbon}}{\pi \rho_{soot}} \frac{1}{N_{pri}^i \cdot Av} \right)^{1/3}. \quad (2.28)$$

The DEM-derived power-laws [66] relate  $d_m^i$  and  $d_g^i$  to  $d_p^i$  and  $n_p^i$  as

$$d_m^i = d_p^i \cdot n_p^i^{0.45}, \quad (2.29)$$

$$d_g^i = \begin{cases} d_m^i / (n_p^i^{-0.2} + 0.4), & \text{if } n_p^i > 1.5 \\ d_m^i / 1.29, & \text{if } n_p^i \leq 1.5 \end{cases} \quad (2.30)$$

The collision diameter,  $d_c^i$  is the maximum of  $d_m^i$ ,  $d_g^i$ :

$$d_c^i = \max(d_m^i, d_g^i) \quad (2.31)$$

$d_m^i$ ,  $d_g^i$ ,  $d_c^i$  are used to calculate the source terms due to the surface growth, oxidation, PAH adsorption and coagulation. The volume equivalent diameter,  $d_v^i$ , is the diameter of the sphere with the same mass as agglomerate, and it is obtained as:

$$d_v^i = d_p^i \cdot n_p^i{}^{1/3} \quad (2.32)$$

The primary particle surface area is calculated from  $d_p^i$  assuming spherical primary particles.

$$A_p^i = \pi d_p^i{}^2, \quad (2.33)$$

$A_{tot}^i$  (for each section) is defined as the total surface area of soot particles per unit mass of gas mixture obtained as

$$A_{tot}^i = N_{pri}^i \cdot Av \cdot A_p^i. \quad (2.34)$$

### 2.4.2 Diffusion of soot particles

The diffusion coefficient of soot particle,  $D^i$ , is calculated as

$$D^i = \frac{k_B T}{f^i}, \quad (2.35)$$

where  $f^i$  is the friction factor of particles in gas,

$$f^i = \frac{3\pi\mu d_m^i}{C^i(d_m^i)}, \quad (2.36)$$

where  $C^i$  is the Cunningham function that corrects the friction factor given a diameter in the continuum regime for transition and free molecular regimes as:

$$C^i(d) = 1 + \frac{2\lambda}{d} \left( 1.21 + 0.4 \cdot \exp\left(\frac{-0.78d}{\lambda}\right) \right), \quad (2.37)$$

where  $\lambda$  is the mean free path of gas given as:

$$\lambda = \frac{\mu}{\rho} \sqrt{\frac{\pi W_{gas}}{2k_B AvT}}. \quad (2.38)$$

Note that,  $\lambda$  is a property of the gas mixture that does not depend on particle morphology and size section. The mean velocity,  $c^i$  and mean stop distance of particles,  $\lambda_a^i$  can be calculated as:

$$c^i = \sqrt{\frac{8k_B T}{\pi m_{agg}^i}}. \quad (2.39)$$

$$\lambda_a = \frac{8D^i}{\pi c^i}. \quad (2.40)$$

The mean distance of particles are also calculated as:

$$\delta_a^i = \frac{1}{d_c^i \lambda_a^i} \left[ (d_c^i + \lambda_a^i)^3 - (d_c^i{}^2 + \lambda_a^i{}^2)^{3/2} \right] - d_{c,j}. \quad (2.41)$$

### 2.4.3 Soot Composition

The composition of soot is characterized by their elemental carbon to hydrogen ratio (C/H) is a measure of soot maturity and increases from C/H < 2 for incipient soot [142] to 2 < C/H < 10 for nascent soot [143] and C/H > 20 for mature soot [93]. The soot agglomerates are assumed to have pure carbon graphitic core [45] with all hydrogen atoms on the surface [86]. C/H ratio can be obtained from total carbon and hydrogen content as:

$$\left(\frac{C}{H}\right)^i = \frac{C_{tot}^i}{H_{tot}^i}. \quad (2.42)$$

The carbon content of each agglomerate is a predefined parameter in the SPBM (depending on the section the agglomerate is placed), but it can be calculated from dividing  $C_{tot}$  by  $N_{agg}$  for the MPBM. The hydrogen content of each agglomerate is calculated for both particle dynamics models as:

$$H_{agg}^i = \frac{H_{tot}^i}{N_{agg}^i}. \quad (2.43)$$

#### 2.4.4 Monodisperse Population Balance Model

The MPBM used in this research tracks the number density of primary particles ( $N_{pri}$ ) and agglomerates ( $N_{agg}$ ), total carbon ( $C_{tot}$ ) and hydrogen ( $H_{tot}$ ) content of soot particles per unit mass of gas mixture. The morphological parameters such as primary particle, mobility and gyration diameters obtained from these soot variables are the average values for the population.

##### 2.4.4.1 Coagulation

Coagulation is the process during which solid and hard soot particles collide and attach at point of contact leading to larger agglomerates. This process conserves the soot mass and composition and number density of primary particles, so coagulation only affects  $N_{agg}$ .  $I_{coag}^N$  accounts for the decay rate of  $N_{agg}$  by the binary collision of soot particles by

$$I_{coag} = -\frac{1}{2}\beta N_{agg}^2, \quad (2.44)$$

where  $\beta$  is the collision frequency of agglomerates for the free molecular ( $Kn > 10$ ) to continuum regime ( $Kn < 0.1$ ). The value of  $\beta$  in the transition regime ( $0.1 < Kn < 10$ ) can be calculated from the harmonic mean of the continuum ( $\beta_{cont}$ ) and free molecular ( $\beta_{fm}$ ) regime values. Additionally, an enhancement factor of %82 is applied to take into account the effect of polydispersity [67] as:

$$\beta = 1.82 \frac{\beta_{fm} \beta_{cont}}{\beta_{fm} + \beta_{cont}}, \quad (2.45)$$

$$\beta_{fm} = 4 \sqrt{\frac{\pi k_b T}{m_{agg}}} d_c^2, \quad (2.46)$$

$$\beta_{cont} = 8\pi d_c D. \quad (2.47)$$

Alternatively,  $\beta$  can be obtained using Fuchs interpolation [144] as:

$$\beta = \beta_{cont} \left( \frac{d_c}{d_c + 2\sqrt{2}\delta} + \frac{8D}{\sqrt{2}c_r d_c} \right)^{-1}. \quad (2.48)$$

##### 2.4.4.2 Source terms

The source terms of tracked variables combines the effect of the inception, PAH adsorption, surface growth and oxidation and coagulation.

$$S_{N_{agg}} = \frac{I_{N,inc}}{n_{c,min}} + I_{coag}. \quad (2.49)$$

$$S_{N_{pri}} = \frac{I_{N,inc}}{n_{c,min}}. \quad (2.50)$$

$$S_{C_{tot}} = I_{C_{tot},inc} + I_{C_{tot},gr} + I_{C_{tot},ads} + I_{C_{tot},ox}. \quad (2.51)$$

$$S_{H_{tot}} = I_{H_{tot},inc} + I_{H_{tot},gr} + I_{H_{tot},ads} + I_{H_{tot},ox}. \quad (2.52)$$

The partial source terms in Equations 2.49-2.52 denoted by I are determined by PAH growth and surface reaction model explained in Sections 2.6 and 2.5, respectively.

### 2.4.5 Sectional Population Balance Model

A SPBM with the fixed pivot is used to describe particle dynamics [145]. The mass range of particles are divided into discrete sections each of which includes agglomerates of the same mass. Inception introduces new particles to the first section with the mass corresponding to the incipient particle. The particles of first section can migrate to upper sections by gaining mass via surface growth and coagulation, and return to lower sections when they lose mass through oxidation. The mass of sections is determined by a geometric progression with a scale factor equal to the mass of incipient soot particle, and a common ratio of SF, known as sectional spacing factor. The mass of each section is approximated by the carbon content of agglomerates in moles as:

$$C_{agg}^i = \frac{n_{c,min}}{Av} \cdot SF^{(i-1)}. \quad (2.53)$$

where (i-1) represents the exponent of SF. The mass of hydrogen is ignored in the placement of agglomerates in the sections. The total number density of agglomerates,  $N_{agg}^i$  [mol/kg], and primary particles,  $N_{pri}^i$  [mol/kg] are tracked for each section. Morphological parameters are determined for each section according to the equations in Section 2.4.1.

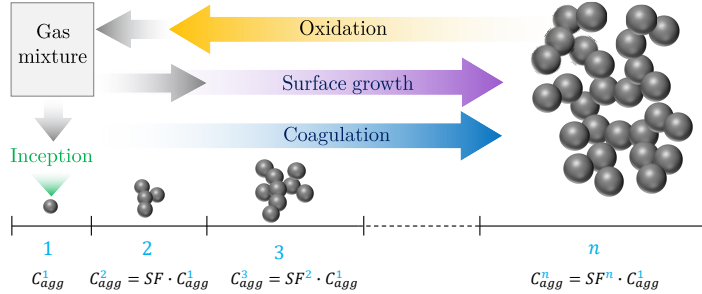


Figure 2.5: The illustration of sections of SPBM. The mass of sections grows progressively by the scale factor of SF. Inception introduces new particles to the first section that propagate to the upper section via coagulation and surface growth and return to lower sections by oxidation. Carbon and hydrogen pass from gas to solid phase through inception and surface growth and goes back via oxidation.

#### 2.4.5.1 Coagulation

In SPBM approach, collisions between particles from every two sections are considered. The new particles formed by coagulation are placed in an upper section with the mass equal to sum of mass of particles involved in the collision. When the mass of yielded particle lies between two consecutive sections, the particles are divided among these sections proportional to their mass. One possible scenario is that the mass of the newly formed particle is greater than the last section, thus leaving tracked mass range. Losing mass is a potential problem with the fixed pivot sectional model, which can be avoided by selecting proper number of sections and spacing factor to ensure the last sections stay empty during the simulation.

The collision frequency between sections j and k can be obtained from the harmonic mean of the values in the continuum and free molecular regimes as:

$$\beta^{jk} = \frac{\beta_{fm}^{jk} \beta_{cont}^{jk}}{\beta_{fm}^{jk} + \beta_{cont}^{jk}}, \quad (2.54)$$

$$\beta_{fm}^{jk} = \sqrt{\frac{\pi k_B T}{2} \left( \frac{1}{m_{agg}^j} + \frac{1}{m_{agg}^k} \right) (d_c^j + d_c^k)^2}, \quad (2.55)$$

$$\beta_{cont}^{ij} = \frac{2k_B T}{3\mu} \left( \frac{C^j}{d_m^j} + \frac{C^k}{d_m^k} \right) (d_c^j + d_c^k)^2. \quad (2.56)$$

The collision frequency can also be determined from the Fuchs interpolation similar to the MPBM as:

$$\beta^{jk} = \beta_{cont}^{ij} \left[ \frac{d_c^j + d_c^k}{d_c^j + d_c^k + 2 + \delta_r^{jk}} + \frac{8(D^j + D^k)}{\bar{c}_r^{jk} (d_c^j + d_c^k)} \right]^{-1}, \quad (2.57)$$

where  $\delta_r^{jk}$  and  $\bar{c}_r^{jk}$  are the mean square root of mean distance and velocity of particles, respectively.

$$\delta_r^{jk} = \sqrt{\delta_a^{j2} + \delta_a^{k2}}, \quad (2.58)$$

$$\bar{c}_r^{jk} = \sqrt{c^{j2} + c^{k2}}. \quad (2.59)$$

Coagulation redistributes the total number of agglomerates and primary particles as well as hydrogen atoms among the sections. The partial coagulation source terms for  $N_{agg}^i$ ,  $N_{pri}^i$  and  $H_{tot}^i$  can be calculated as:

$$I_{N_{agg}}^i = \sum_{k=1}^{n_{sec}} \sum_{j=k}^{n_{sec}} \left( 1 - \frac{\delta_{jk}}{2} \right) \eta_{ijk} \beta^{jk} N_{agg}^j N_{agg}^k - N_{agg}^i \sum_{k=1}^{n_{sec}} \beta^{im} N_{agg}^m. \quad (2.60)$$

$$I_{N_{pri}}^i = \sum_{k=1}^{n_{sec}} \sum_{j=k}^{n_{sec}} \left( 1 - \frac{\delta_{jk}}{2} \right) \eta_{p,ijk} \eta_{ijk} \beta^{jk} N_{agg}^j N_{agg}^k - N_{pri}^i \sum_{k=1}^{n_{sec}} \beta^{im} N_{agg}^m. \quad (2.61)$$

$$I_{H_{tot}}^i = \sum_{k=1}^{n_{sec}} \sum_{j=k}^{n_{sec}} \left( 1 - \frac{\delta_{jk}}{2} \right) \eta_{h,ijk} \eta_{ijk} \beta^{jk} N_{agg}^j N_{agg}^k - H_{tot}^i \sum_{k=1}^{n_{sec}} \beta^{im} N_{agg}^m. \quad (2.62)$$

where  $\delta_{jk}$  is the Kronecker delta defined as:

$$\delta_{jk} = \begin{cases} 1, & \text{if } j = k \\ 0, & \text{if } j \neq k \end{cases} \quad (2.63)$$

In Equation (2.60),  $\eta_{ijk}$  assigns newly formed agglomerates to the two consecutive sections in order to conserve mass during coagulation [71].

$$\eta_{ijk} = \begin{cases} \frac{C_{agg}^{i+1} - C_{agg}^{jk}}{C_{agg}^{i+1} + C_{agg}^{jk}}, & \text{if } C_{agg}^i \leq C_{agg}^{jk} < C_{agg}^{i+1} \\ \frac{C_{agg}^i - C_{agg}^{jk}}{C_{agg}^i + C_{agg}^{i-1}}, & \text{if } C_{agg}^{i-1} \leq C_{agg}^{jk} < C_{agg}^i \\ 0 & \text{else} \end{cases} \quad (2.64)$$

where  $C_{agg}^{jk} = C_{agg}^j + C_{agg}^k$ . Similarly,  $\eta_{p,ijk}$  in Equation (2.61) and  $\eta_{h,ijk}$  in Equation (2.62) adjust the number of primary particles and hydrogen atoms added to consecutive sections based on their mass, respectively.

$$\eta_{p,ijk} = \frac{C_{agg}^i}{C_{agg}^{jk}} (n_p^j + n_p^k), \quad (2.65)$$

$$\eta_{h,ijk} = \frac{C_{agg}^i}{C_{agg}^{jk}} (H_{agg}^j + H_{agg}^k), \quad (2.66)$$

### 2.4.5.2 Source terms

The source terms are split into four parts showing the contribution of different soot formation and evolution factors. The effect of surface growth and PAH adsorption are combined (denoted by the subscript gr,ads) because they are similar mass-gaining mechanisms.

$$S_{N_{agg}} = (S_{N_{agg}})_{inc} + (S_{N_{agg}})_{gr,ads} + (S_{N_{agg}})_{ox} + (S_{N_{agg}})_{coag}, \quad (2.67)$$

$$S_{N_{pri}} = (S_{N_{pri}})_{inc} + (S_{N_{pri}})_{gr,ads} + (S_{N_{pri}})_{ox} + (S_{N_{pri}})_{coag}, \quad (2.68)$$

$$S_{H_{tot}} = (S_{H_{tot}})_{inc} + (S_{H_{tot}})_{gr,ads} + (S_{H_{tot}})_{ox} + (S_{H_{tot}})_{coag}. \quad (2.69)$$

Inception introduces equal number of agglomerates and primary particles to the first section.

$$(S_{N_{agg}})_{inc} = \frac{1}{Av} \frac{I_{N,inc}}{C_{agg}^i}, \quad i = 1. \quad (2.70)$$

$$(S_{N_{pri}})_{inc} = \frac{1}{Av} \frac{I_{N,inc}}{C_{agg}^i}, \quad i = 1. \quad (2.71)$$

$$(S_{H_{tot}})_{inc} = I_{H,inc}, \quad i = 1. \quad (2.72)$$

Surface growth and PAH adsorption increase the (carbon) mass and hydrogen content of agglomerates, and transfer them to upper sections. The removal rate of agglomerates ( $N_{agg}^i$ ) from the original section due to surface growth and PAH adsorption must be equal to the addition rate of agglomerates to the target section to conserve the mass, and it is calculated by dividing the mass growth rate by the difference of the mass of the adjacent sections.

$$(S_{N_{agg}})_{gr,ads} = \frac{1}{Av} \begin{cases} -\frac{I_{C_{tot},gr}^i + I_{C_{tot},ads}^i}{C_{agg}^{i+1} - C_{agg}^i} & \text{if } i = 1 \\ \frac{I_{C_{tot},gr}^{i-1} + I_{C_{tot},ads}^{i-1}}{C_{agg}^i - C_{agg}^{i-1}} - \frac{I_{C_{tot},gr}^i + I_{C_{tot},ads}^i}{C_{agg}^{i+1} - C_{agg}^i} & \text{if } 1 < i < n_{sec} \\ \frac{I_{C_{tot},gr}^{i-1} + I_{C_{tot},ads}^{i-1}}{C_{agg}^i - C_{agg}^{i-1}} & \text{if } i = n_{sec} \end{cases} \quad (2.73)$$

As agglomerates move up/down through sections, they carry the number of primary particles as well as hydrogen atoms, so the transfer rate of agglomerates is multiplied by  $n_p^i$  and  $H_{agg}^i$ , respectively.

$$(S_{N_{pri}})_{gr,ads} = \frac{1}{Av} \begin{cases} -\frac{I_{C_{tot},gr}^i + I_{C_{tot},ads}^i}{C_{agg}^{i+1} - C_{agg}^i} & \text{if } i = 1 \\ \frac{I_{C_{tot},gr}^{i-1} + I_{C_{tot},ads}^{i-1}}{C_{agg}^i - C_{agg}^{i-1}} n_p^{i-1} - \frac{I_{C_{tot},gr}^i + I_{C_{tot},ads}^i}{C_{agg}^{i+1} - C_{agg}^i} n_p^i & \text{if } 1 < i < n_{sec} \\ \frac{I_{C_{tot},gr}^{i-1} + I_{C_{tot},ads}^{i-1}}{C_{agg}^i - C_{agg}^{i-1}} n_p^{i-1} & \text{if } i = n_{sec} \end{cases} \quad (2.74)$$

$$(S_{H_{tot}})_{gr,ads} = \frac{1}{Av} \begin{cases} -\frac{I_{C_{tot},gr}^i + I_{C_{tot},ads}^i}{C_{agg}^{i+1} - C_{agg}^i} H_{agg}^i + I_{H_{tot},gr}^i + I_{H_{tot},ads}^i & \text{if } i = 1 \\ \frac{I_{C_{tot},gr}^{i-1} + I_{C_{tot},ads}^{i-1}}{C_{agg}^i - C_{agg}^{i-1}} H_{agg}^{i-1} - \frac{I_{C_{tot},gr}^i + I_{C_{tot},ads}^i}{C_{agg}^{i+1} - C_{agg}^i} H_{agg}^i + I_{H_{tot},gr}^i + I_{H_{tot},ads}^i & \text{if } 1 < i < n_{sec} \\ \frac{I_{C_{tot},gr}^{i-1} + I_{C_{tot},ads}^{i-1}}{C_{agg}^i - C_{agg}^{i-1}} H_{agg}^{i-1} + I_{H_{tot},gr}^i + I_{H_{tot},ads}^i & \text{if } i = n_{sec} \end{cases} \quad (2.75)$$

Similarly, the agglomerates lose (carbon) mass by oxidation, and descend to the lower sections carrying primary particle and hydrogen.

$$(S_{N_{agg}})_{ox} = \frac{1}{Av} \begin{cases} \frac{I_{C_{tot},ox}^{i+1}}{C_{agg}^{i+1} - C_{agg}^i} - \frac{I_{C_{tot},ox}^i}{C_{agg}^i} & \text{if } i = 1 \\ \frac{I_{C_{tot},ox}^{i+1}}{C_{agg}^{i+1} - C_{agg}^i} - \frac{I_{C_{tot},ox}^i}{C_{agg}^i - C_{agg}^{i-1}} & \text{if } 1 < i < n_{sec} \\ -\frac{I_{C_{tot},ox}^i}{C_{agg}^i - C_{agg}^{i-1}} & \text{if } i = n_{sec} \end{cases} \quad (2.76)$$

$$(S_{N_{pri}})_{ox} = \frac{1}{Av} \begin{cases} \frac{I_{C_{tot},ox}^{i+1}}{C_{agg}^{i+1} - C_{agg}^i} n_p^{i+1} - \frac{I_{C_{tot},ox}^i}{C_{agg}^i} & \text{if } i = 1 \\ \frac{I_{C_{tot},ox}^{i+1}}{C_{agg}^{i+1} - C_{agg}^i} n_p^{i+1} - \frac{I_{C_{tot},ox}^i}{C_{agg}^i - C_{agg}^{i-1}} n_p^i & \text{if } 1 < i < n_{sec} \\ -\frac{I_{C_{tot},ox}^i}{C_{agg}^i - C_{agg}^{i-1}} n_p^i & \text{if } i = n_{sec} \end{cases} \quad (2.77)$$

$$(S_{H_{tot}})_{ox} = \frac{1}{Av} \begin{cases} \frac{I_{C_{tot},ox}^{i+1}}{C_{agg}^{i+1} - C_{agg}^i} H_{agg}^{i+1} - \frac{I_{C_{tot},ox}^i}{C_{agg}^i} H_{agg}^i + I_{H_{tot},ox}^i & \text{if } i = 1 \\ \frac{I_{C_{tot},ox}^{i+1}}{C_{agg}^{i+1} - C_{agg}^i} H_{agg}^{i+1} - \frac{I_{C_{tot},ox}^i}{C_{agg}^i - C_{agg}^{i-1}} H_{agg}^i + I_{H_{tot},ox}^i & \text{if } 1 < i < n_{sec} \\ -\frac{I_{C_{tot},ox}^i}{C_{agg}^i - C_{agg}^{i-1}} H_{agg}^i + I_{H_{tot},ox}^i & \text{if } i = n_{sec} \end{cases} \quad (2.78)$$

## 2.5 Surface reactions model

The heterogeneous surface reactions are described by hydrogen-abstraction-acetylene-addition (HACA) mechanism [40, 58]. The soot growth in HACA scheme is based on a sequential process similar to PAH growth. The hydrogenated arm-chair sites ( $C_{soot} - H$ ) on the edge of aromatic rings are dehydrogenated by H abstraction forming  $C_{soot}^\circ$  that bonds with  $C_2H_2$  resulting in an additional aromatic ring with hydrogenated site. These sites can also be attacked by  $O_2$  or  $OH$ . The elementary reactions that describe this sequential process are listed in Table 2.1. The rate of mass growth by HACA is obtained from the reaction of  $C_2H_2$  with dehydrogenated sites as:

$$\omega_{gr}^i = \alpha^i k_{f4}[C_2H_2][C_{soot}^\circ]. \quad (2.79)$$

where  $k_{f4}$  denotes the forward rate of Reaction 2.1 in Table 2.1, and  $[C_{soot}^\circ]$  is obtained by multiplying the surface density of dehydrogenated sites,  $\chi_{soot}^\circ$  with total surface area of soot (per unit of mass of gas mixture) as:

$$[C_{soot}^i] = \frac{\rho}{Av} A_{tot}^i \cdot \chi_{soot}^i. \quad (2.80)$$

$\chi_{soot}^i$  is calculated by assuming the steady-state for  $[C_{soot}^i]$  in the system of reactions in Table 2.1:

$$\chi_{soot}^i = \frac{k_f1[H] + k_f2[OH]}{k_{r1}[H_2] + k_{r2}[H_2O] + k_{f3}[H] + k_{f4}[C_2H_2] + k_{f5}[O_2] + k_{f1}[H] + k_{f2}[OH]} \chi_{soot_{CH}}, \quad (2.81)$$

where  $\chi_{soot_{CH}}$  is the surface density of hydrogenated sites estimated based on the assumption that soot surface is covered with stacks of benzene rings [58]. Considering the stack spacing of 3.15 Å and 2 C–H bonds per benzene ring length, the surface density of hydrogenated sites,  $\chi_{soot-H}$ , is calculated to be  $0.23 \text{ site}/\text{\AA}^2 = 2.3 \times 10^{19} \text{ site}/\text{m}^2$ , which gives the maximum theoretical limit of the reaction sites.

In Equation (2.79),  $\alpha$  is the surface reactivity factor between 0 and 1 that represents the decline of reaction sites from the theoretical limit due to particle aging, growth and maturity [146, 147], and it has been observed to depend on temperature time history [148, 60]. The value of  $\alpha$  has been described using constant target-specific values as well as empirical equations based on particle size and flame temperature. A detailed review of these can be found in the chapter 4 of [149]. Here, the empirical equations proposed by Appel et al. [58] is used to calculate  $\alpha$ :

$$\alpha^i = \tanh \left( \frac{12.56 - 0.00563 \cdot T}{\log_{10} \left( \frac{\rho_{soot} \cdot Av}{W_{carbon}} \frac{\pi}{6} d_p^3 \right)} - 1.38 + 0.00068 \cdot T \right). \quad (2.82)$$

Alternatively, Blanquart and Pitsch [85] related  $\alpha$  to the number of surface hydrogen atoms on the soot particles.

$$\alpha^i = \frac{H_{tot}^i}{C_{tot}^i}. \quad (2.83)$$

The contribution of HACA to growth source terms can be computed from HACA rates considering the number of carbon atoms in  $C_2H_2$  and number of arm-chair and zig-zag hydrogenated sites on soot particle [86] using

$$I_{C_{tot},gr}^i = 2\omega_{gr}^i / \rho, \quad (2.84)$$

$$I_{H_{tot},gr}^i = 0.25\omega_{gr}^i / \rho. \quad (2.85)$$

The rate change of  $C_2H_2$  concentration due to mass growth is written as:

$$\left( \frac{d[C_2H_2]}{dt} \right)_{gr} = - \sum_{i=1}^{n_{sec}} \omega_{gr}^i. \quad (2.86)$$

The rate of release of H radicals into the gas mixture due to surface growth is:

$$\left( \frac{d[H]}{dt} \right)_{gr} = 1.75 \sum_{i=1}^{n_{sec}} \omega_{gr}^i. \quad (2.87)$$

The carbons on the surface of soot are oxidized via reaction with  $O_2$  and  $OH$  which decreases total carbon of soot and releases  $CO$  and  $H_2$  to gas mixture. The oxidation process is described by HACA mechanism.  $O_2$  and  $OH$  oxidation rates are calculated as

$$\omega_{ox,O_2}^i = \alpha^i k_{f5}[O_2][C_{soot}^i], \quad (2.88)$$

$$\omega_{ox,OH}^i = \alpha^i k_{f6}[OH][soot^i]. \quad (2.89)$$

The oxidation source term is calculated considering the number of carbon atoms removed from soot through each oxidation pathway by

Table 2.1: Rate coefficients for the various surface reactions in Arrhenius form  $k = AT^n \cdot e^{-E/RT}$ 

No.	Reaction		A $\left[ \frac{\text{m}^3}{\text{mol} \cdot \text{s}} \right]$	n	$\frac{E}{R} [\text{K}]$
(R 2.1)	$\text{C}_{\text{soot}-\text{H}} + \text{H} \rightleftharpoons \text{C}_{\text{soot}^\circ} + \text{H}_2$	f	$4.17 \times 10^7$	0	6542.52
		r	$3.9 \times 10^6$	0	5535.98
(R 2.2)	$\text{C}_{\text{soot}-\text{H}} + \text{OH} \rightleftharpoons \text{C}_{\text{soot}^\circ} + \text{H}_2\text{O}$	f	$10^4$	0.734	719.68
		r	$3.68 \times 10^2$	1.139	8605.94
(R 2.3)	$\text{C}_{\text{soot}^\circ} + \text{H} \longrightarrow \text{C}_{\text{soot}} + \text{H}_2\text{O}$	f	$10^4$	0.734	719.68
(R 2.4)	$\text{C}_{\text{soot}^\circ} + \text{C}_2\text{H}_2 \longrightarrow \text{C}_{\text{soot}-\text{H}}$	f	80	1.56	1912.43
(R 2.5)	$\text{C}_{\text{soot}^\circ} + \text{O}_2 \longrightarrow 2 \text{CO}$	f	$2.2 \times 10^6$	0	3774.53
(R 2.6)	$\text{C}_{\text{soot}-\text{H}} + \text{OH} \longrightarrow \text{CO} + \frac{1}{2} \text{H}_2$	f	$1.3 \times 10^7$	0	0

$$I_{C_{tot},ox}^i = -(2\omega_{ox,O_2}^i + \omega_{ox,OH}^i)/\rho, \quad (2.90)$$

We assume that oxidation does not change the number of surface hydrogen atoms. The rate change of concentration of CO, H and OH by oxidation is calculated as:

$$\left( \frac{d[\text{CO}]}{dt} \right)_{ox} = \sum_{i=1}^{n_{sec}} \omega_{ox,O_2}^i. \quad (2.91)$$

$$\left( \frac{d[\text{O}_2]}{dt} \right)_{ox} = - \sum_{i=1}^{n_{sec}} \omega_{ox,O_2}^i. \quad (2.92)$$

$$\left( \frac{d[\text{OH}]}{dt} \right)_{ox} = - \sum_{i=1}^{n_{sec}} \omega_{ox,OH}^i. \quad (2.93)$$

$$\left( \frac{d[\text{H}_2]}{dt} \right)_{ox} = \frac{1}{2} \sum_{i=1}^{n_{sec}} \omega_{ox,OH}^i. \quad (2.94)$$

## 2.6 PAH growth models

Here, four different PAH growth models are used to describe the conversion of PAHs to incipient particles and their adsorption on existing agglomerates. As mentioned before, the soot inception and surface growth is not fully understood yet, but there is substantial evidence to support the collision of PAHs as a key step in inception and surface growth [27, 28, 29]. So, global inception models have been developed based PAH collision consisting of different pathways with single- or multi-step reactions. The collision frequency of gaseous species including PAH molecules and polymers depend on their mass and diameter, and it is obtained as:

$$\beta_{dim_{jk}} = 2.2 \cdot d_r^2 \sqrt{\frac{8\pi k_B T}{m_r}} \quad (2.95)$$

where  $d_r$  and  $m_r$  are reduced diameter and mass for two PAH molecules, respectively.

$$d_r = 2 \frac{d_{PAH_k} \cdot d_{PAH_j}}{d_{PAH_k} + d_{PAH_j}} \quad (2.96)$$

$$m_r = \frac{m_{PAH_k} \cdot m_{PAH_j}}{m_{PAH_k} + m_{PAH_j}} \quad (2.97)$$

The mass of each PAH molecule is obtained from its molecular weight as:

$$m_{PAH_j} = \frac{W_{PAH_j}}{Av} \quad (2.98)$$

The diameter of PAH is calculated from its mass and density.

$$d_{PAH_j} = \left( \frac{6 \cdot m_{PAH_j}}{\pi \cdot \rho_{PAH_j}} \right)^{1/3} \quad (2.99)$$

The density of a PAH molecule is estimated using the relation proposed by Johansson et al. [150].

$$\rho_{PAH_j} = 171943.5197 \frac{W_{carbon} \cdot n_{C,PAH_j} + W_{hydrogen} \cdot n_{H,PAH_j}}{n_{C,PAH_j} + n_{H,PAH_j}} \quad (2.100)$$

The collision frequency of  $PAH_j$  and soot agglomerates in each section can be determined for the entire regime by harmonic mean of the collision frequency in the free molecular and continuum regimes as:

$$\beta_{ads_j}^i = \frac{\beta_{fm,ads}^i \cdot \beta_{cont,ads}^i}{\beta_{fm,ads}^i + \beta_{cont,ads}^i} \quad (2.101)$$

$$\beta_{fm,ads_j}^i = 2.2 \sqrt{\frac{\pi k_B T}{2} \left( \frac{1}{m_{agg}^i} + \frac{1}{m_{PAH_j}} \right) (d_g^i + d_{PAH_j})^2} \quad (2.102)$$

$$\beta_{cont,ads_j}^i = \frac{2k_B T}{3\mu} \left[ \frac{C^i(d_m)}{d_g^i} + \frac{C^i(d_{PAH_j})}{d_{PAH_j}} \right] (d_g + d_{PAH_j}) \quad (2.103)$$

where  $C^i$  is the Cunningham function calculated by Equation 2.37.

### 2.6.1 Irreversible Dimerization

The irreversible dimerization is based on the irreversible collision of PAHs leading to their clustering/polymerization that forms dimers, trimers, and tetramers until the polymer mass reaches a threshold that can be considered a solid particle. For practical purposes, dimer is usually considered as a incipient particle that grows by surface growth and coagulation. A single-step irreversible collision of two similar PAHs forms a new dimer as:



Similarly, the adsorption of each PAH molecule on soot particles is described by the irreversible collision of soot and  $PAH_j$  as:



The forward rate of dimerization,  $k_{f,dim_j}$  and adsorption,  $k_{f,ads_j}$  in Reactions (R.2.7) and (R.2.8) are calculated from Equations (2.95) and (2.101), respectively.

$$k_{f,dim_j} = \gamma_{inc} \cdot \beta_{jk,PAH} \cdot Av, \quad (2.104)$$

$$k_{f,ads_j}^i = \gamma_{ads_j} \cdot \beta_{j,ads}^i \cdot Av, \quad (2.105)$$

where  $\gamma_{inc}$  and  $\gamma_{ads}$  are the collision efficiencies for dimerization and adsorption, respectively. Their value vary in the range of  $[10^{-7}, 1]$ , and are usually chosen to match the predicted soot mass with the experimental data. Here,  $\gamma_{inc} = 10^{-4}$  and  $\gamma_{ads} = 10^{-3}$ . The rate of dimerization and adsorption from  $PAH_j$  are calculated accordingly as:

$$w_{dim_j} = k_{f,dim_j} [PAH_j][PAH_j] \quad (2.106)$$

The partial source terms for inception are calculated as:

$$I_{N,inc} = \frac{1}{\rho} \sum_{j=1}^{n_{PAH}} w_{dim_j} 2n_{PAH_j,C} \quad (2.107)$$

$$I_{C_{tot},inc} = \frac{1}{\rho} \sum_{j=1}^{n_{PAH}} w_{dim_j} 2n_{PAH_j,C} \quad (2.108)$$

$$I_{H_{tot},inc} = \frac{1}{\rho} \sum_{j=1}^{n_{PAH}} w_{dim_j} 2n_{PAH_j,H} \quad (2.109)$$

The rate of PAH adsorption for each section is obtained as:

$$w_{ads_j}^i = k_{f,ads_j}^i [\text{soot}][PAH_j] \quad (2.110)$$

The contribution of PAH adsorption to the source terms are expressed as:

$$I_{C_{tot},ads}^i = \frac{1}{\rho} \sum_{j=1}^{n_{PAH}} w_{ads_j}^i n_{PAH,C} \quad (2.111)$$

$$I_{H_{tot},ads}^i = \frac{1}{\rho} \sum_{j=1}^{n_{PAH}} w_{dim_j}^i (n_{PAH,H} - 2) \quad (2.112)$$

Each PAH molecule loses one H atom becoming a radical that forms bonds with a dehydrogenated site on soot surface, so two H atoms are released during the process that is taken into account in Equation (2.112).

The formation of a dimer consumes two PAH molecules, and during adsorption one PAH molecule is removed from the gas mixture, so the total rate of PAH<sub>i</sub> removal by the irreversible dimerization is obtained as:

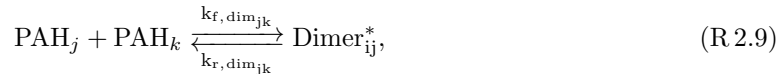
$$\left( \frac{d [PAH_j]}{dt} \right)_{inc} = -2w_{dim_j} - \sum_{i=1}^{n_{sec}} w_{ads_j}^i. \quad (2.113)$$

During the adsorption process one H<sub>2</sub> is released to the gas mixture.

$$\left( \frac{d [H_2]}{dt} \right)_{inc} = \sum_{i=1}^{n_{sec}} w_{ads_j}^i. \quad (2.114)$$

## 2.6.2 Reactive Dimerization

This model is built on Irreversible Dimerization with two main differences: The first step of dimerization and adsorption is reversible forming physically bonded dimers followed by a irreversible carbonization that leads to chemical bond formation in dimers [57]. This approach allows formation of homo- and heterodimers. The dimerization of PAH<sub>j</sub> and PAH<sub>k</sub> is described as:



where Dimer<sub>jk</sub><sup>\*</sup> and Dimer<sub>jk</sub> physically and chemically bonded dimers, respectively, from PAH<sub>j</sub> and PAH<sub>k</sub>. The forward rate of physical dimerization,  $k_{f,dim_{jk}}$  is calculated from Equation (2.95) as:

$$k_{f,dim_{jk}} = p'' \cdot \beta_{jk,PAH} \cdot Av, \quad (2.115)$$

where  $p'' = 0.1$  accounts for the probability of PAH-PAH collisions in “FACE” configuration that results in successful vdW bond formation [151]. The reverse rate of physical dimerization,  $k_{r,dim_{jk}}$  is obtained from the dimerization equilibrium constant [53] as:

$$\log_{10} K_{eq} = a \frac{\epsilon_{jk}}{RT} + b, \quad (2.116)$$

$$k_{r,dim_{jk}} = k_{f,dim_{jk}} 10^{-b} e^{-a\epsilon_{jk}\ln(10)/(RT)}, \quad (2.117)$$

$$\epsilon_{jk} = cW_{jk} - d, \quad (2.118)$$

$$W_{jk} = \frac{W_j \cdot W_k}{W_j + W_k}, \quad (2.119)$$

where  $a = 0.115$  (obtained from pyrere dimerization data [48]) and  $b=1.8$  [57],  $c=933420$  j/kg, and  $d=34053$  j/mol [57].

The rate of chemical bond formation,  $k_{reac}$  is defined in the Arrhenius form [49] as

$$k_{reac} = 5 \times 10^6 \cdot e^{(-96232/RT)}. \quad (2.120)$$

Assuming a steady state condition for the physical dimers,  $\partial[\text{Dimer}_{jk}^*]/\partial t = 0$ , the rate of formation of chemically-bonded dimers can be obtained as

$$\omega_{dim_{jk}} = k_{reac} \frac{k_{f,dim_{jk}} [\text{PAH}_j][\text{PAH}_k]}{k_{r,dim_{jk}} + k_{c,dim}}. \quad (2.121)$$

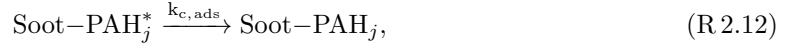
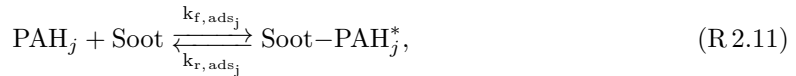
The contribution of dimer formation to partial source terms is expressed by looping over all combinations of PAHs as:

$$I_{N,inc} = \frac{1}{\rho} \sum_{j=1}^{n_{PAH}} \sum_{k=j}^{n_{PAH}} \omega_{dim_{kj}} (n_{PAH_j,C} + n_{PAH_k,C}), \quad (2.122)$$

$$I_{C_{tot},inc} = \frac{1}{\rho} \sum_{j=1}^{n_{PAH}} \sum_{k=j}^{n_{PAH}} \omega_{dim_{kj}} (n_{PAH_j,C} + n_{PAH_k,C}), \quad (2.123)$$

$$I_{H_{tot},inc} = \frac{1}{\rho} \sum_{j=1}^{n_{PAH}} \sum_{k=j}^{n_{PAH}} \omega_{dim_{kj}} (n_{PAH_j,H} + n_{PAH_k,H}), \quad (2.124)$$

Similarly, PAH adsorption is described by a two-step process where the collision of PAH<sub>j</sub> with soot agglomerates leads to physically bonded Soot – PAH\* that is carbonized and forms chemically-bonded Soot – PAH added to soot surface.



The forward rate of PAH-soot collision is calculated from Equation (2.101), and the reverse rate is determined same as inception (Equation(2.117)).

$$k_{f,ads}^i = \beta_{jk,ads}^i \cdot Av, \quad (2.125)$$

$$k_{r,ads}^i = k_{f,ads}^i \cdot 10^{-b} e^{-a\epsilon_{soot,j}\ln(10)/(RT)}, \quad (2.126)$$

$$\epsilon_{soot,j} = cW_{soot,j} - d, \quad (2.127)$$

a, b, c, d values are the same as those used in inception. Computing  $\epsilon_{soot,j}$  also requires "equivalent soot molecular weight",  $W_{soot}$  for section i, which is estimated from carbon mass of each agglomerate as:

$$W_{soot}^i = \frac{C_{tot}^i W_{carbon}}{N_{agg}^i} \quad (2.128)$$

The rate constant of carbonization of Soot – PAH<sub>j</sub><sup>\*</sup> is defined as in the Arrhenius form similar to inception (Equation (2.120)). The prefactor is adjusted based on matching the numerical PSD [49] with measurements in the ethylene pyrolysis in a flow reactor [152].

$$k_{c,dim} = 2 \times 10^{10} \cdot e^{(-96232/RT)}. \quad (2.129)$$

The total adsorption rate can be calculated assuming a steady-state concentration for physically adsorbed PAH on soot,  $\partial[\text{Soot} - \text{PAH}^*]/\partial t = 0$  calculated in a similar way to inception flux (Equation (2.121)) as

$$\omega_{ads_j}^i = k_{c,ads} \frac{k_{f,ads_j} [\text{Soot}][\text{PAH}_j]}{k_{r,ads_j} + k_{c,ads_j}}, \quad (2.130)$$

The contribution of PAH adsorption rate to partial source terms can be expressed as:

$$I_{C_{tot},ads}^i = \frac{1}{\rho} \sum_{i=1}^{n_{PAH}} \omega_{ads_j}^i n_{C,PAH_j}, \quad (2.131)$$

$$I_{C_{tot},ads}^i = \frac{1}{\rho} \sum_{i=1}^{n_{PAH}} \omega_{ads_j}^i (n_{H,PAH_j} - 2). \quad (2.132)$$

The rate of removal of PAH from gas mixture due to adsorption is given as

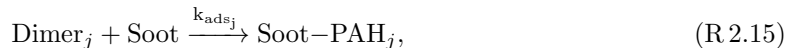
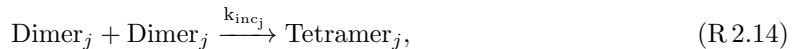
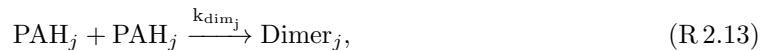
$$\left( \frac{d[\text{PAH}_j]}{dt} \right)_{inc} = - \sum_{k=1}^{n_{PAH}} w_{dim_{jk}} - \sum_{i=1}^{n_{sec}} w_{ads_j}^i. \quad (2.133)$$

During the adsorption process one H<sub>2</sub> is released to the gas mixture.

$$\left( \frac{d[\text{H}_2]}{dt} \right)_{inc} = \sum_{i=1}^{n_{sec}} w_{ads_j}^i. \quad (2.134)$$

### 2.6.3 Dimer Coalescence

Dimer coalescence model is a multi-step irreversible model proposed by Blanquart and Pitsch [85] where self-collision of PAH molecules form dimers that are intermediate state between gaseous PAH molecules and solid soot particles. The self-coalescence of dimers forms incipient soot particles. Alternatively, dimers can adsorb on the surface of existing soot particles and contribute to their surface growth. The equations are based on implementation of Dimer Coalescence by Sun et al. [153] for a sectional model.



where the rate constant of dimerization,  $k_{dim_j}$  and inception  $k_{inc_j}$  are calculated from collision rate of PAHs in Equation (2.101).

Table 2.2: The dimerization efficiency,  $\gamma_{\text{dim}_j}$ , for different PAH in dimer coalescence model [86]

Species name	Chemical formula	W [kg/mol]	$\gamma_{\text{dim}_j}$
Naphthalene	C <sub>10</sub> H <sub>8</sub>	0.128	0.002
Acenaphthylene	C <sub>12</sub> H <sub>8</sub>	0.152	0.004
Biphenyl	C <sub>12</sub> H <sub>10</sub>	0.154	0.0085
Phenanthrene	C <sub>14</sub> H <sub>10</sub>	0.178	0.015
Acephenanthrylene	C <sub>16</sub> H <sub>10</sub>	0.202	0.025
Pyrene	C <sub>16</sub> H <sub>10</sub>	0.202	0.025
Fluoranthene	C <sub>16</sub> H <sub>10</sub>	0.202	0.025
Cyclopenta[cd]pyrene	C <sub>18</sub> H <sub>10</sub>	0.226	0.039

$$k_{\text{dim}_j} = \gamma_{\text{dim}_j} \cdot \beta_{jj,PAH} \cdot Av, \quad (2.135)$$

$$k_{inc_j} = \beta_{jj,dimer} \cdot Av, \quad (2.136)$$

where  $\gamma_{\text{dim}_j}$  is the dimerization efficiency that is assumed to scale with fourth power of PAH molecular weight [86] as:

$$\gamma_{\text{dim}_j} = C_{N,j} \cdot W_{PAH_j}^4, \quad (2.137)$$

Blanquart and Pitsch [85] estimated the constant  $C_{N,j}$  by comparing the profiles of several PAH species with experimental measurements in a single premixed benzene flame [154], and provided efficiency values for various PAHs that are listed in Table 2.2. The rate of dimer collision is expressed as:

$$w_{\text{dim}_j} = k_{inc_j} [\text{Dimer}_j][\text{Dimer}_j] \quad (2.138)$$

Similarly, the rate of adsorption of dimers on soot particles is obtained as:

$$w_{ads_j}^i = k_{ads_j}^i [\text{soot}]^i [\text{Dimer}_j] \quad (2.139)$$

Assuming fast dimer consumption leads to the steady-state concentration of dimers that can be determined by solving a quadratic equation as:

$$a_{inc_j} [\text{dimer}]^2 + b_{ads_j} [\text{dimer}] = \omega_{\text{dim},j} \quad (2.140)$$

$$[\text{Dimer}_j] = \begin{cases} \frac{-b_{ads_j} + \sqrt{\Delta_j}}{2a_{inc_j}}, & \text{if } \Delta_j \geq 0 \\ 0 & \text{if } \Delta_j < 0 \end{cases} \quad (2.141)$$

$$\Delta_j = b_{ads_j}^2 - 4a_{inc_j}\omega_{\text{dim},j} \quad (2.142)$$

where  $a_{inc_j} = k_{inc_j}$  and  $b_{ads_j}$  is calculated by summing the adsorption rate of dimer for all sections and dividing it by the dimer concentration.

$$b_{ads_j} = \sum_{i=1}^{n_{sec}} k_{ads_j}^i [\text{soot}]^i \quad (2.143)$$

After determining the concentration of each dimer, the contribution of inception and PAH adsorption to source terms of tracked soot variables can be calculated similar to previous inception models considering the number of carbon and hydrogen atoms involved in the process.

$$I_{N,inc} = \frac{1}{\rho} \sum_{j=1}^{n_{PAH}} 4\omega_{inc_j} n_{PAH_j,C}, \quad (2.144)$$

$$I_{C_{tot},inc} = \frac{1}{\rho} \sum_{j=1}^{n_{PAH}} 4\omega_{inc_j} n_{PAH_j,C}, \quad (2.145)$$

$$I_{H_{tot},inc} = \frac{1}{\rho} \sum_{j=1}^{n_{PAH}} 4\omega_{inc_j} (n_{PAH_j,H} - 2), \quad (2.146)$$

$$I_{C_{tot},ads}^i = \frac{1}{\rho} \sum_{i=1}^{n_{PAH}} 2\omega_{ads_j}^i n_{C,PAH_j}, \quad (2.147)$$

$$I_{C_{tot},ads}^i = \frac{1}{\rho} \sum_{i=1}^{n_{PAH}} 2\omega_{ads_j}^i (n_{H,PAH_j} - 2). \quad (2.148)$$

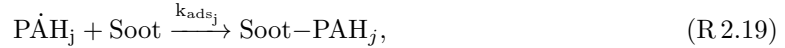
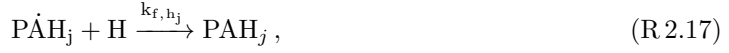
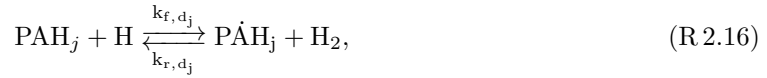
The rate of removal of PAHs and release of H<sub>2</sub> due to inception and PAH adsorption is calculated as:

$$\left( \frac{d [\text{PAH}_j]}{dt} \right)_{inc} = -4 \sum_{k=1}^{n_{PAH}} w_{inc_j} - 2 \sum_{i=1}^{n_{sec}} w_{ads_j}^i. \quad (2.149)$$

$$\left( \frac{d [\text{H}_2]}{dt} \right)_{inc} = 2 \sum_{i=1}^{n_{sec}} w_{ads_j}^i. \quad (2.150)$$

## 2.6.4 E-Bridge Formation

The E-Bridge Formation was originally proposed by Frenklach and Mebel [25] to describe soot inception using a HACA-like scheme that starts with dehydrogenation of PAH monomers, often pyrene, which forms the monomer radicals and continues with the sequential addition of the radicals to PAHs that form dimers, trimers and larger polymers until the PAH structure reaches the mass threshold and the clustering process becomes irreversible. Here, a modified version of EBridge Formation model is used where dimers are considered as incipient soot, and monomer radical are adsorbed on soot agglomerates. This PAH growth model is described using the following set of pathways:



The rate constants of Reactions (R 2.16)&(R 2.17) are listed in Table 2.3 while those of dimer production and adsorption are calculated based on Equations (2.95)&(2.101), respectively. For both steps, it is assumed that all collisions are successful i.e. 100% collision efficiency for radical-monomer and radical-soot.

Table 2.3: Rate coefficients for the monomer de-/hydrogenation reaction of E-bridge formation in Arrhenius form  $k = AT^n \cdot e^{-E/RT}$  [25]

Reaction	A	$\left[ \frac{m^3}{mol \cdot s} \right]$	n	$\frac{E}{R}[K]$
(R 2.16)	f	$98 \times n_{C,PAH_j}$	1.8	7,563.519
	r	$1.6 \times 10^{-2}$	2.63	2145.346
(R 2.17)	f	$4.8658 \times 10^7$	0.13	0.0

$$k_{inc_j} = \beta_{jj,PAH} \cdot Av, \quad (2.151)$$

$$k_{ads_j}^i = \beta_{ads_j}^i \cdot Av, \quad (2.152)$$

The rate of dimer formation and adsorption is calculated as:

$$w_{dim_j} = k_{inc_j} [\text{PAH}_j] [\dot{\text{PAH}}_j] \quad (2.153)$$

$$w_{ads_j}^i = k_{ads_j}^i [\text{Soot}]^i [\dot{\text{PAH}}_j] \quad (2.154)$$

The calculations of rate of inception and PAH adsorption from  $\text{PAH}_j$  requires the concentration of corresponding monomer radical that can be determined by applying the steady-state assumption for  $\dot{\text{PAH}}_j$ .

$$\frac{d[\dot{\text{PAH}}_j]}{dt} = 0$$

$$\begin{aligned} k_{f,d_j} [\text{PAH}_j] [\text{H}] - k_{r,d_j} [\dot{\text{PAH}}_j] [\text{H}_2] - k_{f,h_j} [\dot{\text{PAH}}_j] [\text{H}] - k_{inc_j} [\dot{\text{PAH}}_j]^2 \\ - \sum_{i=1}^{n_{sec}} k_{ads_j}^i [\dot{\text{PAH}}_j] [\text{Soot}]^i = 0 \end{aligned}$$

The above equations can be rearranged as a quadratic equation similar to the dimer coalescence.

$$a_{inc_j} [\dot{\text{PAH}}_j]^2 + b_{ads_j} [\dot{\text{PAH}}_j] + c_j = 0, \quad (2.155)$$

$$a_{inc_j} = k_{f,d_j} \quad (2.156)$$

$$b_{ads_j} = k_{r,d_j} [\text{H}_2] + k_{f,h_j} [\text{H}] + \sum_{i=1}^{n_{sec}} k_{ads_j}^i [\text{Soot}]^i \quad (2.157)$$

$$c_{inc_j} = k_{f,d_j} [\text{PAH}_j] [\text{H}] \quad (2.158)$$

Finally, solving the quadratic equation for each PAH results in concentration of the radical using the following equation as:

$$[\dot{\text{PAH}}_j] = \begin{cases} \frac{-b_{ads_j} + \sqrt{\Delta_j}}{2a_{inc_j}}, & \text{if } \Delta_j \geq 0 \\ 0 & \text{if } \Delta_j < 0 \end{cases} \quad (2.159)$$

$$\Delta_j = b_{ads_j}^2 - 4a_{inc_j}c_j \quad (2.160)$$

The contribution of inception and adsorption to the partial source terms for E-Bridge formation can be written as:

$$I_{N,inc} = \frac{1}{\rho} \sum_{j=1}^{n_{PAH}} 2\omega_{inc_j} n_{PAH_j,C}, \quad (2.161)$$

$$I_{C_{tot},inc} = \frac{1}{\rho} \sum_{j=1}^{n_{PAH}} 2\omega_{inc_j} n_{PAH_j,C}, \quad (2.162)$$

$$I_{H_{tot},inc} = \frac{1}{\rho} \sum_{j=1}^{n_{PAH}} 2\omega_{inc_j} (n_{PAH_j,H} - 2), \quad (2.163)$$

$$I_{C_{tot},ads}^i = \frac{1}{\rho} \sum_{i=1}^{n_{PAH}} \omega_{ads_j}^i n_{C,PAH_j}, \quad (2.164)$$

$$I_{C_{tot},ads}^i = \frac{1}{\rho} \sum_{i=1}^{n_{PAH}} \omega_{ads_j}^i (n_{H,PAH_j} - 2). \quad (2.165)$$

The rate of removal of each PAH involved in soot inception and PAH adsorption and release of H<sub>2</sub> to the gas mixture can be expressed as:

$$\left( \frac{d[PAH_j]}{dt} \right)_{inc} = -2 \sum_{k=1}^{n_{PAH}} w_{inc_j} - \sum_{i=1}^{n_{sec}} w_{ads_j}^i. \quad (2.166)$$

$$\left( \frac{d[H_2]}{dt} \right)_{inc} = \sum_{i=1}^{n_{sec}} w_{ads_j}^i. \quad (2.167)$$

## 2.7 Gas scrubbing rates

The rate of production/destruction of species involved in soot formation must be taken into account to preserve the mass and energy balance in reactive systems. In order to do that, the production rate of gaseous species calculated by Cantera must be corrected for the rate of release/consumption due to PAH growth and surface reaction models.

$$\left( \frac{d[PAH_j]}{dt} \right)_{tot} = \left( \frac{d[PAH_j]}{dt} \right)_{gas} + \left( \frac{d[PAH_j]}{dt} \right)_{inc} + \left( \frac{d[PAH_j]}{dt} \right)_{ads}. \quad (2.168)$$

H<sub>2</sub> is released to the gas mixture due to inception, PAH adsorption as well as oxidation.

$$\left( \frac{d[H_2]}{dt} \right)_{tot} = \left( \frac{d[H_2]}{dt} \right)_{gas} + \left( \frac{d[H_2]}{dt} \right)_{inc} + \left( \frac{d[H_2]}{dt} \right)_{ads} + \left( \frac{d[H_2]}{dt} \right)_{ox}. \quad (2.169)$$

Surface growth consumes C<sub>2</sub>H<sub>2</sub> and adds H<sub>2</sub> to the gas mixture.

$$\left( \frac{d[C_2H_2]}{dt} \right)_{tot} = \left( \frac{d[C_2H_2]}{dt} \right)_{gas} + \left( \frac{d[C_2H_2]}{dt} \right)_{gr}. \quad (2.170)$$

$$\left( \frac{d[H]}{dt} \right)_{tot} = \left( \frac{d[H]}{dt} \right)_{gas} + \left( \frac{d[H]}{dt} \right)_{gr}. \quad (2.171)$$

Oxidation uses O<sub>2</sub> and OH to remove carbon from soot particles and generates H<sub>2</sub> and CO.

$$\left( \frac{d[CO]}{dt} \right)_{tot} = \left( \frac{d[CO]}{dt} \right)_{gas} + \left( \frac{d[CO]}{dt} \right)_{ox}. \quad (2.172)$$

$$\left( \frac{d[O_2]}{dt} \right)_{tot} = \left( \frac{d[O_2]}{dt} \right)_{gas} + \left( \frac{d[O_2]}{dt} \right)_{ox}. \quad (2.173)$$

$$\left( \frac{d[OH]}{dt} \right)_{tot} = \left( \frac{d[OH]}{dt} \right)_{gas} + \left( \frac{d[OH]}{dt} \right)_{ox}. \quad (2.174)$$

# Chapter 3

## Results

### 3.1 Validation

A set of simulations was performed to ensure the accuracy and reliability of omnisoot for prediction of soot formation. Aerosol dynamics is validated by comparing the results of population balance models implemented in omnisoot with those of DEM simulations from literature. Carbon and hydrogen mass and energy balances are also rigorously evaluated to ensure that residuals fall within the bounds of acceptable numerical error.

#### 3.1.1 Collision Frequency

The collision frequency function determines the rate at which two particles collide, which results in the reduction of total number of agglomerates and increase in size. In the absence of strong flow shear or external forces, Brownian motion is the main driving force for particle coagulation. As explained in Sections 2.4.4.1 & 2.4.5.1, omnisoot employs harmonic mean and Fuchs interpolations to calculate collision frequency of agglomerates from free-molecular to continuum regimes based on gas mean free path, and particle morphology.

The test case for validation of collision frequency is based on the DEM simulation of 2000 monodisperse spherical particles with the density of 2200 kg/m<sup>3</sup> in a cubic cell with the constant temperature of 298 K and pressure of 1 atm [155]. Figure 3.1 depicts the collision frequency plotted against Knudsen number ( $\text{Kn} = 2\lambda/d_m$ ) obtained by omnisoot using harmonic mean (red solid line) and Fuchs interpolation (green dashed line) and DEM results of Goudeli et al. [155]. The Fuchs interpretation perfectly matches DEM data over the free-molecular ( $\text{Kn} < 10$ ) to the continuum ( $\text{Kn} > 10$ ) range. Harmonic mean is also in good agreement with the DEM results in the free-molecular and continuum regime, but slightly underpredicts the collision frequency in the transition regime ( $0.1 \leq \text{Kn} \leq 10$ ) with relative errors less than 16%.

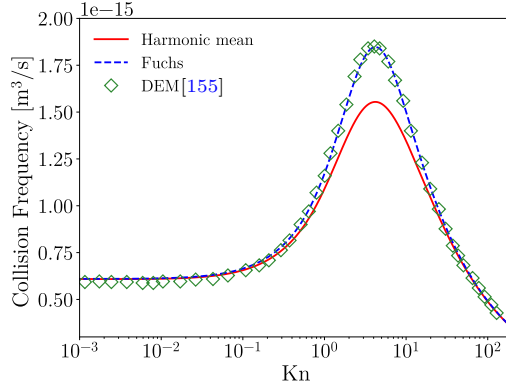


Figure 3.1: The comparison of collision frequency,  $\beta$ , obtained by omnisoot using harmonic mean (red solid line) and Fuchs interpolation (green dashed line) with DEM results (symbols) [155]

### 3.1.2 Coagulation

This test case was designed and conducted to validate the coagulation sub-unit of both particle dynamics models, MPBM and SPBM, by comparing the results of omnisoot with those of DEM [156]. The constant volume reactor was used for this test case, but it will be applicable to other reactors and flame models as long as the particle residence time matches with the values obtained by DEM. An adiabatic reactor with the volume of  $1 \text{ m}^3$  is initialized with  $2.6261 \times 10^{18}$  spherical particles 2 nm in diameter. The initial conditions are indicated in Table 3.1. The particles are allowed to coagulate in the free molecular regime and grow in size while no inception, PAH adsorption and surface growth occur. Figure 3.3 demonstrates the number density of agglomerates ( $N_{agg}$ ) and primary particles ( $N_{pri}$ ), and mobility ( $d_m$ ) and gyration ( $d_g$ ) diameters of particle obtained by omnisoot that are in good agreement with DEM results.  $N_{pri}$  is conserved during coagulation resulting in identical flat lines for both particle dynamics models, but  $N_{agg}$  declines over time with the higher decay rate for SPBM because it accounts for the polydispersity of agglomerates that results in larger collision frequency compared to MPBM. Therefore, mean mobility and gyration diameter of SPBM (red lines in Fig. 3.3-b) are slightly larger than those predicted by MPBM (blue lines of the same figure).

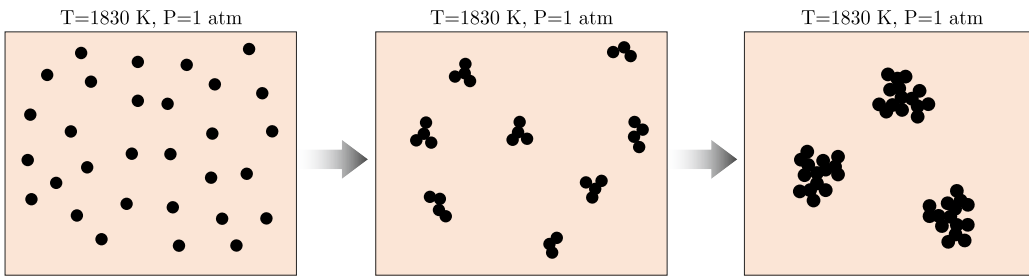


Figure 3.2: The schematic of agglomeration process in the coagulation test cases where initially spherical particle collide and form agglomerate

MPBM model cannot resolve PSD because of the monodispersity assumption. In contrast, SPBM tracks the number concentration of particles in separate sections that can be used to construct evolving PSD and calculate mean properties and determine the spread of size distribution of particles during coagulation. Figure 3.4-a shows the standard deviation of mobility diameter,  $\sigma_g$  predicted by SPBM in close agreement with DEM results.  $\sigma_g$  starts from unity indicating a monodisperse population at the beginning of simulation, and it finally reaches 2.03 that is the signature geometric standard deviation for agglomerate mobility diameters in the free molecular regime [157]. Fig. 3.4 demonstrates the evolution of non-dimensional PSD from  $t=1 \text{ ms}$  to  $677 \text{ ms}$ . The PSD is plotted for

Table 3.1: The simulations conditions of the coagulation test case [156]

Property	Value
Composition	CH <sub>4</sub> :0.425, O <sub>2</sub> :0.435, N <sub>2</sub> :0.14
T	1830 K
P	1 atm
$N_{agg}^1$	$3.514 \times 10^{-5}$ mol/kg
$N_{pri}^1$	$3.514 \times 10^{-5}$ mol/kg
$d_p^1$	2 nm

the normalized concentration,  $\Psi = \bar{v}n_{agg}(v, t)/N_{agg,inf}$  and dimensionless volume,  $\eta = v/\bar{v}$ , where  $n_{agg}(v, t)$  is the size distribution function of agglomerate,  $v$  particle volume,  $\bar{v}$  mean particle volume,  $N_{agg,inf}$  total number concentration of agglomerates. For short residence times,  $t \approx 4$  ms, the PSD resembles a half bell curve because the majority of particles have diameters close to  $d_0 = 2$  nm with the average volume close to the minimum volume, so the particles with  $\eta \approx 1$  have the largest concentration. As particles grow by coagulation, the PSD rapidly transitions to a full bell-curve ( $t \geq 22$  ms) and does not change for longer residence times,  $t \geq 447$  ms marking the attainment of SPSD in a good agreement with DEM results. This confirms the capability of SPBM implemented in omnisoot to capture SPSD for soot agglomerates as a signature of Brownian-driven particle coagulation.

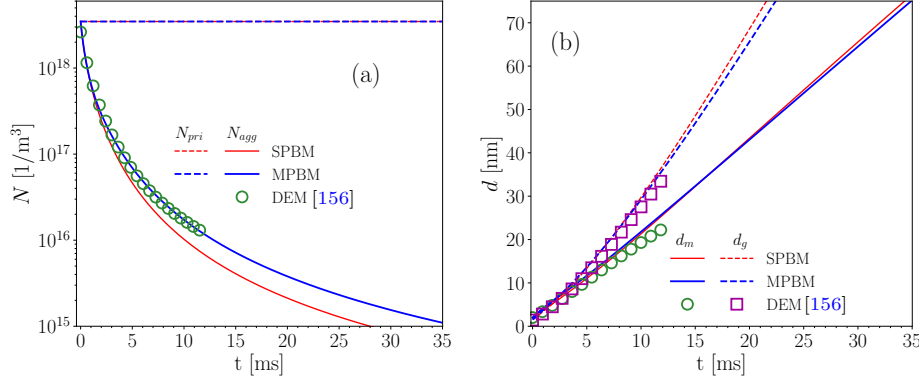


Figure 3.3: The total number concentration of agglomerates and primary particles (a), and mobility and gyration diameter (b) obtained with omnisoot using MPBM and SPBM that are in close agreement with the DEM results [156] indicating the validation of coagulation sub-model

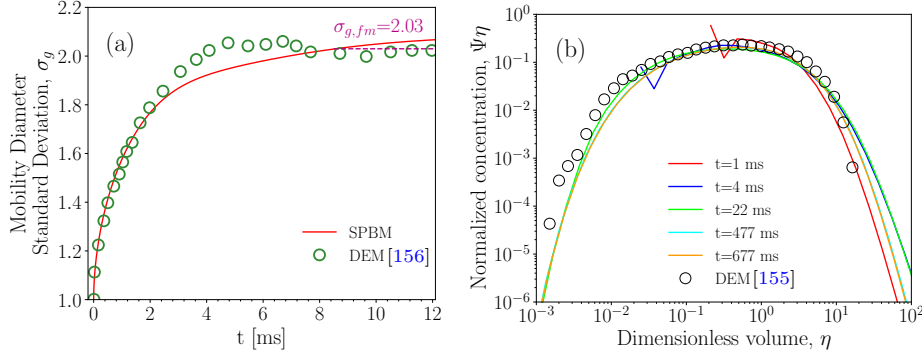


Figure 3.4: The standard deviation (residual) of mobility diameter,  $\sigma_g$  obtained with SPBM in close agreement with DEM results [156] (left pane) that reaches  $\sigma_{g,fm} = 2.03$  characteristic of the free molecular regime [157]; the particle size distribution (normalized number concentration of agglomerates is plotted against non-dimensional volume in the right pane) at different residence times that overlaps after initial transient phase marking the attainment of self-preserving size distribution in good agreement with DEM results [155]

### 3.1.3 Constant Volume Reactor

The pyrolysis of 30% CH<sub>4</sub> diluted in N<sub>2</sub> with the initial temperature and pressure of 2455 K and 3.47 atm, respectively, was simulated using the constant volume reactor model with the residence time of 40 ms. The combination of available PAH growth and particle dynamics models leads to eight different cases that were simulated to ensure the conservation of mass and energy. Here, we focus on the total elemental balance of carbon and hydrogen because they are involved in soot processes. Figure 3.5 demonstrates the relative error of total carbon, hydrogen and energy of system for different PAH growth and particle dynamics models in the constant volume that falls below 10<sup>-10</sup> for all parameters confirming the validity of model in satisfying the mass and energy balance in the constant volume reactor using all models.

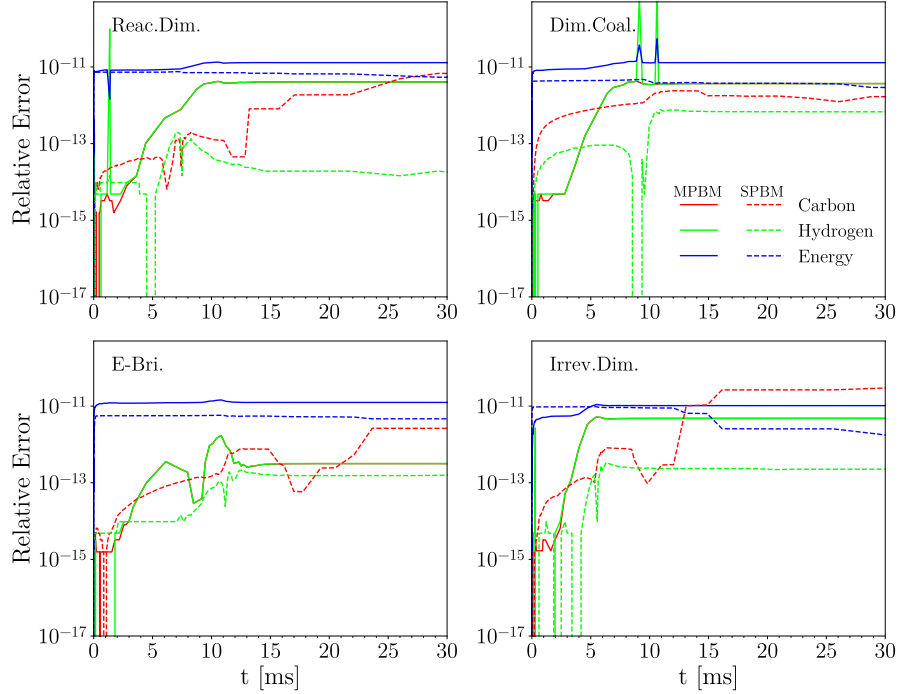


Figure 3.5: The relative error (residual) of total carbon (red line) and hydrogen (green line) mass, and total internal energy residual of gas and soot (blue line) plotted against residence time during pyrolysis of 30%  $\text{CH}_4\text{-N}_2$  at 2455 K and 3.47 atm in the constant volume reactor simulated using different PAH growth models along with MPBM (solid line) and SPBM (dashed line)

### 3.1.4 Plug Flow Reactor

Methane pyrolysis in an adiabatic flow reactor is used to check elemental carbon and hydrogen, and energy balance in the PFR model. The inlet flow enters the reactor at the composition of 30%  $\text{CH}_4$  diluted in  $\text{N}_2$ , and  $T=2100$  K and  $P=1$  atm. Figure 3.6 shows the residual of total elemental carbon and hydrogen, and energy up to 40 cm of the reactor length using all PAH growth and particle dynamics model. The residuals are in the order of  $10^{-11}$  and start to grow at the beginning of the reactor by pyrolysis of  $\text{CH}_4$  and the formation of intermediate species such as  $\text{C}_2\text{H}_2$  and PAHs. This initiates soot inception and surface growth affecting the gas chemistry and energy that ends near  $x=10$  cm, and then the coagulation of particles is dominant with no affect on mass and energy of particles. As a result, PFR model of omnisoot satisfied the conservation of the mass and energy.

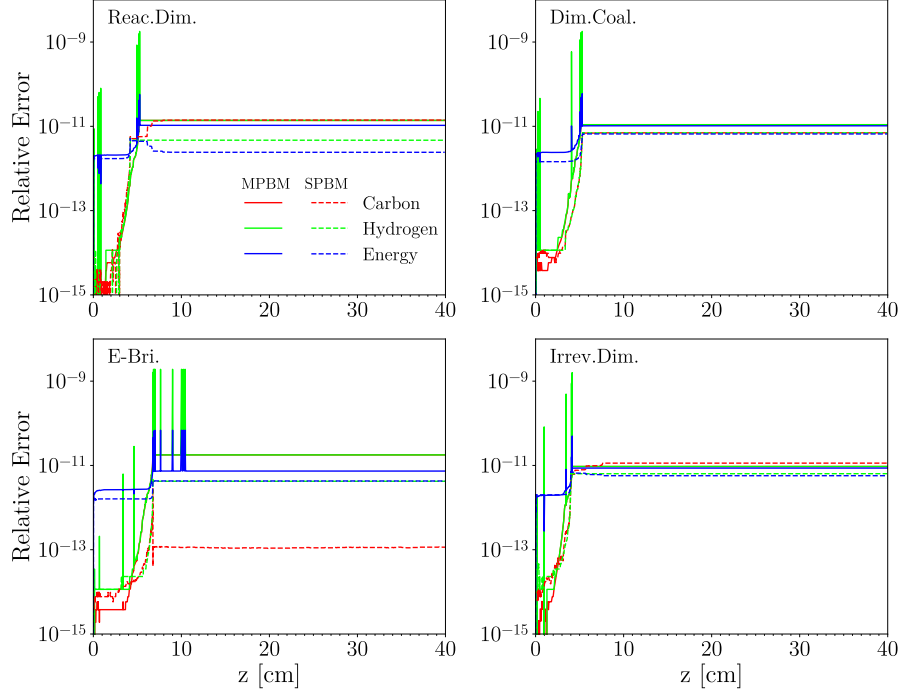


Figure 3.6: The relative error (residual) of total carbon (red line) and hydrogen (green line) mass, and total internal energy residual of gas and soot (blue line) plotted against reactor length (cm) in the adiabatic flow reactor during pyrolysis of 30%  $\text{CH}_4\text{-N}_2$  at 2100 K and 1 atm simulated using different PAH growth models and MPBM (solid line) and SPBM (dashed line)

## 3.2 Soot yield and morphology during methane pyrolysis in shock-tubes

In this section, we focus on simulation of soot formation in shock-tubes using the constant volume reactor of omnisoot in order to (i) assess the performance of reaction mechanisms in prediction of the species mole fraction measured by laser diagnostics, and (ii) evaluate the accuracy of inception models to predict soot yield and morphology.

Temperature ranges achieved in shock-tube experiments ( $T > 2000$  K) are relevant for plasma pyrolysis of methane ( $\text{CH}_4$ ) as an emerging alternative production method for co-generation of CB and hydrogen [158]. Achieving specific grades of CB for different target applications requires a good control over its properties such as its morphology (quantified by primary particle,  $d_p$  and mobility diameter,  $d_m$ ), composition (elemental carbon to hydrogen ratio), specific surface area (inversely proportional to  $d_p$ ,  $\text{SSA} = 6/(\rho_{soot} d_p)$ ) and internal nanostructure (composed of aligned graphitic shell and disordered core). However, this is challenging because of the complexity of soot inception and mass growth processes and its coupling with gas phase chemistry, dependence on local temperature and pressure, and short time scales of soot inception and surface growth [36]. Therefore, robust particle dynamics models coupled with detailed chemical mechanisms are essential to better understand methane-to-CB conversion process under different feedstock compositions, and temperature and pressure time-histories.

While methane combustion has been extensively studied [159] due to the need for a detailed chemical description of natural gas combustion, the formation of carbonaceous particles such as soot and CB from methane pyrolysis are not well understood yet. Significant differences exist between reaction mechanisms in prediction of  $\text{CH}_4$  and intermediate species such as  $\text{C}_2\text{H}_2$ , and  $\text{C}_2\text{H}_4$  in flame and reactors [159]. These uncertainties are amplified for larger hydrocarbons, especially polycyclic

aromatic hydrocarbons (PAH) due to multiplicity of pathways that are not identified in available reaction mechanisms.

Shock tubes can be effective for kinetic studies and measurements of methane pyrolysis and the subsequent soot inception and surface growth due to the uniform and instant heating of the mixture behind the reflected shock to the desired temperature and pressure as well as the absence of complicating factors such as diffusion and mixing. The shock-wave propagation and reflection creates nearly isothermal and isobaric conditions ideal for kinetic studies of pyrolysis and particle formation. However, these conditions are limited to short residence times usually 1-3 ms, so they can only be used to study early stages of soot formation such as inception and surface growth, and not for processes occurring at longer residence times such as coagulation, graphitization and carbonization.

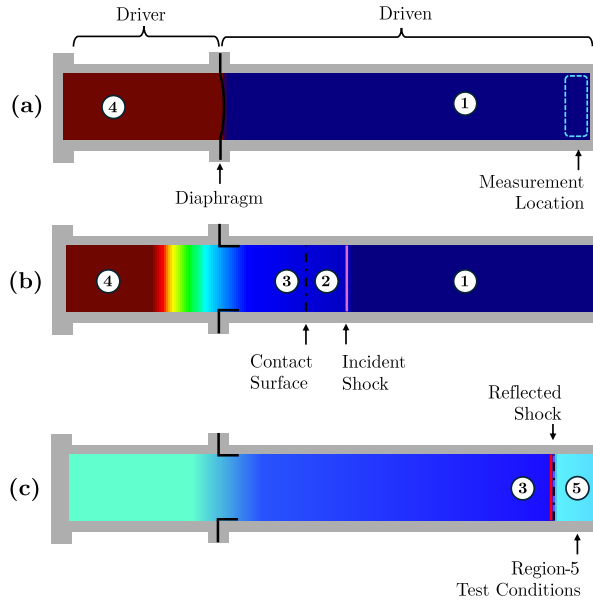


Figure 3.7: Different stages of shock wave propagation during shock-tube test from (a) before rupture of diaphragm leading to (b) propagation of incident shock towards the end of shock-tube and (c) its reflection from the end wall that increases pressure and temperature of test gas (Reprinted from Ref. [160])

Different stages of shock-wave propagation is illustrated in Fig.3.7. A shock tube consists of a driver and a driven section separated by a single-use diaphragm. The driver section contains usually an inert gas with a low molecular weight such as He, and the driven section is filled with the studied test gas. The driver section is pressurized to the desired pressure until the rupture of the diaphragm. This creates a shock wave that propagates through the driven section causing a pressure and temperature jump in the test gas.

After reaching the end wall, the shock wave reflects back towards the driver end of the shock-tube resulting in a secondary compression and heating of the mixture, and ultimately stagnating the test gas. In nearly 10  $\mu\text{s}$ , this shock-heating process can bring the test gas from room-temperature to temperatures upwards of 10,000 K, and pressures more than 1000 atm.

The passage of reflected shock, referred to as region 5 with  $T_5$  and  $P_5$ , is the reference for calculation of residence time and the starting point for simulations. The delay in appearance of soot (often quantified by a threshold for LII or extinction signals) is known as induction time,  $\tau_{\text{ind}}$ . There has been a lot of research in the literature on induction time (similarly on ignition delay time) in shock tubes [161], but it is not the focus of this work. Instead, we mainly focus on species concentrations and soot characteristics during the pyrolysis of methane, at atmospheric and higher pressures which can be used for the design and optimization of CB in plasma reactors [158].

### 3.2.1 Experimental setup and data collection

The experiments on CH<sub>4</sub> pyrolysis were conducted by Hanson Research Group at Stanford University. The data has not been published yet (at the time of writing the document) and were provided through the collaboration with Monolith Materials and Stanford University.

Mole fraction time histories of methane (CH<sub>4</sub>), acetylene (C<sub>2</sub>H<sub>2</sub>), and ethylene (C<sub>2</sub>H<sub>4</sub>) were captured using continuous wave (CW) laser absorption at 3.365 μm, 2.998 μm, and 10.532 μm, respectively [162, 163, 164]. Soot volume fraction was measured using laser light extinction at  $\lambda=633$  nm and 1064 nm with absorption function, E(m) of 0.174 and 0.203 [165], respectively. Additionally, soot samples were collected onto imaging stubs mounted in the shock-tube end-wall. A schematic of the experimental setup for laser diagnostics in the shock tube is shown in Fig. 3.8. Samples were extracted from the interior surface of the shock tube endwall after each experiment to allow for imaging and analysis of the particulates. TEM images were recorded with a FEI Tecnai G2 F20 X-TWIN microscope and Gatan SC200 camera for the test case of P<sub>5</sub>=4.5 atm and T<sub>5</sub>=2217 K.

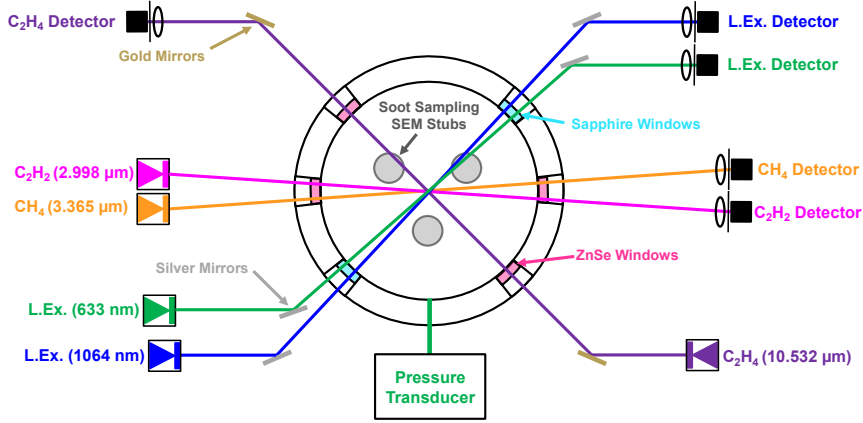


Figure 3.8: Layout of the laser diagnostics and shock-tube setup. Spatial and spectral filtering is employed to ensure high-quality absorbance measurements to infer species mole fractions and soot volume fraction. Soot samples are collected at the shock-tube endwall. All lasers are aligned in a plane 1 cm from the endwall

### 3.2.2 30% Methane Data-set

The first data set includes eight data points with the fuel loading of 30% CH<sub>4</sub>-Ar at P=4±0.5 atm in the temperature range of 1800-2500 K. Table 3.2 lists the test conditions including pressure, temperature and composition of all data points.

Table 3.2: The pressure, temperature and composition of simulation data points for 30% CH<sub>4</sub>

	Datapoints							
	(1)	(2)	(3)	(4)	(5)	(6)	(7)	(8)
T [K]	1861	1917	2030	2155	2184	2313	2375	2455
P [atm]	4.12	3.74	3.56	3.93	3.62	3.58	3.75	3.47
Composition	CH <sub>4</sub> : 0.3, Ar: 0.7							

The time history of CH<sub>4</sub>, C<sub>2</sub>H<sub>4</sub> and C<sub>2</sub>H<sub>2</sub> mole fraction as well as soot yield and volume fraction were reported up to 0.5 ms. The constant volume reactor of omnisoot was used with all PAH growth and particle dynamics models. The performance of reaction mechanisms are assessed by

comparing the mole fraction of species captured by laser diagnostics, CH<sub>4</sub>, C<sub>2</sub>H<sub>4</sub>, and C<sub>2</sub>H<sub>2</sub> with model predictions using Caltech [166], KAUST [159] and ABF [58] mechanisms. The analysis of simulation results (see Figs. B.2-B.2) showed that soot formation described by different PAH growth and particle dynamics models have negligible impact on prediction the mole fraction of measured species in the studied temperature range. Therefore, the assessment of reaction mechanisms for prediction of major species is performed without soot to simplify the analysis. Figs. 3.9-3.11 compares the mole fraction of CH<sub>4</sub>, C<sub>2</sub>H<sub>4</sub>, C<sub>2</sub>H<sub>2</sub> predicted by Caltech, KAUST, and ABF with data from laser diagnostics. Note that only a subset of simulations are shown for brevity, and results for the whole temperature range can be found in Figs. B.8-B.10. CH<sub>4</sub> mole fraction starts with a sharp drop from 0.3 at the beginning (corresponding to fast decomposition of methane) followed by a more gradual decrease. The initial decomposition rate increases with temperature. All mechanisms underpredict CH<sub>4</sub> mole fraction, but ABF mechanism predictions are closer to the measurements than KAUST and Caltech. In other words, KAUST and Caltech overestimate CH<sub>4</sub> conversion rate. The mole fraction of C<sub>2</sub>H<sub>4</sub> (Fig.3.10) starts with a quick jump after methane decomposition, reaches the maximum value and gradually decreases towards its final value. The simulations extended beyond test time of shock-tube calculations showed that C<sub>2</sub>H<sub>4</sub> mole fraction predicted by KAUST and Caltech mechanisms continues to decrease to the equilibrium values, but ABF predicts an increase at longer residence times indicating reversal of C<sub>2</sub>H<sub>4</sub> decomposition which is more pronounced at high temperatures. The C<sub>2</sub>H<sub>2</sub> mole fraction increases in two steps, a rapid increase at the beginning followed by a gradual one. ABF mechanism predictions are in good agreement with measurements, but Caltech and KAUST underpredict the C<sub>2</sub>H<sub>2</sub> mole fraction. The difference between mechanisms are more pronounced at equilibrium conditions. While ABF predicts a plateau beyond 1.5 ms, KAUST and Caltech predict a decrease towards a lower value indicating conversion of acetylene to larger hydrocarbons and PAHs. The carbon mass fraction (CMF) of measured species, CH<sub>4</sub>, C<sub>2</sub>H<sub>4</sub> and C<sub>2</sub>H<sub>2</sub> combined is shown in Fig. 3.12. The CMF of different mechanisms decreases up to a certain time that shortens with temperature. Beyond that, ABF mechanism predicts an increasing trend indicating that carbon returns to major species, but KAUST and Caltech continuously transfer carbon from measured species to larger hydrocarbons. This is consistent with the CMF of soot precursors shown in Fig. 3.13, which is significantly larger for KAUST and Caltech compared with ABF by two to three orders of magnitude, so it is expected that ABF mechanism cannot provide enough precursors for soot model to predict volume fraction comparable with the measurements.

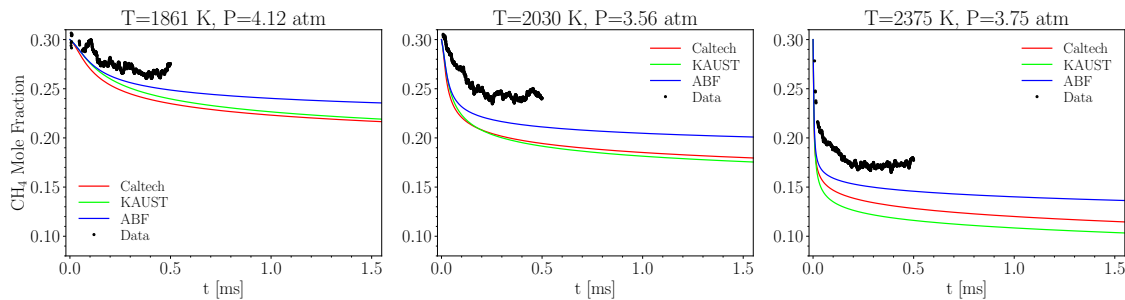


Figure 3.9: The time history of carbon mass fraction of CH<sub>4</sub> of 30% CH<sub>4</sub> pyrolysis at T=1861, 2083, and 2375 K using Caltech, KAUST, and ABF mechanisms compared with laser diagnostics data

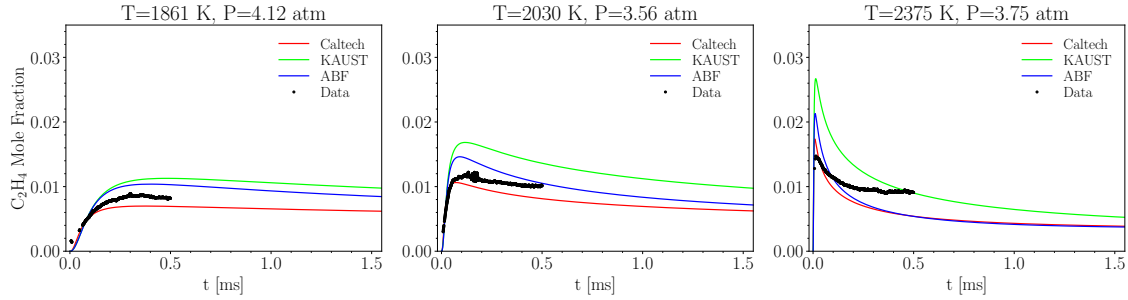


Figure 3.10: The time history of carbon mass fraction of C<sub>2</sub>H<sub>4</sub> of 30% CH<sub>4</sub> pyrolysis at T=1861, 2083, and 2375 K using Caltech, KAUST, and ABF mechanisms compared with laser diagnostics data

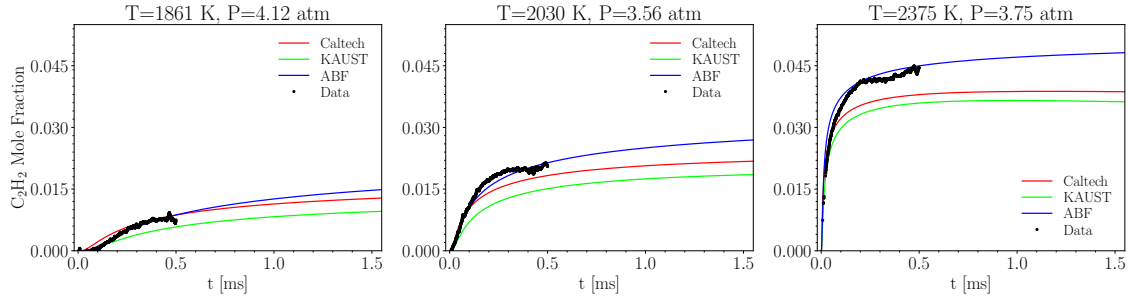


Figure 3.11: The time history of carbon mass fraction of C<sub>2</sub>H<sub>2</sub> of 30% CH<sub>4</sub> pyrolysis at T=1861, 2083, and 2375 K using Caltech, KAUST, and ABF mechanisms compared with laser diagnostics data

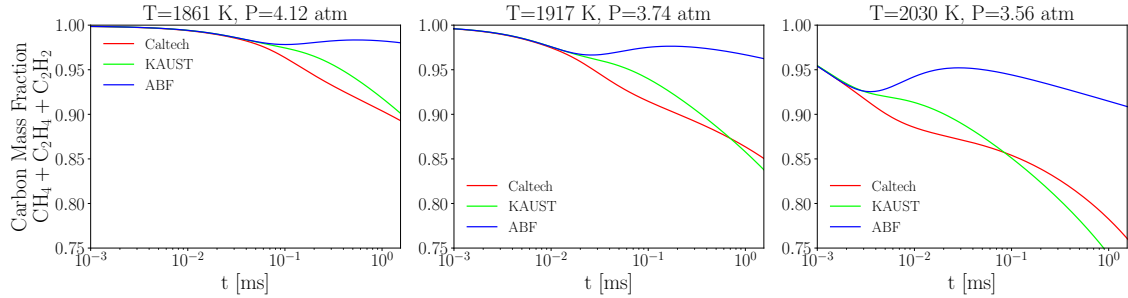


Figure 3.12: The time history of carbon mass fraction of CH<sub>4</sub>, C<sub>2</sub>H<sub>4</sub>, C<sub>2</sub>H<sub>2</sub> of 30% CH<sub>4</sub> pyrolysis at T=1861, 2083, and 2375 K using Caltech, KAUST, and ABF

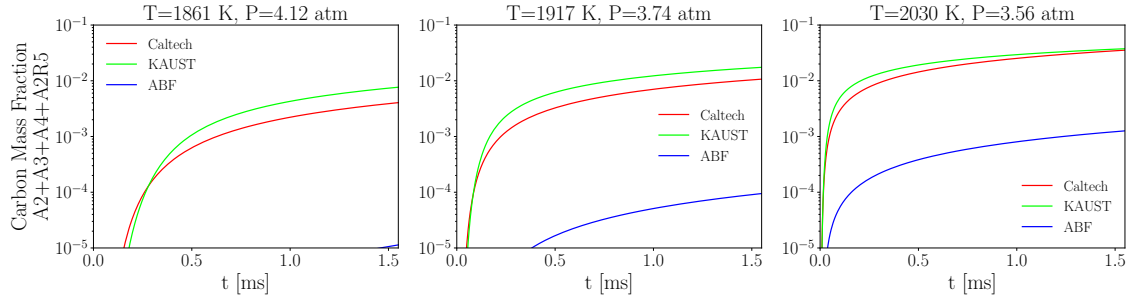


Figure 3.13: The time history of carbon mass fraction of soot precursors, A2, A3, A4 and A2R5 of 30%  $\text{CH}_4$  pyrolysis at  $T=1861$ , 2083, and 2375 K using Caltech, KAUST, and ABF mechanisms

Comparing  $f_v$  predicted by three reaction mechanisms at  $T=2375$  K and  $P=3.75$  atm with the data from extinction measurements confirms the above-mentioned conclusion. As shown in Fig. 3.14, the  $f_v$  by ABF follows a similar trend as data, but the values are nearly two orders of magnitude lower indicating small PAH concentrations. Although both Caltech and KAUST predict  $f_v$  comparable with data, KAUST will be used for detailed soot simulations as its combination with E-Bridge Modified accurately captures soot volume fraction. Having said that, any conclusions drawn using KAUST can be easily generalized to Caltech as well.

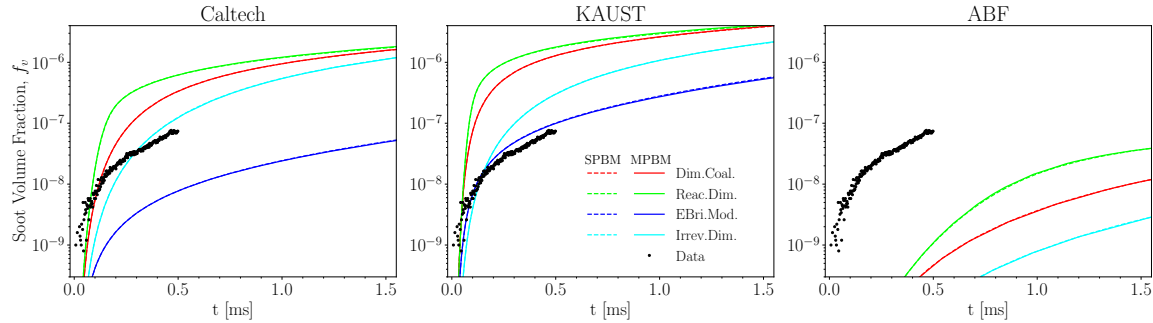


Figure 3.14: The time history of soot volume fraction of 30%  $\text{CH}_4$  pyrolysis at  $T=2375$  K and  $P=3.75$  atm using Caltech, KAUST, and ABF mechanism and different PAH growth and particle dynamics models

Fig. 3.15 shows that the time variation of soot volume fraction in  $T=2155$ , 2313, and 2455 K. The measurement data was not available (or too noisy) below 2155 K due to lack of enough soot particles leading to weak extinction signals (see Fig. B.13). SPBM and MPBM results coincide indicating that taking polydispersity into account by the particle dynamics model does not affect soot mass during 1.5 ms of simulation.  $f_v$  by EBridge Modified is in good agreement with data and the lowest among inception models across the temperature range. On the other hand, Reactive Dimerization and Dimer Coalescence yields the largest  $f_v$  nearly two orders of magnitude larger than data (and EBridge Modified). There is a remarkable similarity between trend of  $f_v$  and CMF of soot precursors (Fig. 3.13) that highlights the major role of inception and PAH adsorption in soot mass growth. Temperature promotes soot formation in the studied shock tube. Fig. 3.16 depicts that  $f_v$  computed at 1.5 ms increases with temperature in a nearly linear fashion expect for EBridge Modified.

Fig. 3.17 shows the time history of primary particle diameter,  $d_p$  at different temperatures. For Sectional model,  $d_p$  is the average primary particle diameter calculated from arithmetic mean of  $d_p$  of all sections. As expected, EBridge Formation and Irreversible Dimerization predict the lowest  $d_p$  due to low soot mass growth rate leading to small  $f_v$  values. Dimer Coalescence and Reactive Dimerization generate a relatively close  $f_v$  values (corresponding to similar soot mass growth),

but Reactive Dimerization predicts a larger  $d_p$  indicating lower inception flux and stronger PAH adsorption rate of this model compared to Dimer Coalescence. There is a noticeable difference between sectional and monodisperse models in the  $d_p$  predicted by Reactive Dimerization, but other inception models do not exhibit such a sensitivity to particle dynamics model. Both models predict the initial rapid rise in  $d_p$ . While MPBM predicts a gradual increase to final value,  $d_p$  by SPBM decreases after the initial rise due to stronger inception rate by SPBM that generates particle with  $d_p=2$  nm bringing down the average  $d_p$ . Fig. 3.18 depicts temperature dependence of  $d_p$  at 1.5 ms where SPBM predicts a decreasing trend as opposed to MPBM.

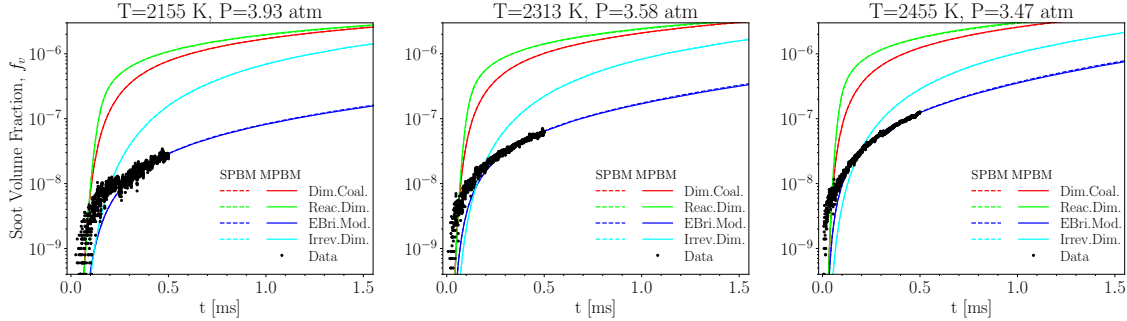


Figure 3.15: The time history soot volume fraction,  $f_v$  of 30% CH<sub>4</sub> pyrolysis for T=2155, 2313, and 2455 K using KAUST with different combinations of PAH growth and particle dynamics models compared with extinction measurements

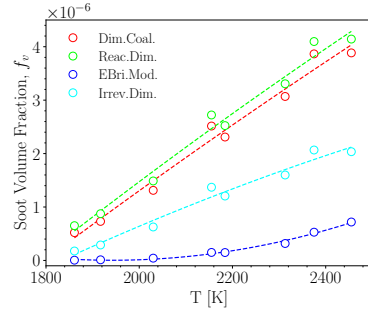


Figure 3.16: The soot volume fraction,  $f_v$  at 1.5 ms increasing with temperature during 30% CH<sub>4</sub> pyrolysis using KAUST and SPBM. The dashed lines are added to guide the eye

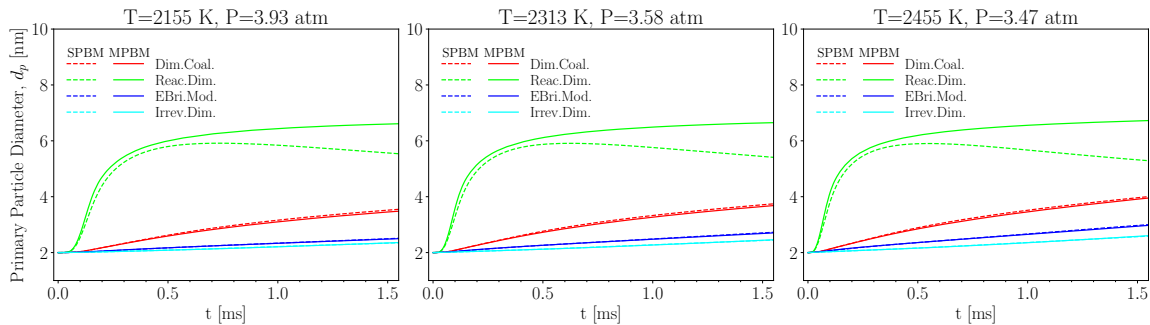


Figure 3.17: The time history of primary particle diameter,  $d_p$  of 30% CH<sub>4</sub> pyrolysis for T=2155, 2313, and 2455 K using KAUST with different combinations of PAH growth and particle dynamics models

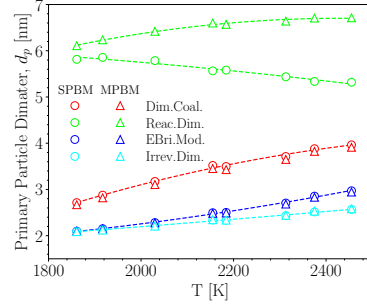


Figure 3.18: The primary particle diameter,  $d_p$  at 1.5 ms increasing with temperature during 30%  $\text{CH}_4$  pyrolysis using KAUST with MPBM and SPBM. The dashed lines are added to guide the eye

As shown in Fig. 3.19, the inception flux of Reactive Dimerization starts with a quick rise followed by a quick drop until  $t \approx 0.25$  ms which is nearly the same for both particle dynamics models, but beyond that SPBM predicts an increasing inception flux. This stems from a lower PAH adsorption rate by SPBM (with Reactive Dimerization) directing more PAHs to inception. All models predict an initial rapid rise due to PAH production by  $\text{CH}_4$  decomposition. Dimer Coalescence reaches the highest peak and continuously decreases afterward because of consumption of PAHs. However, Irreversible Dimerization and EBridge Modified nearly stay constant towards the end of simulation time.

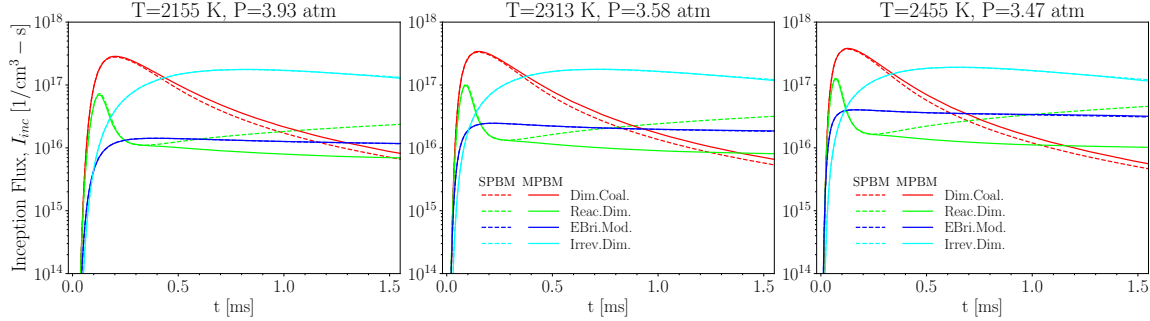


Figure 3.19: The time history of inception flux,  $I_{inc}$  of 30%  $\text{CH}_4$  pyrolysis for  $T=2155$ , 2313, and 2455 K using KAUST with different combinations of PAH growth and particle dynamics models

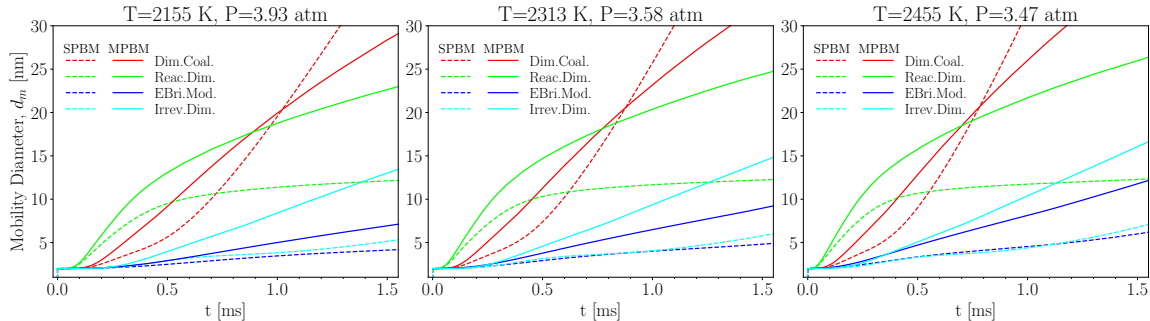


Figure 3.20: The time history of mobility diameter,  $d_m$  of 30%  $\text{CH}_4$  pyrolysis for  $T=2155$ , 2313, and 2455 K using KAUST with different combinations of PAH growth and particle dynamics models

As shown Fig. 3.20,  $d_m$  exhibits a stronger sensitivity to the employed particle dynamics model compared to  $d_p$  because MPBM cannot capture the initial transition of particle population before the

Table 3.3: The pressure, temperature and composition of simulation data points for 10% CH<sub>4</sub>

	Datapoints									
	(1)	(2)	(3)	(4)	(5)	(6)	(7)	(8)	(9)	(10)
T [K]	1873	1927	2074	2030	2348	1776	1897	2085	2277	2406
P [atm]	1.09	1.37	1.27	1.22	1.13	4.76	4.49	4.85	4.43	3.89
Composition	CH <sub>4</sub> : 0.1, CO <sub>2</sub> : 0.01, Ar: 0.7									

attainment of self-preserving size distribution. As a result, morphology (quantified by characteristic diameters) predicted by MPBM diverges from the SPBM results that are closer to actual polydisperse morphology of soot. Overall, Dimer Coalescence predicts a larger mean mobility diameter because of stronger inception flux at the beginning of simulation time (see Fig. 3.19) leading to more primary particles and higher coagulation rate that generates larger agglomerates. Fig. 3.21 shows the carbon addition rate by PAH adsorption is comparable and greater than that of HACA. This difference is more pronounced for Reactive Dimerization where PAH adsorption is larger by more than one order of magnitude.

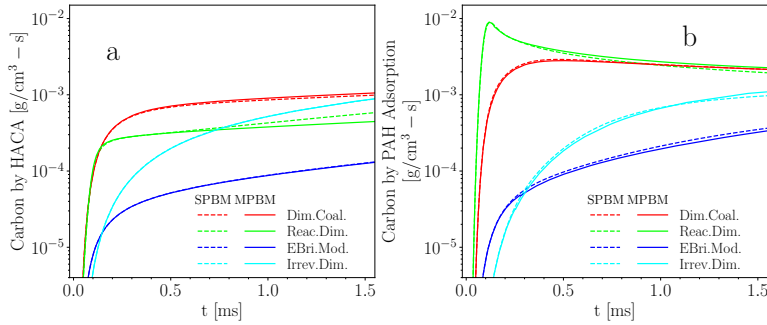


Figure 3.21: The time history of rate of carbon mass addition by (a) HACA and (b) PAH adsorption at T=2313 K using KAUSTR with different combinations of PAH growth and particle dynamics models

### 3.2.3 10% Methane Data-set

The second data set from Stanford's group includes the measurements on 10% CH<sub>4</sub> pyrolysis at P=1±0.5 atm and 4±0.5 atm in the temperature range of 1800-2500 K. The first step is the examination of chemistry by comparing the predicted species mole fraction using different reaction mechanisms with data from laser diagnostics. Then, we look into soot volume fraction and morphology for a single data point at which TEM measurements were conducted, analyze the collected TEM images, identify main factors contributing to the discrepancies in volume fraction and morphology, optimize the PAH growth models to minimize the prediction error, and apply optimized model to the rest of data points. We limit our discussion to the 4-atm cases as extinction measurements showed negligible soot in 1-atm cases. The results of whole pressure and temperature ranges can be found in Section B.1.2.

#### 3.2.3.1 Reaction Mechanism Assessment

As shown in Fig. 3.22, similar to 30% dataset, KAUSTR yields the highest CH<sub>4</sub> conversion followed by Caltech and ABF mechanism. While KAUSTR accurately predicts CH<sub>4</sub> mole fraction over the studied temperature range, Caltech and ABF overpredict it indicating that less carbon is directed toward intermediates and larger hydrocarbons.

Fig. 3.23 shows that ABF predicts the initial jump and gradual decrease towards equilibrium  $\text{C}_2\text{H}_4$  mole fraction at  $T=1897$  K in good agreement with the data, but underpredicts it at higher temperatures. KAUST mechanism overpredicts  $\text{C}_2\text{H}_4$  production at the beginning leading to higher peak as well as its later consumption resulting in lower mole fraction towards the end of simulation compared to the measurements. Fig. 3.24 depicts underprediction of  $\text{C}_2\text{H}_2$  mole fraction by all mechanisms over the whole temperature range, which is more pronounced for KAUST mechanism. Fig. 3.25 shows that carbon mass fraction in measured species decreases for all mechanisms showing conversion of carbon from major species to larger hydrocarbons, but similar to 30% simulation, ABF predicts an increase in total carbon mass fraction. As shown in Fig. 3.26, the carbon mass fraction of designated soot precursors predicted by ABF are lower by more than one order of magnitude compared to KAUST and Caltech.

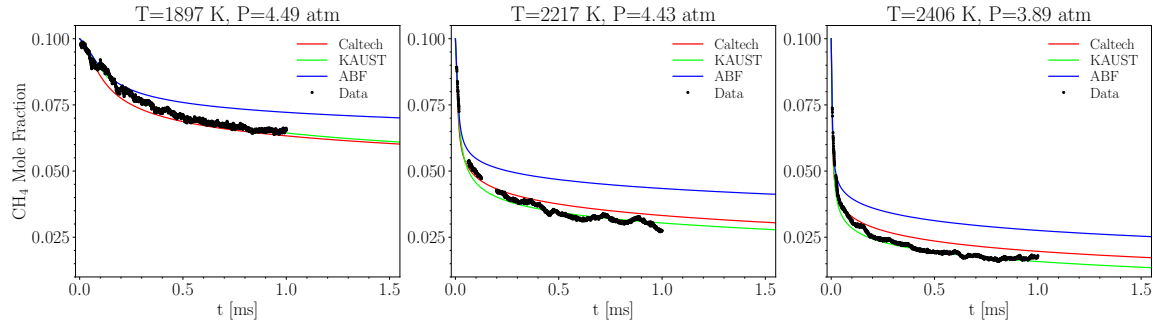


Figure 3.22: The time history of mole fraction of  $\text{CH}_4$  of 10%  $\text{CH}_4$  pyrolysis at  $T=1897$ , 2217, and 2406 K using Caltech, KAUST, and ABF mechanisms compared with laser diagnostics data

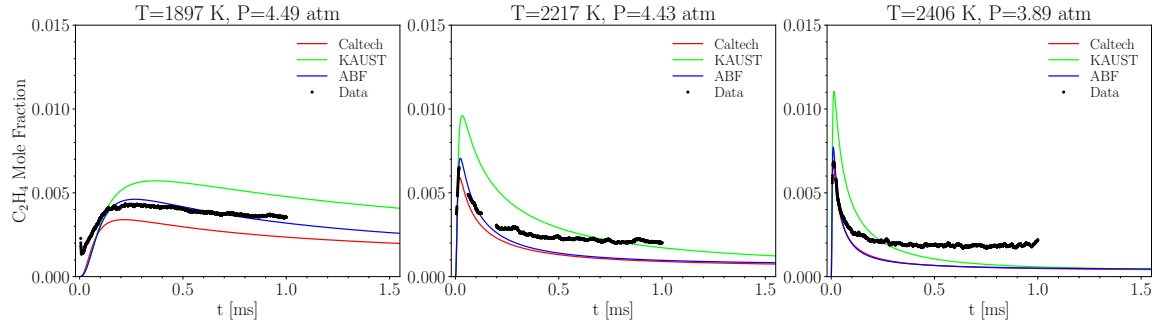


Figure 3.23: The time history of mole fraction of  $\text{C}_2\text{H}_4$  of 10%  $\text{CH}_4$  pyrolysis at  $T=1897$ , 2217, and 2406 K using Caltech, KAUST, and ABF mechanisms compared with laser diagnostics data

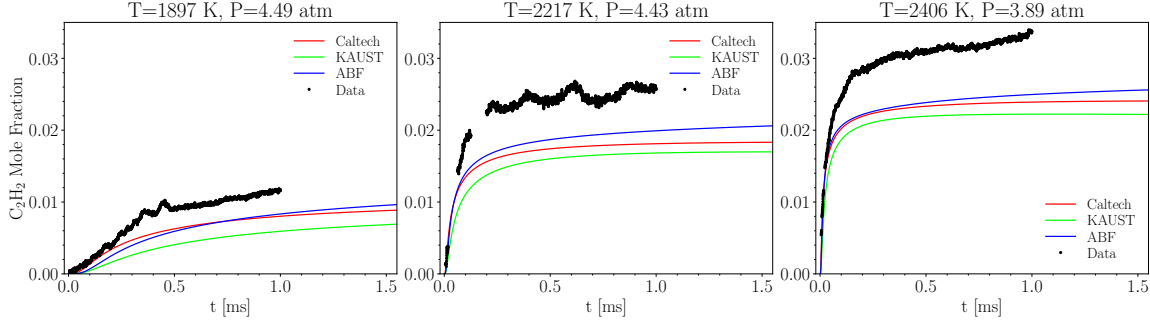


Figure 3.24: The time history of mole fraction of C<sub>2</sub>H<sub>2</sub> of 10% CH<sub>4</sub> pyrolysis at T=1897, 2217, and 2406 K using Caltech, KAUST, and ABF mechanisms compared with laser diagnostics data

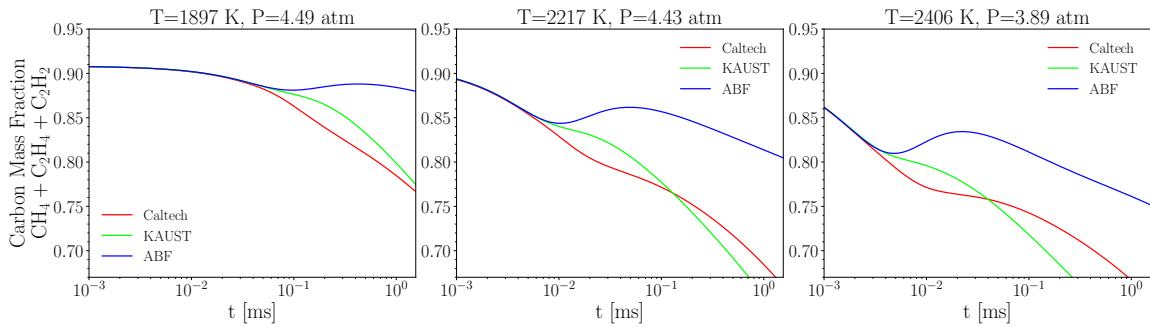


Figure 3.25: The time history of carbon mass fraction of CH<sub>4</sub>, C<sub>2</sub>H<sub>4</sub>, C<sub>2</sub>H<sub>2</sub> of 10% CH<sub>4</sub> pyrolysis at T=1897, 2217, and 2406 K using Caltech, KAUST, and ABF mechanisms compared with laser diagnostics data

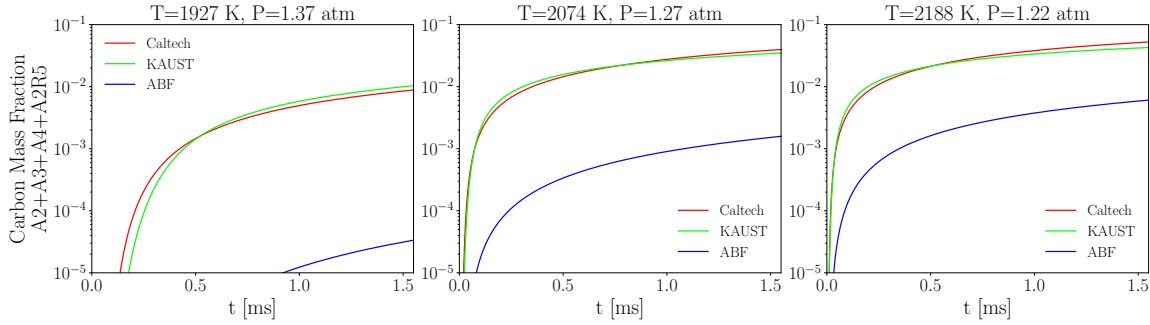


Figure 3.26: The time history of carbon mass fraction of A<sub>2</sub>, A<sub>3</sub>, A<sub>4</sub>, A<sub>2</sub>R<sub>5</sub> of 10% CH<sub>4</sub> pyrolysis at T=1897, 2217, and 2406 K using Caltech, KAUST, and ABF mechanisms compared with laser diagnostics data

### 3.2.3.2 Characterization of soot morphology in methane pyrolysis shock-tube

The TEM images of soot made during pyrolysis of 10% CH<sub>4</sub> was provided by Stanford group for a single data point of T=2217 K and P=4.5 atm that can be used to characterize soot morphology from  $d_p$  and  $d_m$ . The images in addition to soot volume fraction enables assessing the performance of omnisoott in the description of soot generated during methane pyrolysis in the shock-tube. As reported by Stanford team, the expansion wave traverses the shock tube around 2 ms reducing the temperature to nearly 1000 K freezing the chemical reactions that contribute to the surface growth,

but the coagulation continues until the collection of particles leading to larger agglomerates. As a result,  $d_p$  estimated from the TEM images closely represents  $d_p$  of agglomerates at the end of process, but  $d_m$  estimated from TEM images could be larger than the actual values due to post-expansion-wave growth of particles. *atems* package [167] was used for characterizing soot aggregates recorded in TEM images with different methods for evaluating the aggregate projected area, perimeter, and primary particle diameter. It creates a binary map from the raw TEM image where white and black pixels represent the agglomerates and background, respectively, and feeds the map to an agglomerate segmentation algorithm to detect individual agglomerates. Fig.3.27 shows a sample from TEM images and segmented agglomerates from the generated map.

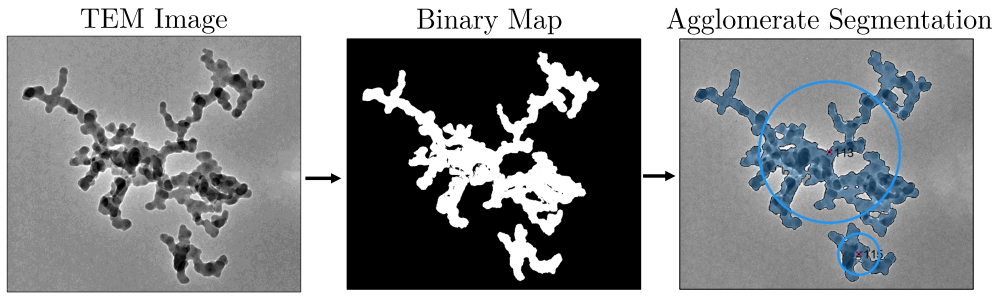


Figure 3.27: A TEM image provided by Stanford group (left pane) with the generated binary map (middle pane) and detected agglomerates using the segmentation algorithm (right pane)

We applied K-means clustering (KMC) [167] and otsu thresholding [168] to the same TEM images and compared the segmented agglomerates. A sample is shown in Fig.3.28 where KMC detected more agglomerates in the TEM image, but segments part of the background as agglomerates or divides a single agglomerate into multiple ones. On the other hand, otsu thresholding misses most of agglomerates in the sampled TEM image. Here, the K-means clustering [167] is used and 171 agglomerates were detected.  $d_m$  was calculated from the diameter of equivalent projected area ,  $A_a$  of each agglomerate. The pair correlation method (PCM) [168] was applied to compute the projected primary particle area,  $A_p$  and the mean  $d_p$  assuming that primary particle are almost uniform in size within each agglomerate. The arithmetic mean of  $d_p$  of the entire samples is calculated as

$$\bar{d}_p = \frac{\sum_{Aggs} n_p d_p}{\sum_{Aggs} n_p} \quad (3.1)$$

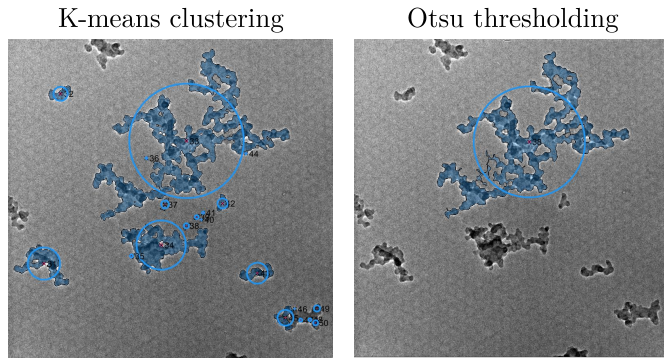


Figure 3.28: Agglomerates in single TEM image segmented by K-means clustering (left pane) and otsu thresholding (right pane)

Table 3.28 reports the arithmetic mean and median of mobility and primary particle diameter detected by atoms from TEM images. The computed  $d_m$  and  $d_p$  will be compared with soot sampled

Table 3.4: The morphological characteristics of agglomerates quantified by *atems* using KMC and PCM

Property	Arithmetic mean	Median
$d_m$ [nm]	97	69
$d_p$ [nm]	22	18

from various sources. Soot morphology is mainly governed by coagulation leading to self-similar structures in which  $d_m$  scales with  $d_p$  and  $n_p$ . Olfert and Rogak [169] analyzed soot particles from flares [170], inverted burners [171], compression ignition engines [172] and other sources to support the external mixing hypothesis and related agglomerate size characterized by  $d_m$  to  $d_p$  using the following power-law:

$$d_p = d_{p,100} \left( \frac{d_m}{100\text{nm}} \right)^{D_{\text{TEM}}}, \quad (3.2)$$

where  $d_{p,100}$  is the average primary particle diameter for an agglomerate with  $d_m = 100$  nm, and  $D_{\text{TEM}}$  is the exponent. Both quantities were obtained by fitting Eq. (3.2) to soot sampled from different sources. Fig 3.29 demonstrates the scatter plot of  $d_p$  against  $d_m$  compared with power-law curves of Eq. (3.2) using two sets of prefactor and exponent values, i)  $D_{\text{TEM}}=0.32$ ,  $d_{p,100}=20.6$  nm, and ii)  $D_{\text{TEM}}=0.39$ ,  $d_{p,100}=20.2$  nm taken from average values reported in summary of fit parameters in Table 1 of Olfert and Rogak [169]. The power-law shows a good agreement with quantities that  $d_p$  and  $d_m$  computed by *atems* can be good representative of soot agglomerates with minimal agglomerate overlap.

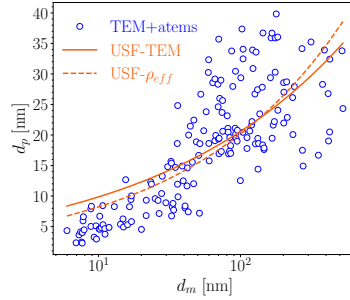


Figure 3.29: The  $d_m$  as a function of  $d_p$  from TEM image obtained by *atems* [167] (symbols) compared with the power law in Eq. (3.2)

The number of primary particles,  $N_{pri}$  was estimated from  $f_v$  and  $d_p$  assuming spherical primary particles with fixed size during the process. Using minimum, maximum, and mean of  $d_p$  from TEM measurements provides a range of expected  $N_{pri}$  can be obtained.

$$N_{pri} = \frac{f_v}{\pi d_p^3 / 6}. \quad (3.3)$$

### 3.2.3.3 Modelling soot yield and morphology

Fig. 3.30 compares predicted  $f_v$  and  $d_p$  with data. The horizontal scatter bars denote the uncertainty in the residence time corresponding to the TEM measurement. EBridge Modified and Irreversible Dimerization predicted soot volume fraction in close agreement with measurements, but Reactive Dimerization and Dimer Coalescence overpredict  $f_v$  by a factor of 2-3. On the other hand,  $d_p$  is significantly underestimated by all PAH growth models. Reactive Dimerization yields the largest  $d_p$  nearly 6 nm due to stronger PAH adsorption rate.

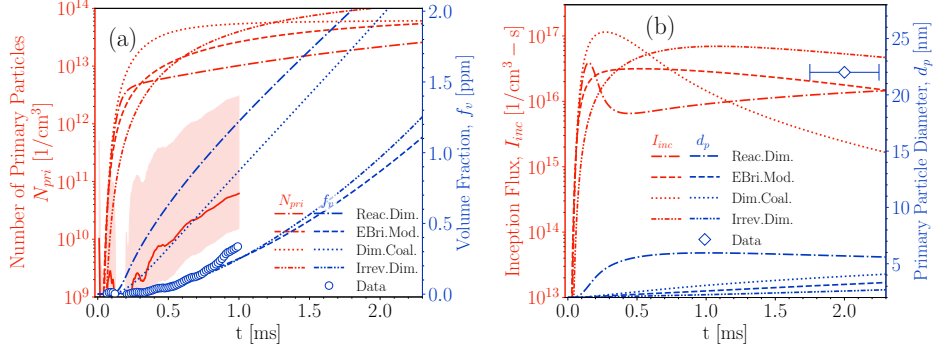


Figure 3.30: The soot volume fraction,  $f_v$  and number of primary particles,  $N_{pri}$  (left pane), and , the soot inception flux,  $I_{inc}$  and the primary particle diameter,  $d_p$  predicted by KAUST mechanism, SPBM, and different PAH growth models at  $T=2230$  K,  $P=4.5$  atm that corresponds to shock-tube conditions of TEM measurement

The underprediction of  $d_p$  by the PAH growth models despite producing enough or even more soot carbon mass compared with the measurement motivated a sensitivity analysis for soot yield and morphology. It should be noted that the sensitivity analysis is only focused on soot model to identify the sub-model(s) with the dominant effect on yield and morphology, and it does not include reactions in the gas phase.

First, the effect of HACA rate on soot yield and morphology is examined for the data point with  $T=2230$  K and  $P=4.5$  atm. To this purpose, the surface reactivity,  $\alpha$ , in HACA formulation is modified by introducing a damping factor,  $\zeta$  in Eq. (2.79) as:

$$\alpha^i = \tanh \left( \frac{12.56 - 0.00563 \cdot \zeta T}{\log_{10} \left( \frac{\rho_{soot} \cdot Av}{W_{carbon}} \frac{\pi}{6} d_p^3 \right)} - 1.38 + 0.00068 \cdot \zeta T \right). \quad (3.4)$$

Note that, there are many adjustable parameters in HACA scheme such as rate constants. We picked  $\zeta$  to modify  $\alpha$  for a number of reasons: First,  $\alpha$  was initially introduced as a tuning parameter as a function of local temperature and primary particle diameter to control surface growth rate, and it has been usually adjusted specifically for each flame [173, 129] to match the predicted volume fraction with the measurements. Second, the global empirical relation of Appel et al. [58] (used in omnisoott to quantify  $\alpha$ ) developed by fitting parameters of  $\alpha$  to minimize the prediction error of volume fraction for various premixed flames, but shock tubes generally have larger temperature ranges compared with premixed flames, which could excessively reduce surface reactivity and HACA growth rates. Finally, larger volume fractions (in the order of few ppm) were underpredicted by the global  $\alpha$  relation (Fig. 9 of [58]). So, the low values of  $\alpha$  in the shock tube at  $T=2230$  K corresponding to process conditions of TEM measurements can contribute to underprediction of surface growth rates and  $d_p$ . We introduce  $\zeta$  to reduce the damping effect of temperature on surface reactivity that promote HACA growth rates resulting in larger primary particle diameters, and possibly lessen the discrepancy between predicted and measured  $d_p$ . Fig. 3.31 demonstrates the variation of  $\alpha$  with temperature for  $\zeta=0.6, 0.8, 1$  and primary particle diameter 2 and 6 nm.  $\alpha$  decreases with temperature, and it is inversely proportional to  $\zeta$ .

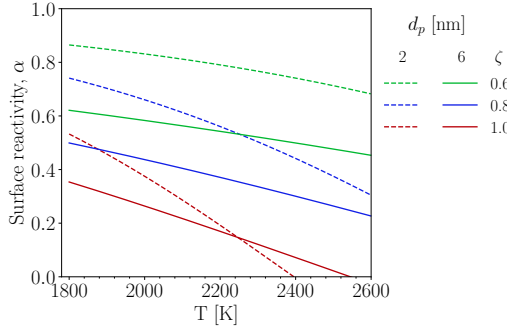


Figure 3.31: The variation of surface reactivity,  $\alpha$ , as a function of temperature for different values of  $\zeta$  and primary particle size of 2 nm (dashed lines) and 6 nm (solid lines)

A series of simulations was performed to study the damping effect of temperature on soot mass and morphology by varying  $\zeta$  from 1 to 0.8 and 0.6. Note that,  $\zeta$  of 1 represent the original  $\alpha$  formulation. The reaction mechanism and particle dynamic model were set to KAUST and SPBM, respectively. Fig. 3.32 depicts the volume fraction variation for each PAH growth model using different  $\zeta$  values. As expected, lowering  $\zeta$  increases the soot volume fraction with a maximum of 29% at  $t=2$  ms for Dimer Coalescence. However, as shown in Fig. 3.33  $\zeta$  has negligible effect on  $d_p$  with all PAH growth models. As a result, HACA growth rate cannot account for the observed gap between measure and predicted primary particle within 2 ms of the simulation of shock tube.

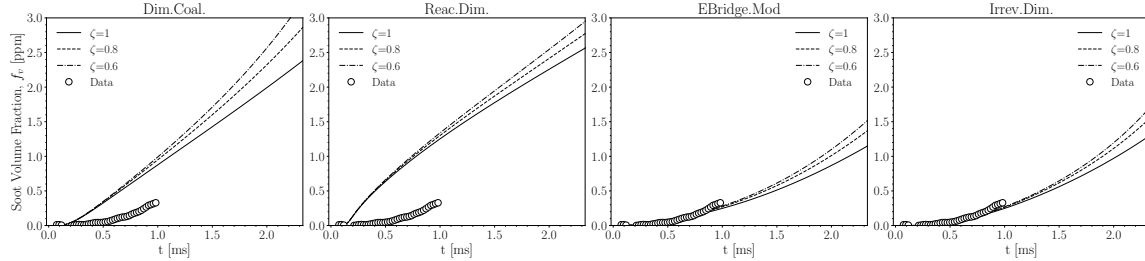


Figure 3.32: The effect of reducing  $\zeta$  leading to larger HACA rates on soot volume fraction,  $f_v$  using KAUST, SPBM and different PAH growth model

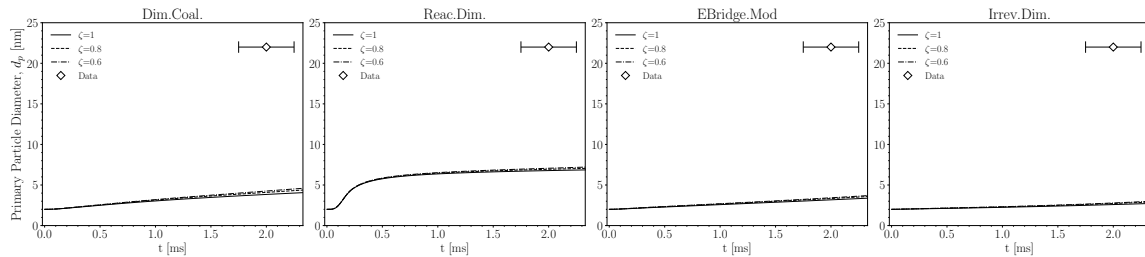


Figure 3.33: The effect of reducing  $\zeta$  leading to larger HACA rates on primary particle diameter,  $d_p$  using KAUST and MPBM and different PAH growth model

There is evidence supporting the coalescence (or sintering) of soot particles at initial stages of formation. The TEM images collected thermophoretically [174] near the inception zone of a burner-stabilized laminar premixed ethylene–oxygen–argon flame ( $\phi = 2.5$ ) showed particles with apparent sizes larger than those measured by Scanning Mobility Particle Sizer (SMPS) [175] suggesting that the particles flatten on the TEM grid upon impact. In other words, incipient and nascent soot

particles may have a liquid-like state that quickly transforms to a fully solid particles due to soot aging and maturity [45]. At initial stages, these particles can coalesce (merge) upon collision forming larger primary particles. There are a few experimental studies on soot coalescence. Ono et al. [17] reheated size-selected particles with a differential mobility analyzer formed during pyrolysis of ethylene and benzene in a secondary reactor and observed the morphological changes by comparing the TEM images. Matsukawa et al. [176] proposed a relation based on solid-state sintering mechanism of metallic nano-particles to describe characteristic sintering time of soot as:

$$\tau_c^i = A(d_p^i)^4 \cdot T \cdot \exp\left(\frac{E_a}{RT}\right), \quad (3.5)$$

where  $A = 3.0110^{22}[\text{s}/\text{m}^4 - \text{K}]$  and  $E_a = 1.4010^5[\text{J/mol}]$  are the prefactor, and activation energy, respectively, that are determined by curve-fitting to the change in primary particle diameter of soot after reheating in a flow reactor. Coalescence does not affect the agglomerate mass, but rather decreases the surface area of an agglomerate by merging primary particles. Coalescence is described in omnisoot by adding another partial source term to Eq. 2.68 as:

$$(S_{N_{pri}})_{coal} = -\frac{3}{\tau_c^i} \left( n_p^i - (n_p^i)^{2/3} \right) N_{agg}^i \quad (3.6)$$

Fig. 3.34 depicts the decrease in  $f_v$  by considering coalescence because of reduction in the surface area of agglomerates hence the number of active sites for HACA growth. As shown in Fig. 3.35, coalescence increases  $d_p$  with a maximum of 64% for Dimer Coalescence, but it cannot account for the significant underprediction of primary particle diameter by the model.

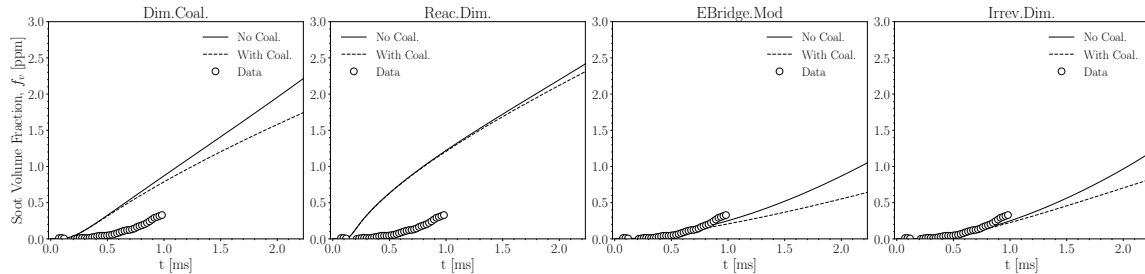


Figure 3.34: The effect of coalescence on soot volume fraction,  $f_v$  using KAUST, SPBM and different PAH growth model

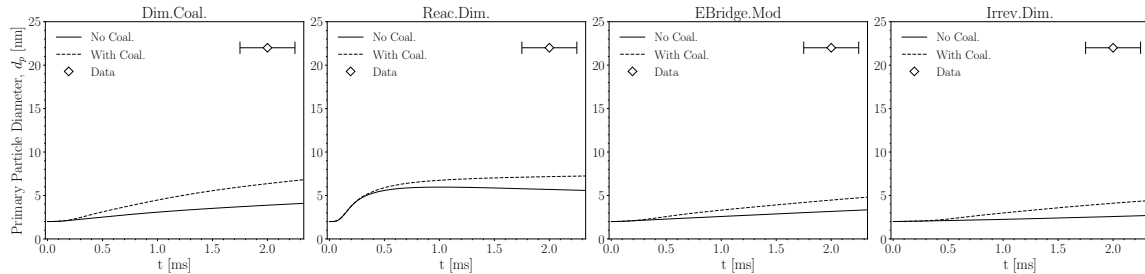


Figure 3.35: The effect of coalescence on primary particle diameter,  $d_p$  using KAUST and SPBM and different PAH growth model

The next step is examining the effect on inception and PAH adsorption on predicted soot volume fraction and primary particle diameter. This is achieved by introducing two prefactors,  $\delta$  and  $\eta$  to adjust inception flux and PAH adsorption rate, respectively. Nine different simulation cases are designed by assigning 1, 0.01, 0.001 to  $\delta$  and 1, 10, 100 to  $\eta$  where the case with  $\delta, \eta = 1$  corresponds to the default PAH growth parameters. Fig. 3.36 and 3.37 shows modifying  $\delta$  and  $\eta$

values in Reactive Dimerization model can significantly change the  $f_v$  and  $d_p$ . Modified primary particle diameter values increased large enough to cover the gap between TEM measurements and simulations. By introducing the same prefactors in the rest of PAH growth model, we noticed that  $d_p$  exhibits a similar sensitivity with respect to  $\delta$  and  $\eta$  values. Therefore, the inception flux and increasing the PAH adsorption rate are the major factors that determine primary particle size and soot yield in shock-tube simulations.

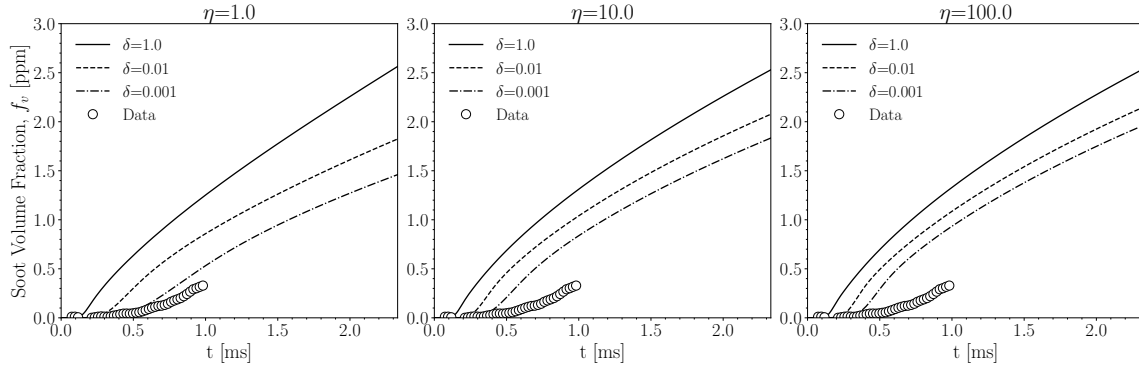


Figure 3.36: The effect of inception flux and PAH adsorption rate on soot volume fraction,  $f_v$ , using KAUST, Reactive Dimerization and SPBM

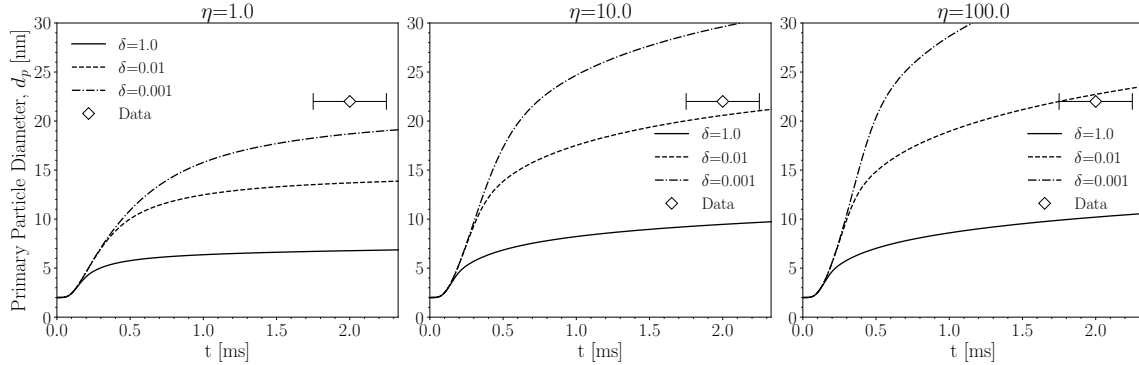


Figure 3.37: The effect of inception flux and PAH adsorption rate on primary particle diameter,  $d_p$  using KAUST, Reactive Dimerization and SPBM

Now that the importance of inception and PAH adsorption is demonstrated, a systematic analysis will be conducted for each PAH growth model by altering  $\delta$  and  $\eta$  to determine the rate constants that minimize the prediction error of both  $f_v$  and  $d_p$ . The weighted average of mean square error of  $f_v$  and  $d_p$  was used to calculate the total error. We employ a two-step grid search for all PAH growth models. In the first step, both  $\delta$  and  $\eta$  are divided and multiplied by a series factors ranging 1- $10^4$ , respectively, leading to 81 simulations in total. The simulation case with the lowest error is used as the starting point for the second grid search by perturbing  $\delta$  and  $\eta$  between -50% and +50%, leading to 45 simulations. It is important to note that the purpose of optimization is not necessarily finding the global minimum of cost function (the combined error of  $d_p$  and  $f_v$ ), but rather to show that it is possible to predict both  $f_v$  and  $d_p$  in good agreement with data by adjusting the inception flux and PAH adsorption rate ensuring that the rate constants stay within their physical limit. The agreement between data and predictions using optimized PAH growth models shown in Fig. 3.38 confirms the above-mentioned conclusion. Interestingly, the predicted  $N_{pir}$  by all PAH growth models reach a plateau of  $10^{11} [1/cm^3]$  and fall in the range inferred from extinction and TEM measurements. The inception flux,  $I_{inc}$  of PAH growth models shows similar behavior spanning over

the range of  $\approx 3 \times 10^{12} [1/cm^3 \cdot s]$  to  $\approx 3 \times 10^{14} [1/cm^3 \cdot s]$ . But, they also have noticeable differences. While Dimer Coalescence starts with a quick rise in inception flux followed by a decrease toward the end of test time, Reactive Dimerization predicts a more uniform inception over the simulated time.

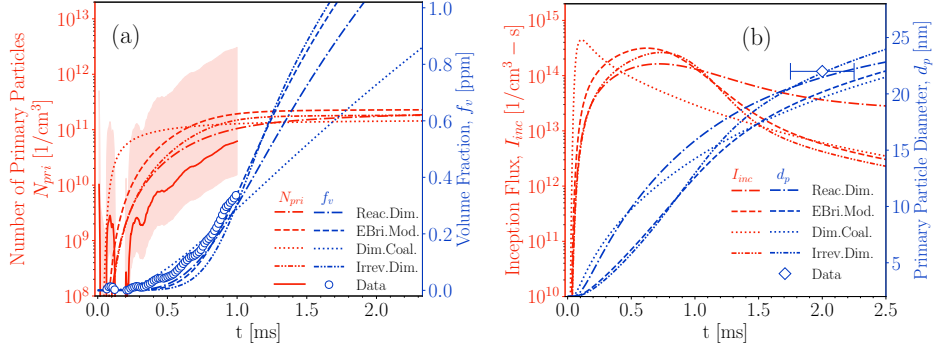


Figure 3.38: The soot volume fraction,  $f_v$  and number of primary particles,  $N_{pri}$  (left pane), the soot inception flux,  $I_{inc}$  and the primary particle diameter,  $d_p$  predicted by KAUST mechanism, SPBM, and different PAH growth models with optimized rate at  $T=2230$  K,  $P=4.5$  atm that corresponds to shock-tube conditions of TEM measurement

The PAH growth models with optimized rates were applied to the whole temperature and pressure ranges (see Fig. B.23 and B.24). As shown in Fig. 3.39, the measured  $f_v$  demonstrates a relatively strong sensitivity to temperature best captured by EBridge Formation. This model start with a temperature-dependent dehydrogenation step, but other model are initiated with PAH collision that weakly depends on temperature. On the other hand, Dimer Coalescence is least sensitive to temperature. While it slightly underestimates  $f_v$  at  $T=2085$  K, it predicts soot volume fraction four time larger than data at  $T=2406$  K. The evolution of primary particle diameter,  $d_p$  seems to not be considerably affected with temperature in  $2000 \text{ K} < T < 2400$  K. The  $d_p$  using optimized PAH growth models is calculated at  $t=2$  ms and plotted for the studied  $T_5$  range in Fig. 3.41 that shows a bell-like temperature dependency with peak around 2200 K for all PAH growth models.

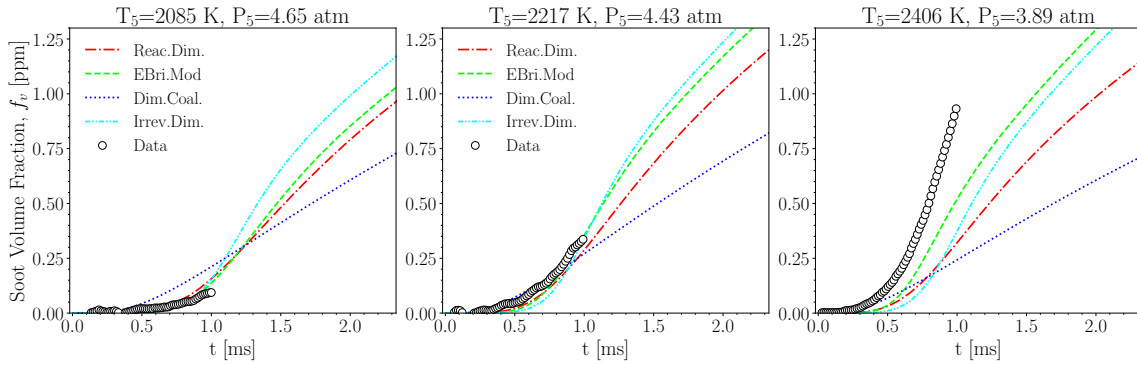


Figure 3.39: The soot volume fraction,  $f_v$  over  $2000 \text{ K} < T < 2400$  K, using KAUST, SPBM, and optimized inception models

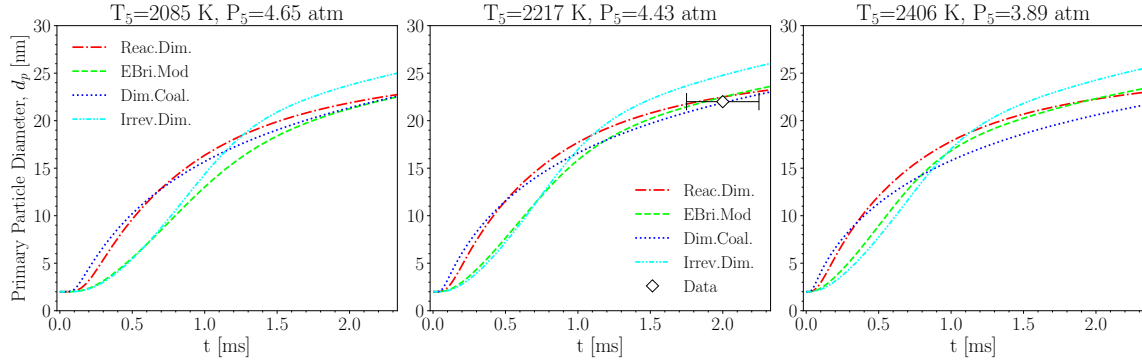


Figure 3.40: The primary particle diameter,  $d_p$  over  $2000 \text{ K} < T < 2400 \text{ K}$ , using KAUST, SPBM, and optimized inception models

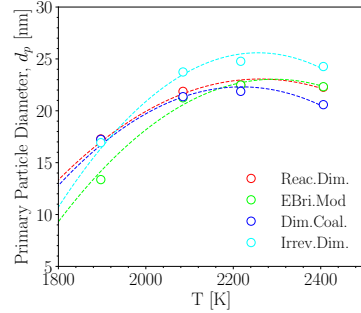


Figure 3.41: The primary particle diameter,  $d_p$  at  $t=2 \text{ ms}$  over the studied temperature range using KAUST, SPBM, and optimized inception models. The dashed line is added to guide the eye.

# Bibliography

- [1] GL Agafonov, IV Bilera, PA Vlasov, IV Zhil'tsova, Yu A Kolbanovskii, VN Smirnov, and AM Tereza. Unified kinetic model of soot formation in the pyrolysis and oxidation of aliphatic and aromatic hydrocarbons in shock waves. *Kinetics and Catalysis*, 57:557–572, 2016.
- [2] Gunnar Myhre, Drew Shindell, and Julia Pongratz. Anthropogenic and natural radiative forcing. 2014.
- [3] World Health Organization et al. Health effects of particulate matter: Policy implications for countries in eastern europe, caucasus and central asia. 2013.
- [4] U.S. EPA. Integrated science assessment (isa) for particulate matter (final report, dec 2019). 2019.
- [5] Ann Y Watson and Peter A Valberg. Carbon black and soot: two different substances. *AIHAJ-American Industrial Hygiene Association*, 62(2):218–228, 2001.
- [6] International Carbon Black Association et al. Carbon black user's guide. *available at www.carbon-black.org*, 2016.
- [7] Verónica Palomares, Aintzane Goñi, Izaskun Gil De Muro, Iratxe De Meatza, Miguel Ben-goechea, Igor Cantero, and Teófilo Rojo. Conductive additive content balance in li-ion battery cathodes: Commercial carbon blacks vs. in situ carbon from lifepo<sub>4</sub>/c composites. *J. Power Sources*, 195:7661–7668, 2010. ISSN 0378-7753.
- [8] Sotiris E Pratsinis. History of manufacture of fine particles in high-temperature aerosol reactors. *Aerosol science and technology: History and reviews*, pages 475–507, 2011.
- [9] Roop Chand Bansal, Meng-Jiao Wang, and JB Donnet. Carbon black. *Science and Technology*, 133, 1993.
- [10] Wonihl Cho, Seung-Ho Lee, Woo-Sung Ju, Youngsoon Baek, and Joong Kee Lee. Conversion of natural gas to hydrogen and carbon black by plasma and application of plasma carbon black. *Catalysis Today*, 98(4):633–638, 2004.
- [11] Soo-Jin Park, Min-Kang Seo, and Changwoon Nah. Influence of surface characteristics of carbon blacks on cure and mechanical behaviors of rubber matrix compoundings. *Journal of colloid and interface science*, 291(1):229–235, 2005.
- [12] C Russo, A Tregrossi, and A Ciajolo. Dehydrogenation and growth of soot in premixed flames. *Proceedings of the Combustion Institute*, 35(2):1803–1809, 2015.
- [13] Madhu Singh and Randy L Vander Wal. Nanostructure quantification of carbon blacks. *C*, 5 (1):2, 2018.
- [14] Randy L Vander Wal, Aleksey Yezerets, Neal W Currier, Do Heui Kim, and Chong Min Wang. Hrtem study of diesel soot collected from diesel particulate filters. *Carbon*, 45(1):70–77, 2007.

- [15] Magín Lapuerta, Javier Barba, Anton D Sediako, Mohammad Reza Kholghy, and Murray J Thomson. Morphological analysis of soot agglomerates from biodiesel surrogates in a coflow burner. *Journal of Aerosol Science*, 111:65–74, 2017.
- [16] Andrea D’Anna. Combustion-formed nanoparticles. *Proceedings of the Combustion Institute*, 32(1):593–613, 2009.
- [17] Kiminori Ono, Kazuki Dewa, Yoshiya Matsukawa, Yasuhiro Saito, Yohsuke Matsushita, Hideyuki Aoki, Koki Era, Takayuki Aoki, and Togo Yamaguchi. Experimental evidence for the sintering of primary soot particles. *Journal of Aerosol Science*, 105:1–9, 2017.
- [18] Jiangjun Wei, Yang Zeng, Mingzhang Pan, Yuan Zhuang, Liang Qiu, Taotao Zhou, and Yongqiang Liu. Morphology analysis of soot particles from a modern diesel engine fueled with different types of oxygenated fuels. *Fuel*, 267:117248, 2020.
- [19] M Alfè, B Apicella, Rouzaud Barbella, J-N Rouzaud, A Tregrossi, and A Ciajolo. Structure–property relationship in nanostructures of young and mature soot in premixed flames. *Proceedings of the Combustion Institute*, 32(1):697–704, 2009.
- [20] Stephen E Stein and A Fahr. High-temperature stabilities of hydrocarbons. *The Journal of Physical Chemistry*, 89(17):3714–3725, 1985.
- [21] Hai Wang. Formation of nascent soot and other condensed-phase materials in flames. *Proc Combust Inst.*, 33:41–67, 2011. ISSN 15407489.
- [22] Michael Frenklach. Reaction mechanism of soot formation in flames. *Physical chemistry chemical Physics*, 4(11):2028–2037, 2002.
- [23] Askar Fahr and SE Stein. Reactions of vinyl and phenyl radicals with ethyne, ethene and benzene. In *Symposium (International) on Combustion*, volume 22, pages 1023–1029. Elsevier, 1989.
- [24] KO Johansson, MP Head-Gordon, PE Schrader, KR Wilson, and HA Michelsen. Resonance-stabilized hydrocarbon-radical chain reactions may explain soot inception and growth. *Science*, 361(6406):997–1000, 2018.
- [25] Michael Frenklach and Alexander M Mebel. On the mechanism of soot nucleation. *Physical Chemistry Chemical Physics*, 22(9):5314–5331, 2020.
- [26] Michael Frenklach and Lawrence B Ebert. Comment on the proposed role of spheroidal carbon clusters in soot formation. *The Journal of Physical Chemistry*, 92(2):561–563, 1988.
- [27] Bin Zhao, Zhiwei Yang, Murray V Johnston, Hai Wang, Anthony S Wexler, Michael Balthasar, and Markus Kraft. Measurement and numerical simulation of soot particle size distribution functions in a laminar premixed ethylene-oxygen-argon flame. *Combustion and Flame*, 133 (1-2):173–188, 2003.
- [28] Aamir D Abid, Joaquin Camacho, David A Sheen, and Hai Wang. Quantitative measurement of soot particle size distribution in premixed flames—the burner-stabilized stagnation flame approach. *Combustion and Flame*, 156(10):1862–1870, 2009.
- [29] Joachim Happold, Horst-Henning Grotheer, and Manfred Aigner. Soot precursors consisting of stacked pericondensed pahs. *Combustion generated fine carbonaceous particles*, pages 275–285, 2009.
- [30] Jennifer D Herdman and J Houston Miller. Intermolecular potential calculations for polynuclear aromatic hydrocarbon clusters. *The Journal of Physical Chemistry A*, 112(28):6249–6256, 2008.

- [31] Tim S Totton, Alston J Misquitta, and Markus Kraft. A quantitative study of the clustering of polycyclic aromatic hydrocarbons at high temperatures. *Physical chemistry chemical physics*, 14(12):4081–4094, 2012.
- [32] David Wong, R Whitesides, CA Schuetz, and M Frenklach. Molecular dynamics simulations of pah dimerization. *Combustion Generated Fine Carbonaceous Particles*, pages 247–257, 2009.
- [33] Jeremy P Cain, Joaquin Camacho, Denis J Phares, Hai Wang, and Alexander Laskin. Evidence of aliphatics in nascent soot particles in premixed ethylene flames. *Proceedings of the Combustion Institute*, 33(1):533–540, 2011.
- [34] Bin Zhao, Zhiwei Yang, Zhigang Li, Murray V Johnston, and Hai Wang. Particle size distribution function of incipient soot in laminar premixed ethylene flames: effect of flame temperature. *Proceedings of the Combustion Institute*, 30(1):1441–1448, 2005.
- [35] Jacob W Martin, Maurin Salamanca, and Markus Kraft. Soot inception: Carbonaceous nanoparticle formation in flames. *Progress in Energy and Combustion Science*, 88:100956, 2022.
- [36] Angela Violi, Gregory A Voth, and Adel F Sarofim. The relative roles of acetylene and aromatic precursors during soot particle inception. *Proceedings of the Combustion Institute*, 30(1):1343–1351, 2005.
- [37] Mohammad Reza Kholghy, Yashar Afarin, Anton D Sediako, Javier Barba, Magín Lapuerta, Carson Chu, Jason Weingarten, Bobby Borshanpour, Victor Chernov, and Murray J Thomson. Comparison of multiple diagnostic techniques to study soot formation and morphology in a diffusion flame. *Combustion and Flame*, 176:567–583, 2017.
- [38] Christopher R Shaddix and Kermit C Smyth. Laser-induced incandescence measurements of soot production in steady and flickering methane, propane, and ethylene diffusion flames. *Combustion and flame*, 107(4):418–452, 1996.
- [39] Nimeti Doner and Fengshan Liu. Impact of morphology on the radiative properties of fractal soot aggregates. *Journal of Quantitative Spectroscopy and Radiative Transfer*, 187:10–19, 2017.
- [40] Michael Frenklach and Hai Wang. Detailed modeling of soot particle nucleation and growth. In *Symposium (International) on Combustion*, volume 23, pages 1559–1566. Elsevier, 1991.
- [41] Steffen Salenbauch, Alberto Cuoci, Alessio Frassoldati, Chiara Saggese, Tiziano Faravelli, and Christian Hasse. Modeling soot formation in premixed flames using an extended conditional quadrature method of moments. *Combustion and Flame*, 162(6):2529–2543, 2015.
- [42] Pascale Desgroux, Alessandro Faccinetto, Xavier Mercier, Thomas Mouton, Damien Aubagnac Karkar, and Abderrahman El Bakali. Comparative study of the soot formation process in a “nucleation” and a “sooting” low pressure premixed methane flame. *Combustion and Flame*, 184:153–166, 2017.
- [43] Yu Wang, Abhijeet Raj, and Suk Ho Chung. Soot modeling of counterflow diffusion flames of ethylene-based binary mixture fuels. *Combustion and Flame*, 162(3):586–596, 2015.
- [44] Lei Xu, Fuwu Yan, Mengxiang Zhou, and Yu Wang. An experimental and modeling study on sooting characteristics of laminar counterflow diffusion flames with partial premixing. *Energy*, 218:119479, 2021.
- [45] Mohammad Reza Kholghy, Armin Veshkini, and Murray John Thomson. The core–shell internal nanostructure of soot—a criterion to model soot maturity. *Carbon*, 100:508–536, 2016.
- [46] Armin Veshkini, Seth B Dworkin, and Murray J Thomson. Understanding soot particle size evolution in laminar ethylene/air diffusion flames using novel soot coalescence models. *Combustion Theory and Modelling*, 20(4):707–734, 2016.

- [47] J Houston Miller, Kermit C Smyth, and W Gary Mallard. Calculations of the dimerization of aromatic hydrocarbons: Implications for soot formation. In *Symposium (International) on Combustion*, volume 20, pages 1139–1147. Elsevier, 1985.
- [48] Hassan Sabbah, Ludovic Biennier, Stephen J Klippenstein, Ian R Sims, and Bertrand R Rowe. Exploring the role of pahs in the formation of soot: Pyrene dimerization. *The Journal of Physical Chemistry Letters*, 1(19):2962–2967, 2010.
- [49] Ali Naseri, M Reza Kholghy, Neil A Juan, and Murray J Thomson. Simulating yield and morphology of carbonaceous nanoparticles during fuel pyrolysis in laminar flow reactors enabled by reactive inception and aromatic adsorption. *Combustion and Flame*, 237:111721, 2022.
- [50] Nazly E Sanchez, Alicia Callejas, Angela Millera, Rafael Bilbao, and Maria U Alzueta. Polycyclic aromatic hydrocarbon (pah) and soot formation in the pyrolysis of acetylene and ethylene: effect of the reaction temperature. *Energy & fuels*, 26(8):4823–4829, 2012.
- [51] Sanghwan Cho, Seunghoon Lee, Wonnam Lee, and Sunho Park. Synthesis of primary-particle-size-tuned soot particles by controlled pyrolysis of hydrocarbon fuels. *Energy & Fuels*, 30(8):6614–6619, 2016.
- [52] Meghdad Saffaripour, Armin Veshkini, Mohammadreza Kholghy, and Murray J Thomson. Experimental investigation and detailed modeling of soot aggregate formation and size distribution in laminar coflow diffusion flames of jet a-1, a synthetic kerosene, and n-decane. *Combustion and Flame*, 161(3):848–863, 2014.
- [53] J Houston Miller. The kinetics of polynuclear aromatic hydrocarbon agglomeration in flames. In *Symposium (International) on Combustion*, volume 23, pages 91–98. Elsevier, 1991.
- [54] Anna Giordana, Andrea Maranzana, and Glauco Tonachini. Theoretical investigation of soot nanoparticle inception via polycyclic aromatic hydrocarbon coagulation (condensation): Energetic, structural, and electronic features. *The Journal of Physical Chemistry C*, 115(5):1732–1739, 2011.
- [55] NA Eaves, SB Dworkin, and MJ Thomson. The importance of reversibility in modeling soot nucleation and condensation processes. *Proceedings of the Combustion Institute*, 35(2):1787–1794, 2015.
- [56] Mohammad Reza Kholghy, Nick Anthony Eaves, Armin Veshkini, and Murray John Thomson. The role of reactive pah dimerization in reducing soot nucleation reversibility. *Proceedings of the Combustion Institute*, 37(1):1003–1011, 2019.
- [57] Mohammad R Kholghy, Georgios A Kelesidis, and Sotiris E Pratsinis. Reactive polycyclic aromatic hydrocarbon dimerization drives soot nucleation. *Physical Chemistry Chemical Physics*, 20(16):10926–10938, 2018.
- [58] Jörg Appel, Henning Bockhorn, and Michael Frenklach. Kinetic modeling of soot formation with detailed chemistry and physics: laminar premixed flames of c2 hydrocarbons. *Combustion and flame*, 121(1-2):122–136, 2000.
- [59] IT Woods and BS Haynes. Soot surface growth at active sites. *Combustion and flame*, 85 (3-4):523–525, 1991.
- [60] Cameron J Dasch. The decay of soot surface growth reactivity and its importance in total soot formation. *Combustion and flame*, 61(3):219–225, 1985.
- [61] Hope A Michelsen, Meredith B Colket, Per-Erik Bengtsson, Andrea D’anna, Pascale Desgroux, Brian S Haynes, J Houston Miller, Graham J Nathan, Heinz Pitsch, and Hai Wang. A review of terminology used to describe soot formation and evolution under combustion and pyrolytic conditions. *ACS nano*, 14(10):12470–12490, 2020.

- [62] OI Obolensky, VV Semenikhina, AV Solov'Yov, and W Greiner. Interplay of electrostatic and van der waals forces in coronene dimer. *International Journal of Quantum Chemistry*, 107(6):1335–1343, 2007.
- [63] Eirini Goudeli, Maximilian L Eggersdorfer, and Sotiris E Pratsinis. Coagulation of agglomerates consisting of polydisperse primary particles. *Langmuir*, 32:9276–9285, 2016. ISSN 0743-7463.
- [64] FS Lai, SK Friedlander, J Pich, and GM Hidy. The self-preserving particle size distribution for brownian coagulation in the free-molecule regime. *Journal of Colloid and Interface Science*, 39(2):395–405, 1972.
- [65] Raymond D Mountain, George W Mulholland, and Howard Baum. Simulation of aerosol agglomeration in the free molecular and continuum flow regimes. *Journal of Colloid and Interface Science*, 114(1):67–81, 1986.
- [66] Georgios A. Kelesidis, Eirini Goudeli, and Sotiris E. Pratsinis. Morphology and mobility diameter of carbonaceous aerosols during agglomeration and surface growth. *Carbon*, 121:527–535, 9 2017. ISSN 00086223.
- [67] Georgios A Kelesidis and Eirini Goudeli. Self-preserving size distribution and collision frequency of flame-made nanoparticles in the transition regime. *Proceedings of the Combustion Institute*, 38(1):1233–1240, 2021.
- [68] Georgios A. Kelesidis, Eirini Goudeli, and Sotiris E. Pratsinis. Flame synthesis of functional nanostructured materials and devices: Surface growth and aggregation. *Proc Combust Inst* ., 36:29–50, 2017. ISSN 15407489.
- [69] Georgios A Kelesidis and Sotiris E Pratsinis. A perspective on gas-phase synthesis of nanomaterials: Process design, impact and outlook. *Chemical Engineering Journal*, 421:129884, 2021.
- [70] Yun Xiong and Sotiris E Pratsinis. Formation of agglomerate particles by coagulation and sintering—part i. a two-dimensional solution of the population balance equation. *J. Aerosol Sci.*, 24:283–300, 1993. ISSN 0021-8502.
- [71] SH Park, SN Rogak, WK Bushe, JZ Wen, and MJ Thomson. An aerosol model to predict size and structure of soot particles. *Combustion Theory and Modelling*, 9(3):499–513, 2005.
- [72] MA Schiener and RP Lindstedt. Transported probability density function based modelling of soot particle size distributions in non-premixed turbulent jet flames. *Proceedings of the Combustion Institute*, 37(1):1049–1056, 2019.
- [73] Themis Matsoukas and Sheldon K Friedlander. Dynamics of aerosol agglomerate formation. *Journal of Colloid and Interface Science*, 146(2):495–506, 1991.
- [74] MD Smooke, MB Long, BC Connelly, MB Colket, and RJ Hall. Soot formation in laminar diffusion flames. *Combustion and Flame*, 143(4):613–628, 2005.
- [75] Damien Aubagnac-Karkar, Abderrahman El Bakali, and Pascale Desgroux. Soot particles inception and pah condensation modelling applied in a soot model utilizing a sectional method. *Combustion and Flame*, 189:190–206, 2018.
- [76] Andrei Kazakov and Michael Frenklach. Dynamic modeling of soot particle coagulation and aggregation: Implementation with the method of moments and application to high-pressure laminar premixed flames. *Combustion and flame*, 114(3-4):484–501, 1998.
- [77] F Eimar Kruis, Karl A Kusters, Sotiris E Pratsinis, and Brian Scarlett. A simple model for the evolution of the characteristics of aggregate particles undergoing coagulation and sintering. *Aerosol science and technology*, 19(4):514–526, 1993.

- [78] Patrick T Spicer, Olivier Chaoul, Stavros Tsantilis, and Sotiris E Pratsinis. Titania formation by  $\text{tio}_4$  gas phase oxidation, surface growth and coagulation. *J. Aerosol Sci.*, 33:17–34, 2002. ISSN 0021-8502.
- [79] Georgios A Kelesidis and Sotiris E Pratsinis. Estimating the internal and surface oxidation of soot agglomerates. *Combustion and Flame*, 209:493–499, 2019.
- [80] Aamir D Abid, Nicholas Heinz, Erik D Tolmachoff, Denis J Phares, Charles S Campbell, and Hai Wang. On evolution of particle size distribution functions of incipient soot in premixed ethylene–oxygen–argon flames. *Combustion and Flame*, 154(4):775–788, 2008.
- [81] X Ma, CD Zangmeister, and MR Zachariah. Soot oxidation kinetics: a comparison study of two tandem ion-mobility methods. *The Journal of Physical Chemistry C*, 117(20):10723–10729, 2013.
- [82] Joaquin Camacho, Changran Liu, Chen Gu, He Lin, Zhen Huang, Quanxi Tang, Xiaoqing You, Chiara Saggese, Yang Li, Heejung Jung, et al. Mobility size and mass of nascent soot particles in a benchmark premixed ethylene flame. *Combustion and Flame*, 162(10):3810–3822, 2015.
- [83] Arto J Gröhn, Sotiris E Pratsinis, and Karsten Wegner. Fluid-particle dynamics during combustion spray aerosol synthesis of  $\text{zro}_2$ . *Chemical Engineering Journal*, 191:491–502, 2012.
- [84] Sotiris E Pratsinis. Simultaneous nucleation, condensation, and coagulation in aerosol reactors. *Journal of colloid and interface science*, 124(2):416–427, 1988.
- [85] Guillaume Blanquart and Heinz Pitsch. A joint volume-surface-hydrogen multi-variate model for soot formation. *Combustion generated fine carbonaceous particles*, pages 437–463, 2009.
- [86] G Blanquart and H Pitsch. Analyzing the effects of temperature on soot formation with a joint volume-surface-hydrogen model. *Combustion and Flame*, 156(8):1614–1626, 2009.
- [87] Kyo-Seon Kim and Sotiris E Pratsinis. Manufacture of optical waveguide preforms by modified chemical vapor deposition. *AIChE journal*, 34(6):912–921, 1988.
- [88] Michael Frenklach and Stephen J Harris. Aerosol dynamics modeling using the method of moments. *Journal of colloid and interface science*, 118(1):252–261, 1987.
- [89] Stavros Tsantilis and Sotiris E Pratsinis. Soft-and hard-agglomerate aerosols made at high temperatures. *Langmuir*, 20(14):5933–5939, 2004.
- [90] Peter R Lindstedt. Simplified soot nucleation and surface growth steps for non-premixed flames. In *Soot formation in combustion: mechanisms and models*, pages 417–441. Springer, 1994.
- [91] Kin M Leung, Rune P Lindstedt, and William P Jones. A simplified reaction mechanism for soot formation in nonpremixed flames. *Combustion and flame*, 87(3-4):289–305, 1991.
- [92] Robert N Grass, Stavros Tsantilis, and Sotiris E Pratsinis. Design of high-temperature, gas-phase synthesis of hard or soft  $\text{tio}_2$  agglomerates. *AIChE Journal*, 52(4):1318–1325, 2006.
- [93] Hope A Michelsen. Probing soot formation, chemical and physical evolution, and oxidation: A review of in situ diagnostic techniques and needs. *Proceedings of the Combustion Institute*, 36(1):717–735, 2017.
- [94] Rosalind E Franklin. Crystallite growth in graphitizing and non-graphitizing carbons. *Proceedings of the Royal Society of London. Series A. Mathematical and Physical Sciences*, 209 (1097):196–218, 1951.
- [95] Brian S Haynes and H Gg Wagner. Soot formation. *Progress in energy and combustion science*, 7(4):229–273, 1981.

- [96] Joaquin Camacho, Yujie Tao, and Hai Wang. Kinetics of nascent soot oxidation by molecular oxygen in a flow reactor. *Proceedings of the Combustion Institute*, 35(2):1887–1894, 2015.
- [97] Robert H Hurt, Gregory P Crawford, and Hong-Shig Shim. Equilibrium nanostructure of primary soot particles. *Proceedings of the Combustion Institute*, 28(2):2539–2546, 2000.
- [98] Charles S McEnally, Ümit Ö Köylü, Lisa D Pfefferle, and Daniel E Rosner. Soot volume fraction and temperature measurements in laminar nonpremixed flames using thermocouples. *Combustion and Flame*, 109(4):701–720, 1997.
- [99] Pascale Desgroux, Xavier Mercier, and Kevin A Thomson. Study of the formation of soot and its precursors in flames using optical diagnostics. *Proceedings of the Combustion Institute*, 34 (1):1713–1738, 2013.
- [100] Randy L Vander Wal and Aaron J Tomasek. Soot nanostructure: dependence upon synthesis conditions. *Combustion and Flame*, 136(1-2):129–140, 2004.
- [101] Nils-Erik Olofsson, Johan Simonsson, Sandra Török, Henrik Bladh, and Per-Erik Bengtsson. Evolution of properties for aging soot in premixed flat flames studied by laser-induced incandescence and elastic light scattering. *Applied Physics B*, 119:669–683, 2015.
- [102] A Eremin, E Gurentsov, E Popova, and K Priemchenko. Size dependence of complex refractive index function of growing nanoparticles. *Applied Physics B*, 104:285–295, 2011.
- [103] WH Dalzell and AF Sarofim. Optical constants of soot and their application to heat-flux calculations. 1969.
- [104] Jochen Zerbs, Klaus Peter Geigle, Oliver Lammel, Joachim Hader, Ronnie Stirn, Redjem Hadef, and Wolfgang Meier. The influence of wavelength in extinction measurements and beam steering in laser-induced incandescence measurements in sooting flames. *Applied Physics B*, 96:683–694, 2009.
- [105] Georgios A Kelesidis and Sotiris E Pratsinis. Determination of the volume fraction of soot accounting for its composition and morphology. *Proceedings of the Combustion Institute*, 38 (1):1189–1196, 2021.
- [106] Karthik V Puduppakkam, Abhijit U Modak, Chitralkumar V Naik, Joaquin Camacho, Hai Wang, and Ellen Meeks. A soot chemistry model that captures fuel effects. In *Turbo Expo: Power for Land, Sea, and Air*, volume 45691, page V04BT04A055. American Society of Mechanical Engineers, 2014.
- [107] Tami C Bond and Robert W Bergstrom. Light absorption by carbonaceous particles: An investigative review. *Aerosol science and technology*, 40(1):27–67, 2006.
- [108] J Tauc, Radu Grigorovici, and Anina Vancu. Optical properties and electronic structure of amorphous germanium. *physica status solidi (b)*, 15(2):627–637, 1966.
- [109] J Robertson and EP O’reilly. Electronic and atomic structure of amorphous carbon. *Physical Review B*, 35(6):2946, 1987.
- [110] Changran Liu, Ajay V Singh, Chiara Saggesse, Quanxi Tang, Dongping Chen, Kevin Wan, Marianna Vinciguerra, Mario Commodo, Gianluigi De Falco, Patrizia Minutolo, et al. Flame-formed carbon nanoparticles exhibit quantum dot behaviors. *Proceedings of the National Academy of Sciences*, 116(26):12692–12697, 2019.
- [111] Kim Cuong Le, Carmela Russo, Sandra Török, Barbara Apicella, Antonio Tregrossi, Per-Erik Bengtsson, and Anna Ciajolo. Soot optical band gap evaluated through in-situ and ex-situ measurements as tracer of soot evolution in premixed flames: Soot optical band gap evaluated through in-situ and ex-situ measurements as tracer of soot evolution in premixed flames. 2019.

- [112] Carmela Russo, Barbara Apicella, Antonio Tregrossi, Anna Ciajolo, Kim Cuong Le, Sandra Török, and Per-Erik Bengtsson. Optical band gap analysis of soot and organic carbon in premixed ethylene flames: comparison of in-situ and ex-situ absorption measurements. *Carbon*, 158:89–96, 2020.
- [113] Georgios A Kelesidis and Sotiris E Pratsinis. Soot light absorption and refractive index during agglomeration and surface growth. *Proceedings of the Combustion Institute*, 37(1):1177–1184, 2019.
- [114] Salma Bejaoui, Sébastien Batut, Eric Therssen, Nathalie Lamoureux, Pascale Desgroux, and Fengshan Liu. Measurements and modeling of laser-induced incandescence of soot at different heights in a flat premixed flame. *Applied Physics B*, 118:449–469, 2015.
- [115] Hope A Michelsen, Paul E Schrader, and Fabien Goulay. Wavelength and temperature dependences of the absorption and scattering cross sections of soot. *Carbon*, 48(8):2175–2191, 2010.
- [116] G Cléon, T Amodeo, A Faccinetto, and P Desgroux. Laser induced incandescence determination of the ratio of the soot absorption functions at 532 nm and 1064 nm in the nucleation zone of a low pressure premixed sooting flame. *Applied Physics B*, 104(2):297–305, 2011.
- [117] Junyu Mei, Yuxin Zhou, Xiaoqing You, and Chung K Law. Formation of nascent soot during very fuel-rich oxidation of ethylene at low temperatures. *Combustion and Flame*, 226:31–41, 2021.
- [118] Georgios A Kelesidis and Sotiris E Pratsinis. Santoro flame: The volume fraction of soot accounting for its morphology & composition. *Combustion and Flame*, 240:112025, 2022.
- [119] KG Neoh, JB Howard, and AF Sarofim. Soot oxidation in flames. *Particulate carbon: formation during combustion*, pages 261–282, 1981.
- [120] JS Lighty, V Romano, and AF Sarofim. Soot oxidation. In *Combustion generated fine carbonaceous particles (proceedings of an international workshop held in Villa Orlandi, Anacapri, May 13e16, 2007)*. KIT Scientific Publishing, pages 523–36, 2009.
- [121] Charles P Fenimore and George Wallace Jones. Oxidation of soot by hydroxyl radicals. *The Journal of physical chemistry*, 71(3):593–597, 1967.
- [122] KB Lee, MW Thring, and JM Beer. On the rate of combustion of soot in a laminar soot flame. *Combustion and Flame*, 6:137–145, 1962.
- [123] William Bartok and Adel F Sarofim. Fossil fuel combustion: a source book. 1991.
- [124] J Nagle and RF Strickland-Constable. Oxidation of carbon between 1000–2000 c. In *Proceedings of the fifth conference on carbon*, pages 154–164. Elsevier, 1962.
- [125] John PA Neeft, T Xander Nijhuis, Erik Smakman, Michiel Makkee, and Jacob A Moulijn. Kinetics of the oxidation of diesel soot. *Fuel*, 76(12):1129–1136, 1997.
- [126] Georgios A Kelesidis, Nicola Rossi, and Sotiris E Pratsinis. Porosity and crystallinity dynamics of carbon black during internal and surface oxidation. *Carbon*, 197:334–340, 2022.
- [127] Tomoji Ishiguro, Noritomo Suzuki, Yoshiyasu Fujitani, and Hidetake Morimoto. Microstructural changes of diesel soot during oxidation. *Combustion and Flame*, 85(1-2):1–6, 1991.
- [128] Juhun Song, Mahabubul Alam, André L Boehman, and Unjeong Kim. Examination of the oxidation behavior of biodiesel soot. *Combustion and flame*, 146(4):589–604, 2006.
- [129] F Xu, PB Sunderland, and GM Faeth. Soot formation in laminar premixed ethylene/air flames at atmospheric pressure. *Combustion and Flame*, 108(4):471–493, 1997.

- [130] RTFRJRA Puri, TF Richardson, RJ Santoro, and RA Dobbins. Aerosol dynamic processes of soot aggregates in a laminar ethene diffusion flame. *Combustion and flame*, 92(3):320–333, 1993.
- [131] David G. Goodwin, Harry K. Moffat, Ingmar Schoegl, Raymond L. Speth, and Bryan W. Weber. Cantera: An object-oriented software toolkit for chemical kinetics, thermodynamics, and transport processes. <https://www.cantera.org>, 2022. Version 2.6.0.
- [132] Samuel L Manzello, David B Lenhert, Ahmet Yozgatligil, Michael T Donovan, George W Mulholland, Michael R Zachariah, and Wing Tsang. Soot particle size distributions in a well-stirred reactor/plug flow reactor. *Proceedings of the Combustion Institute*, 31(1):675–683, 2007.
- [133] Kevin Gleason, Francesco Carbone, and Alessandro Gomez. Pahs controlling soot nucleation in 0.101—0.811 mpa ethylene counterflow diffusion flames. *Combustion and Flame*, 227:384–395, 2021.
- [134] Kevin Gleason and Alessandro Gomez. Soot nucleation in diffusion flames and the role of aromatic hydrocarbons. *Combustion and Flame*, 255:112899, 2023.
- [135] Kirk A Jensen, Jill M Suo-Anttila, and Linda G Blevins. Measurement of soot morphology, chemistry, and optical properties in the visible and near-infrared spectrum in the flame zone and overfire region of large jp-8 pool fires. *Combustion science and technology*, 179(12):2453–2487, 2007.
- [136] Bonnie J McBride. *Coefficients for calculating thermodynamic and transport properties of individual species*, volume 4513. National Aeronautics and Space Administration, Office of Management . . . , 1993.
- [137] Robert J Kee, Michael E Coltrin, Peter Glarborg, and Huayang Zhu. *Chemically reacting flow: theory, modeling, and simulation*. John Wiley & Sons, 2017.
- [138] Skjalg E Haaland. Simple and explicit formulas for the friction factor in turbulent pipe flow. 1983.
- [139] George W Mulholland, RJ Samson, RD Mountain, and MH Ernst. Cluster size distribution for free molecular agglomeration. *Energy & Fuels*, 2(4):481–486, 1988.
- [140] Jérôme Yon, A Bescond, and F-X Ouf. A simple semi-empirical model for effective density measurements of fractal aggregates. *Journal of Aerosol Science*, 87:28–37, 2015.
- [141] Jenny Rissler, Maria E Messing, Azhar I Malik, Patrik T Nilsson, Erik Z Nordin, Mats Bohgard, Mehri Sanati, and Joakim H Pagels. Effective density characterization of soot agglomerates from various sources and comparison to aggregation theory. *Aerosol Science and Technology*, 47(7):792–805, 2013.
- [142] Anna Ciajolo, Rosalba Barbella, Antonio Tregrossi, and Loretta Bonfanti. Spectroscopic and compositional signatures of pah-loaded mixtures in the soot inception region of a premixed ethylene flame. In *Symposium (International) on Combustion*, volume 27, pages 1481–1487. Elsevier, 1998.
- [143] Christopher Betrancourt, Fengshan Liu, Pascale Desgroux, Xavier Mercier, Alessandro Faccinetto, Maurin Salamanca, Lena Ruwe, Katharina Kohse-Höinghaus, Daniel Emmrich, André Beyer, et al. Investigation of the size of the incandescent incipient soot particles in premixed sooting and nucleation flames of n-butane using lii, him, and 1 nm-smpls. *Aerosol Science and Technology*, 51(8):916–935, 2017.
- [144] Nikolaj A Fuchs, RE Daisley, Marina Fuchs, CN Davies, and ME Straumanis. The mechanics of aerosols, 1965.

- [145] Jin Jwang Wu and Richard C Flagan. A discrete-sectional solution to the aerosol dynamic equation. *Journal of Colloid and interface Science*, 123(2):339–352, 1988.
- [146] BS Haynes and H Gg Wagner. The surface growth phenomenon in soot formation. *Zeitschrift für Physikalische Chemie*, 133(2):201–213, 1982.
- [147] Stephen J Harris and Anita M Weiner. Chemical kinetics of soot particle growth. *Annual Review of Physical Chemistry*, 36(1):31–52, 1985.
- [148] KH Homann. Formation of large molecules, particulates and ions in premixed hydrocarbon flames; progress and unresolved questions. In *Symposium (International) on Combustion*, volume 20, pages 857–870. Elsevier, 1985.
- [149] Armin Veshkini. *Understanding Soot Particle Growth Chemistry and Particle Sizing Using a Novel Soot Growth and Formation Model*. University of Toronto (Canada), 2015.
- [150] K Olof Johansson, Tyler Dillstrom, Matteo Monti, Farid El Gabaly, Matthew F Campbell, Paul E Schrader, Denisia M Popolan-Vaida, Nicole K Richards-Henderson, Kevin R Wilson, Angela Violi, et al. Formation and emission of large furans and oxygenated hydrocarbons from flames. *Proceedings of the National Academy of Sciences*, 113(30):8374–8379, 2016.
- [151] J Houston Miller, W Gary Mallard, and Kermit C Smyth. Intermolecular potential calculations for polycyclic aromatic hydrocarbons. *The Journal of Physical Chemistry*, 88(21):4963–4970, 1984.
- [152] Yoichiro Araki, Yoshiya Matsukawa, Yasuhiro Saito, Yohsuke Matsushita, Hideyuki Aoki, Koki Era, and Takayuki Aoki. Effects of carrier gas on the properties of soot produced by ethylene pyrolysis. *Fuel Processing Technology*, 213:106673, 2021.
- [153] Binxuan Sun, Stelios Rigopoulos, and Anxiong Liu. Modelling of soot coalescence and aggregation with a two-population balance equation model and a conservative finite volume method. *Combustion and Flame*, 229:111382, 2021.
- [154] A Tregrossi, A Ciajolo, and R Barbella. The combustion of benzene in rich premixed flames at atmospheric pressure. *Combustion and flame*, 117(3):553–561, 1999.
- [155] Eirini Goudeli, Maximilian L Eggersdorfer, and Sotiris E Pratsinis. Coagulation-agglomeration of fractal-like particles: Structure and self-preserving size distribution. *Langmuir*, 31(4):1320–1327, 2015.
- [156] M Reza Kholghy and Georgios A Kelesidis. Surface growth, coagulation and oxidation of soot by a monodisperse population balance model. *Combustion and Flame*, 227:456–463, 2021.
- [157] Srinivas Vemury and Sotiris E Pratsinis. Self-preserving size distributions of agglomerates. *Journal of Aerosol Science*, 26(2):175–185, 1995.
- [158] Laurent Fulcheri, Vandan-Julien Rohani, Elliott Wyse, Ned Hardman, and Enoch Dames. An energy-efficient plasma methane pyrolysis process for high yields of carbon black and hydrogen. *International Journal of Hydrogen Energy*, 48(8):2920–2928, 2023.
- [159] Yu Wang, Abhijeet Raj, and Suk Ho Chung. A pah growth mechanism and synergistic effect on pah formation in counterflow diffusion flames. *Combustion and flame*, 160(9):1667–1676, 2013.
- [160] Hanson research group shock tubes. <https://hanson.stanford.edu/our-approaches/shock-tubes>. Accessed: 2024-05-24.
- [161] DE Fussey, AJ Gosling, and D Lampard. A shock-tube study of induction times in the formation of carbon particles by pyrolysis of the c2 hydrocarbons. *Combustion and Flame*, 32:181–192, 1978.

- [162] Nicolas H Pinkowski, Yiming Ding, Sarah E Johnson, Yu Wang, Thomas C Parise, David F Davidson, and Ronald K Hanson. A multi-wavelength speciation framework for high-temperature hydrocarbon pyrolysis. *Journal of Quantitative Spectroscopy and Radiative Transfer*, 225:180–205, 2019.
- [163] Sean J Cassady, Rishav Choudhary, Nicolas H Pinkowski, Jiankun Shao, David F Davidson, and Ronald K Hanson. The thermal decomposition of ethane. *Fuel*, 268:117409, 2020.
- [164] Ivo Stranic and Ronald K Hanson. Laser absorption diagnostic for measuring acetylene concentrations in shock tubes. *Journal of Quantitative Spectroscopy and Radiative Transfer*, 142:58–65, 2014.
- [165] SC Lee and CL Tien. Optical constants of soot in hydrocarbon flames. In *Symposium (international) on combustion*, volume 18, pages 1159–1166. Elsevier, 1981.
- [166] G Blanquart, P Pepiot-Desjardins, and H Pitsch. Chemical mechanism for high temperature combustion of engine relevant fuels with emphasis on soot precursors. *Combustion and Flame*, 156(3):588–607, 2009.
- [167] TA Sipkens and SN Rogak. Using k-means to identify soot aggregates in transmission electron microscopy images. *Journal of Aerosol Science*, 152:105699, 2021.
- [168] Ramin Dastanpour, Jocelyne M Boone, and Steven N Rogak. Automated primary particle sizing of nanoparticle aggregates by tem image analysis. *Powder Technology*, 295:218–224, 2016.
- [169] Jason Olfert and Steven Rogak. Universal relations between soot effective density and primary particle size for common combustion sources. *Aerosol Science and Technology*, 53(5):485–492, 2019.
- [170] Mohsen Kazemimanesh, Ramin Dastanpour, Alberto Baldelli, Alireza Moallemi, Kevin A Thomson, Melina A Jefferson, Matthew R Johnson, Steven N Rogak, and Jason S Olfert. Size, effective density, morphology, and nano-structure of soot particles generated from buoyant turbulent diffusion flames. *Journal of Aerosol Science*, 132:22–31, 2019.
- [171] Ramin Dastanpour, Ali Momenimovahed, Kevin Thomson, Jason Olfert, and Steven Rogak. Variation of the optical properties of soot as a function of particle mass. *Carbon*, 124:201–211, 2017.
- [172] Brian Graves, Jason Olfert, Bronson Patychuk, Ramin Dastanpour, and Steven Rogak. Characterization of particulate matter morphology and volatility from a compression-ignition natural-gas direct-injection engine. *Aerosol Science and Technology*, 49(8):589–598, 2015.
- [173] Marco J Castaldi and SELIM M SENKAW. Pah formation in the premixed flame of ethane. *Combustion science and technology*, 116(1-6):167–181, 1996.
- [174] Bin Zhao, Kei Uchikawa, and Hai Wang. A comparative study of nanoparticles in premixed flames by scanning mobility particle sizer, small angle neutron scattering, and transmission electron microscopy. *Proceedings of the Combustion Institute*, 31(1):851–860, 2007.
- [175] Berk Öktem, Michael P Tolocka, Bin Zhao, Hai Wang, and Murray V Johnston. Chemical species associated with the early stage of soot growth in a laminar premixed ethylene–oxygen–argon flame. *Combustion and Flame*, 142(4):364–373, 2005.
- [176] Yoshiya Matsukawa, Kazuki Dewa, Koki Era, Takayuki Aoki, and Hideyuki Aoki. Experimental coalescence characteristic time of carbon nanoparticle produced from ethylene or benzene pyrolysis. *Chemical Engineering Research and Design*, 198:403–412, 2023.
- [177] H Kellerer, A Müller, H-J Bauer, and S Wittig. Soot formation in a shock tube under elevated pressure conditions. *Combustion science and technology*, 113(1):67–80, 1996.

- [178] V Gg Knorre, Dietmar Tanke, Th Thienel, and H Gg Wagner. Soot formation in the pyrolysis of benzene/acetylene and acetylene/hydrogen mixtures at high carbon concentrations. In *Symposium (international) on combustion*, volume 26, pages 2303–2310. Elsevier, 1996.

# Appendix A

# Derivation of Transport Equations

This chapter explains the derivation of transport equations from first principles for mass, species, energy and soot variables for the reactors employed in omnisooot. The conventional reactor transport equation have been derived for a reacting gas without solid particle [137], so we provide a step by step derivation of equations that describes transport/evolution of mass, species and energy of gas as well as those of soot variables.

## A.1 Constant Volume Reactor

### A.1.1 Continuity

The rate change of mass of gas mixture is equal to the production rate of soot.

$$\frac{d}{dt} (m) = V (1 - \varphi) \sum_i \dot{s}_i W_i,$$

where  $V$  is the reactor volume that stays constant during the process, and gas occupies a fraction of volume reactor without soot, so  $m = \rho V(1 - \varphi)$ .

$$\begin{aligned} \frac{d}{dt} (\rho V(1 - \varphi)) &= V (1 - \varphi) \sum_i \dot{s}_i W_i \\ &\Downarrow \\ \frac{d}{dt} (\rho(1 - \varphi)) &= (1 - \varphi) \sum_i \dot{s}_i W_i \end{aligned} \tag{A.1}$$

### A.1.2 Species

The rate change of mass of each species can be described as:

$$\frac{d}{dt} (m_k) = V (1 - \varphi) (\dot{\omega}_k + \dot{s}_k) W_k$$

The mass of each species is defined as the total gas mass multiplied by the mass fraction as

$$\frac{dY_k}{dt} \rho V(1 - \varphi) + Y_k \frac{d}{dt} (\rho V(1 - \varphi)) = V (1 - \varphi) (\dot{\omega}_k + \dot{s}_k) W_k$$

where the colored term can be substituted from Equation (A.1).

$$\frac{dY_k}{dt} \rho V(1 - \varphi) + Y_k \cancel{V(1 - \varphi)} \sum_i \dot{s}_i W_i = V (1 - \varphi) (\dot{\omega}_k + \dot{s}_k) W_k$$

$$\Downarrow \times \frac{1}{\rho V(1-\varphi)}$$

$$\frac{dY_k}{dt} = \frac{1}{\rho} \left[ (\dot{\omega}_k + \dot{s}_k) W_k - Y_k \sum_i \dot{s}_i W_i \right] \quad (\text{A.2})$$

### A.1.3 Energy

In the constant volume reactor, the internal energy is favorable since the external boundaries of the control volume are not changed, and the work from soot volume is neglected, so formulating the energy balance based on the internal energy is preferred. The energy passes through the boundaries of the control volume via soot generation and external heat source.

$$\begin{aligned} \frac{dE}{dt} &= -\frac{dE_{soot}}{dt} + \dot{Q} \\ \Downarrow E &= m \sum Y_k e_k \\ \frac{dm}{dt} \sum_k Y_k e_k + m \sum_k \frac{dY_k}{dt} e_k + m \sum_k Y_k \frac{de_k}{dt} &= -\frac{dE_{soot}}{dt} + \dot{Q} \\ \Downarrow \text{from continuity} \\ V(1-\varphi) \sum_i \dot{s}_i W_i \sum_k Y_k e_k + m \sum_k \frac{dY_k}{dt} e_k + m \sum_k Y_k \frac{de_k}{dt} &= -\frac{dE_{soot}}{dt} + \dot{Q} \\ \Downarrow \text{from species} \\ V(1-\varphi) \sum_i \dot{s}_i W_i \sum_k Y_k e_k + m \sum_k \frac{1}{\rho} \left[ (\dot{\omega}_k + \dot{s}_k) W_k - Y_k \sum_i \dot{s}_i W_i \right] e_k + m \sum_k Y_k \frac{de_k}{dt} &= -\frac{dE_{soot}}{dt} + \dot{Q} \\ \Downarrow Y_k \frac{de_k}{dt} &= Y_k c_{c,k} \frac{dT}{dt} \\ \Downarrow \sum_k Y_k c_{c,k} &= c_p \\ V(1-\varphi) \sum_i \dot{s}_i W_i \sum_k Y_k e_k + m \sum_k \frac{1}{\rho} \left[ (\dot{\omega}_k + \dot{s}_k) W_k - Y_k \sum_i \dot{s}_i W_i \right] e_k + m c_v \frac{dT}{dt} &= -\frac{dE_{soot}}{dt} + \dot{Q} \\ \Downarrow \frac{dE_{soot}}{dt} &= \left( \rho_{soot} c_{v,soot} \varphi \frac{dT}{dt} - (1-\varphi) \sum_i \dot{s}_i W_i e_{soot} \right) V \\ V(1-\varphi) \sum_i \dot{s}_i W_i \sum_k Y_k e_k + m \sum_k \frac{1}{\rho} \left[ (\dot{\omega}_k + \dot{s}_k) W_k - Y_k \sum_i \dot{s}_i W_i \right] e_k + m c_v \frac{dT}{dt} &= \\ - \left( \rho_{soot} c_{v,soot} \varphi \frac{dT}{dt} - (1-\varphi) \sum_i \dot{s}_i W_i e_{soot} \right) V + \dot{Q} & \end{aligned}$$

$$\Downarrow m = \rho V(1-\varphi)$$

$$\begin{aligned}
& V(1-\varphi) \sum_i \dot{s}_i W_i \sum_k Y_k e_k + V(1-\varphi) \sum_k (\dot{\omega}_k + \dot{s}_k) W_k e_k - V(1-\varphi) \sum_k Y_k e_k \sum_i \dot{s}_i W_i \\
& + \rho V(1-\varphi) c_v \frac{dT}{dt} = - \left( \rho_{soot} c_{v,soot} \varphi \frac{dT}{dt} - (1-\varphi) \sum_i \dot{s}_i W_i e_{soot} \right) V + \dot{Q} \\
& \Downarrow \text{Eliminating } V(1-\varphi) \sum_i \dot{s}_i W_i \sum_k Y_k e_k \\
& \Downarrow \times 1/V \\
& (1-\varphi) \sum_k (\dot{\omega}_k + \dot{s}_k) W_k e_k + \rho(1-\varphi) c_v \frac{dT}{dt} = - \rho_{soot} c_{v,soot} \varphi \frac{dT}{dt} + \\
& (1-\varphi) \sum_i \dot{s}_i W_i e_{soot} + \dot{Q} \\
& \Downarrow \\
& (\rho(1-\varphi) c_v + \rho_{soot} c_{v,soot} \varphi) \frac{dT}{dt} = - (1-\varphi) \sum_k e_k (\dot{\omega}_k + \dot{s}_k) W_k + (1-\varphi) \sum_i \dot{s}_i W_i e_{soot} + \frac{\dot{Q}}{V} \\
& \Downarrow \\
& \frac{dT}{dt} = \frac{1}{\rho(1-\varphi) c_v + \rho_{soot} c_{v,soot} \varphi} \left[ - (1-\varphi) \sum_k e_k (\dot{\omega}_k + \dot{s}_k) W_k + (1-\varphi) \sum_i \dot{s}_i W_i e_{soot} + \frac{\dot{Q}}{V} \right] \quad (\text{A.3})
\end{aligned}$$

#### A.1.4 Soot Variables

The derivation of equations for soot variables can be accomplished similar to species evolution.

$$\frac{d}{dt} (m\psi) = \rho V(1-\varphi) S_\psi$$

$\Downarrow$

$$\frac{d}{dt} (\rho V(1-\varphi\psi)) = \rho V(1-\varphi) S_\psi$$

$\Downarrow \times 1/V$

$$\rho(1-\varphi) \frac{d\psi}{dt} + \psi \frac{d}{dt} (\rho(1-\varphi)) = \rho(1-\varphi) S_\psi$$

$\Downarrow$  from continuity

$$\begin{aligned}
\rho(1-\varphi) \frac{d\psi}{dt} + \psi V(1-\varphi) \sum_i \dot{s}_i W_i &= \rho(1-\varphi) S_\psi \\
\Downarrow \times \frac{1}{\rho(1-\varphi)} \\
\frac{d\psi}{dt} &= S_\psi - \frac{1}{\rho} \left[ \psi \sum_i \dot{s}_i W_i \right]
\end{aligned} \tag{A.4}$$

## A.2 Plug Flow Reactor

### A.2.1 Continuity

The gas flow that passes through the cross-section of a differential element along the flow reactor is described as:

$$\begin{aligned}
\rho u A (1-\varphi) |_{z+dz} - \rho u A (1-\varphi) |_z &= Adz(1-\varphi) \sum_i \dot{s}_i W_i \\
\Downarrow \\
\rho u (1-\varphi) A &= Adz(1-\varphi) \sum_i \dot{s}_i W_i \\
\Downarrow \\
\frac{d}{dz} (\rho u (1-\varphi)) &= (1-\varphi) \sum_i \dot{s}_i W_i
\end{aligned} \tag{A.5}$$

### A.2.2 Momentum

$$\begin{aligned}
\frac{d}{dz} (\dot{m}u) &= -\frac{d}{dz} (P(1-\varphi)) - \tau_w \frac{P_c}{A} \\
\Downarrow \\
u \frac{d}{dz} (\dot{m}) + \dot{m} \frac{d}{dz} (u) &= -\frac{d}{dz} (P(1-\varphi)) - \tau_w \frac{1}{R_H} \\
\Downarrow \\
u(1-\varphi) \sum_i \dot{s}_i W_i + \rho u (1-\varphi) \frac{d}{dz} (u) &= -\frac{d}{dz} (P(1-\varphi)) - \frac{\tau_w}{R_H}
\end{aligned} \tag{A.6}$$

### A.2.3 Species

$$\frac{d}{dz} (m_k) = (1 - \varphi) (\dot{\omega}_k + \dot{s}_k) W_k$$

↓

$$\frac{d}{dz} (\rho u (1 - \varphi) Y_k) = (1 - \varphi) (\dot{\omega}_k + \dot{s}_k) W_k$$

↓

$$\rho u (1 - \varphi) \frac{dY_k}{dz} + Y_k \frac{d}{dz} (\rho u (1 - \varphi)) = (1 - \varphi) (\dot{\omega}_k + \dot{s}_k) W_k$$

↓ from Equation (A.5)

$$\rho u (1 - \varphi) \frac{dY_k}{dz} + Y_k (1 - \varphi) \sum_i \dot{\omega}_i W_i = (1 - \varphi) (\dot{\omega}_k + \dot{s}_k) W_k$$

↓ × 1/(ρ(1 - φ))

$$\frac{dY_k}{dz} = \frac{1}{\rho u (1 - \varphi)} \left[ (1 - \varphi) (\dot{\omega}_k + \dot{s}_k) W_k - Y_k (1 - \varphi) \sum_i \dot{s}_i W_i \right] \quad (\text{A.7})$$

### A.2.4 Energy

$$\frac{d}{dz} (\rho u (1 - \varphi) h) + \frac{d}{dz} (\rho u \varphi h_{soot}) = \dot{q}'$$

↓

$$\frac{dh}{dz} (\rho u (1 - \varphi)) + h \frac{d}{dz} (\rho u (1 - \varphi)) + \frac{d}{dz} (\rho u \varphi) h_{soot} + \frac{dh_{soot}}{dz} \rho u \varphi = \dot{q}'$$

$$\downarrow h = \sum_k Y_k h_k$$

$$\rho u (1 - \varphi) \frac{d}{dz} \left( \sum_k Y_k h_k \right) + h \frac{d}{dz} (\rho u (1 - \varphi)) + \frac{d}{dz} (\rho u \varphi) h_{soot} + \frac{dh_{soot}}{dz} \rho u \varphi = \dot{q}'$$

↓

$$\rho u (1 - \varphi) \sum_k \frac{dY_k}{dz} h_k + \rho u (1 - \varphi) \sum_k \frac{dh_k}{dz} Y_k + h \frac{d}{dz} (\rho u (1 - \varphi)) + \frac{d}{dz} (\rho u \varphi) h_{soot} + \frac{dh_{soot}}{dz} \rho u \varphi = \dot{q}'$$

$\Downarrow$  from Equation (A.5)&(A.7)

$$\rho u (1 - \varphi) \sum_k \frac{1}{\rho u} \left[ (\dot{\omega}_k + \dot{s}_k) W_k - Y_k \sum_i \dot{s}_i W_i \right] h_k + \rho u (1 - \varphi) \sum_k \frac{dh_k}{dz} Y_k + h \frac{d}{dz} \left( (1 - \varphi) \sum_i \dot{s}_i W_i \right) + \frac{d}{dz} (\rho u \varphi) h_{soot} + \frac{dh_{soot}}{dz} \rho u \varphi = \dot{q}'$$

$$\Downarrow \frac{dh_k}{dz} = c_{p,k} \frac{dT}{dz}$$

$$\Downarrow \sum_k Y_k c_{p,k} = c_p$$

$$\Downarrow \frac{dh_{soot}}{dz} = c_{p,soot} \frac{dT}{dz}$$

$$(1 - \varphi) \sum_k \left[ (\dot{\omega}_k + \dot{s}_k) W_k - Y_k \sum_i \dot{s}_i W_i \right] h_k + \rho u (1 - \varphi) c_p \frac{dT}{dz} + h (1 - \varphi) \sum_i \dot{s}_i W_i + \frac{d}{dz} (\rho u \varphi) h_{soot} + c_{p,soot} \frac{dT}{dz} \rho u \varphi = \dot{q}'$$

$\Downarrow$

$$(1 - \varphi) \sum_k [(\dot{\omega}_k + \dot{s}_k) W_k] h_k + \rho u (1 - \varphi) c_p \frac{dT}{dz} - (1 - \varphi) \sum_i \dot{s}_i W_i h_{soot} + c_{p,soot} \frac{dT}{dz} \rho u \varphi = \dot{q}'$$

$\Downarrow$

$$[\rho u (1 - \varphi) c_p + \rho u \varphi c_{p,soot}] \frac{dT}{dz} + (1 - \varphi) \sum_k [(\dot{\omega}_k + \dot{s}_k) W_k] h_k - (1 - \varphi) \sum_i \dot{s}_i W_i h_{soot} = \dot{q}'$$

$\Downarrow$

$$\frac{dT}{dz} = \frac{1}{\rho u (1 - \varphi) c_p + \rho u \varphi c_{p,soot}} \left[ - (1 - \varphi) \sum_k (\dot{\omega}_k + \dot{s}_k) W_k h_k + (1 - \varphi) \sum_i \dot{s}_i W_i h_{soot} + \dot{q}' \right]$$

## A.3 Perfectly Stirred Reactor

### A.3.1 Continuity

The mass conservation for the partially stirred reactor can be written as:

$$\frac{dm}{dt} = \dot{m}_{in} - \dot{m}_{out} + V (1 - \varphi) \sum_i \dot{s}_i W_i \quad (\text{A.8})$$

### A.3.2 Species

$$\frac{d}{dt} (m_k) = \dot{m}_{in} Y_k^* - \dot{m}_{out} Y_k + V (1 - \varphi) (\dot{\omega}_k + \dot{s}_k) W_k$$

$$\Downarrow m_k = m Y_k$$

$$Y_m \frac{dm}{dt} + m (Y_k) = \dot{m}_{in} Y_k^* - \dot{m}_{out} Y_k + V (1 - \varphi) (\dot{\omega}_k + \dot{s}_k) W_k$$

$\Downarrow$  from Equation A.8

$$\left( \dot{m}_{in} - \dot{m}_{out} + V (1 - \varphi) \sum_i \dot{s}_i W_i \right) Y_k + \frac{dY_k}{dt} m = \dot{m}_{in} Y_k^* - \dot{m}_{out} Y_k + V (1 - \varphi) (\dot{\omega}_k + \dot{s}_k) W_k$$

$$\Downarrow$$

$$V (1 - \varphi) Y_k \sum_i \dot{s}_i W_i + \frac{dY_k}{dt} m = \dot{m}_{in} (Y_k^* - Y_k) + V (1 - \varphi) (\dot{\omega}_k + \dot{s}_k) W_k$$

$$\Downarrow$$

$$\frac{dY_k}{dt} \rho V (1 - \varphi) = \dot{m}_{in} (Y_k^* - Y_k) + V (1 - \varphi) (\dot{\omega}_k + \dot{s}_k) W_k - V (1 - \varphi) Y_k \sum_i \dot{s}_i W_i$$

$$\Downarrow$$

$$\frac{dY_k}{dt} = \frac{\dot{m}_{in}}{\rho V (1 - \varphi)} (Y_k^* - Y_k) + \frac{1}{\rho} (\dot{\omega}_k + \dot{s}_k) W_k - \frac{1}{\rho} Y_k \sum_i \dot{s}_i W_i \quad (\text{A.9})$$

### A.3.3 Energy

$$\frac{dH}{dt} = \dot{m}_{in} h^* - \dot{m}_{out} h - \frac{dH_{soot}}{dt} + \dot{Q}$$

$$\Downarrow H = mh$$

$$\frac{dm}{dt} h + m \frac{dh}{dt} = \dot{m}_{in} h^* - \dot{m}_{out} h - \frac{dH_{soot}}{dt} + \dot{Q}$$

$\Downarrow$  from Equation A.8

$$\left( \dot{m}_{in} - \dot{m}_{out} + V (1 - \varphi) \sum_i \dot{s}_i W_i \right) h + m \frac{dh}{dt} = \dot{m}_{in} h^* - \dot{m}_{out} h - \frac{dH_{soot}}{dt} + \dot{Q}$$

$$\Downarrow$$

$$V(1-\varphi)h \sum_i \dot{s}_i W_i + m \frac{dh}{dt} = \dot{m}_{in}(h^* - h) - \frac{dH_{soot}}{dt} + \dot{Q}$$

↓

$$m \frac{dh}{dt} = \dot{m}_{in}(h^* - h) - V(1-\varphi)h \sum_i \dot{s}_i W_i - \frac{dH_{soot}}{dt} + \dot{Q}$$

$$\Downarrow h = \sum Y_k h_k$$

$$m \sum \frac{dY_k}{dt} h_k + m \sum \frac{dh_k}{dt} Y_k = \dot{m}_{in}(h^* - h) - V(1-\varphi)h \sum_i \dot{s}_i W_i - \frac{dH_{soot}}{dt} + \dot{Q}$$

↓ from Equation A.9

$$m \sum \left( \frac{\dot{m}_{in}}{\rho V(1-\varphi)} (Y_k^* - Y_k) + \frac{1}{\rho} (\dot{\omega}_k + \dot{s}_k) W_k - \frac{1}{\rho} Y_k \sum_i \dot{s}_i W_i \right) h_k + m \sum c_{p,k} \frac{dT}{dt} Y_k = \\ \dot{m}_{in}(h^* - h) - V(1-\varphi)h \sum_i \dot{s}_i W_i - \frac{dH_{soot}}{dt} + \dot{Q}$$

$$\Downarrow m = \rho V(1-\varphi)$$

$$\dot{m}_{in} \sum (Y_k^* - Y_k) h_k + V(1-\varphi) \sum (\dot{\omega}_k + \dot{s}_k) W_k h_k + mc_p \frac{dT}{dt} = \dot{m}_{in}(h^* - h) - \frac{dH_{soot}}{dt} + \dot{Q}$$

↓

$$\dot{m}_{in} \sum (Y_k^* - Y_k) h_k + V(1-\varphi) \sum (\dot{\omega}_k + \dot{s}_k) W_k h_k + mc_p \frac{dT}{dt} = \dot{m}_{in}(h^* - h) \\ - \left( \rho_{soot} c_{p,soot} \varphi V \frac{dT}{dt} - (1-\varphi) V \sum_i \dot{s}_i W_i h_{soot} \right) + \dot{Q}$$

↓

$$\dot{m}_{in} \sum (Y_k^* - Y_k) h_k + V(1-\varphi) \sum (\dot{\omega}_k + \dot{s}_k) W_k h_k + mc_p \frac{dT}{dt} = \dot{m}_{in}(h^* - h) \\ - \left( \rho_{soot} c_{p,soot} \varphi V \frac{dT}{dt} - (1-\varphi) V \sum_i \dot{s}_i W_i h_{soot} \right) + \dot{Q}$$

$$\Downarrow m = \rho V(1-\varphi)$$

$$\Downarrow \times 1/V$$

$$\begin{aligned}
& \dot{m}_{in} \sum (Y_k^* - Y_k) h_k + V (1 - \varphi) \sum (\dot{\omega}_k + \dot{s}_k) W_k h_k + \rho V (1 - \varphi) c_p \frac{dT}{dt} = \\
& \dot{m}_{in} (h^* - h) - \left( \rho_{soot} c_{p,soot} \varphi V \frac{dT}{dt} - (1 - \varphi) V \sum_i \dot{s}_i W_i h_{soot} \right) + \dot{Q} \\
& \Downarrow \\
& (\rho (1 - \varphi) c_p + \rho_{soot} c_{p,soot} \varphi) \frac{dT}{dt} = \frac{\dot{m}_{in}}{V} (h^* - h) - \frac{\dot{m}_{in}}{V} \sum (Y_k^* - Y_k) h_k \\
& - (1 - \varphi) \sum (\dot{\omega}_k + \dot{s}_k) W_k h_k + (1 - \varphi) \sum_i \dot{s}_i W_i h_{soot} + \frac{\dot{Q}}{V} \\
& \Downarrow \\
& \frac{dT}{dt} = \frac{1}{\rho (1 - \varphi) c_p + \rho_{soot} c_{p,soot} \varphi} \left[ \frac{\dot{m}_{in}}{V} (h^* - h) - \frac{\dot{m}_{in}}{V} \sum (Y_k^* - Y_k) h_k - (1 - \varphi) \sum (\dot{\omega}_k + \dot{s}_k) W_k h_k \right. \\
& \quad \left. + (1 - \varphi) \sum_i \dot{s}_i W_i h_{soot} + \frac{\dot{Q}}{V} \right] \tag{A.10}
\end{aligned}$$

## Appendix B

# Additional Results

### B.1 Methane pyrolysis data from Hanson Research Group

#### B.1.1 30% CH<sub>4</sub> dataset

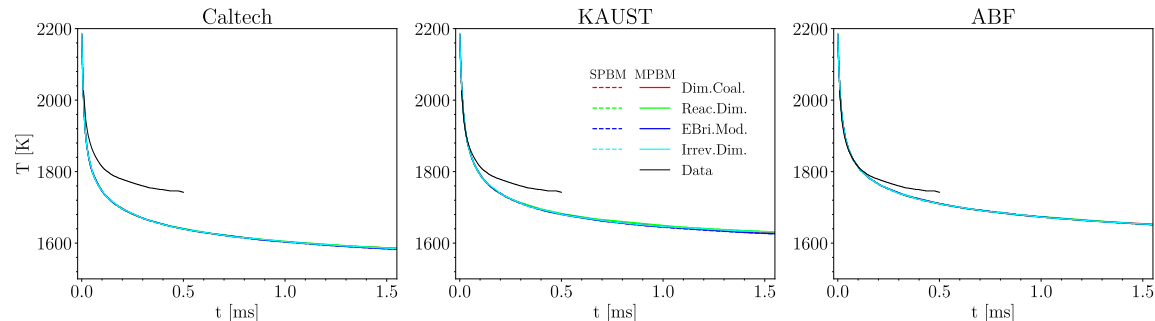


Figure B.1: The time history of temperature of 30% CH<sub>4</sub> pyrolysis at T=2184 K and P=3.62 atm using Caltech, KAUST, and ABF mechanisms and different PAH growth and particle dynamics models compared with the simulation results reported by Hanson Research Group

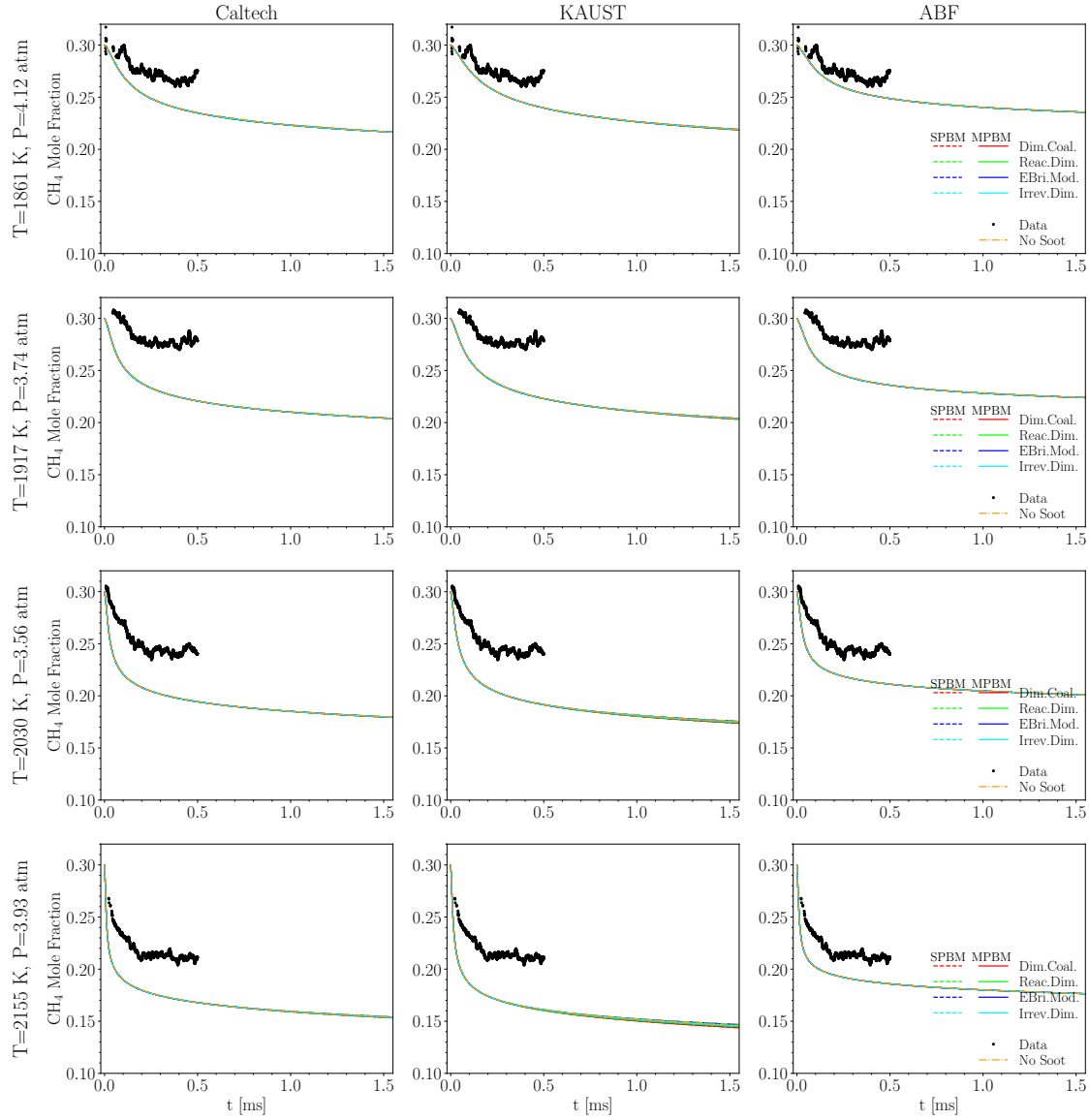


Figure B.2: The time history of CH<sub>4</sub> mole fraction of 30% CH<sub>4</sub> pyrolysis for 1861 K < T < 2155 K using Caltech, KAUST, and ABF mechanisms without soot (only chemistry) and with soot modeling described by different PAH growth and particle dynamics models compared with laser diagnostic data

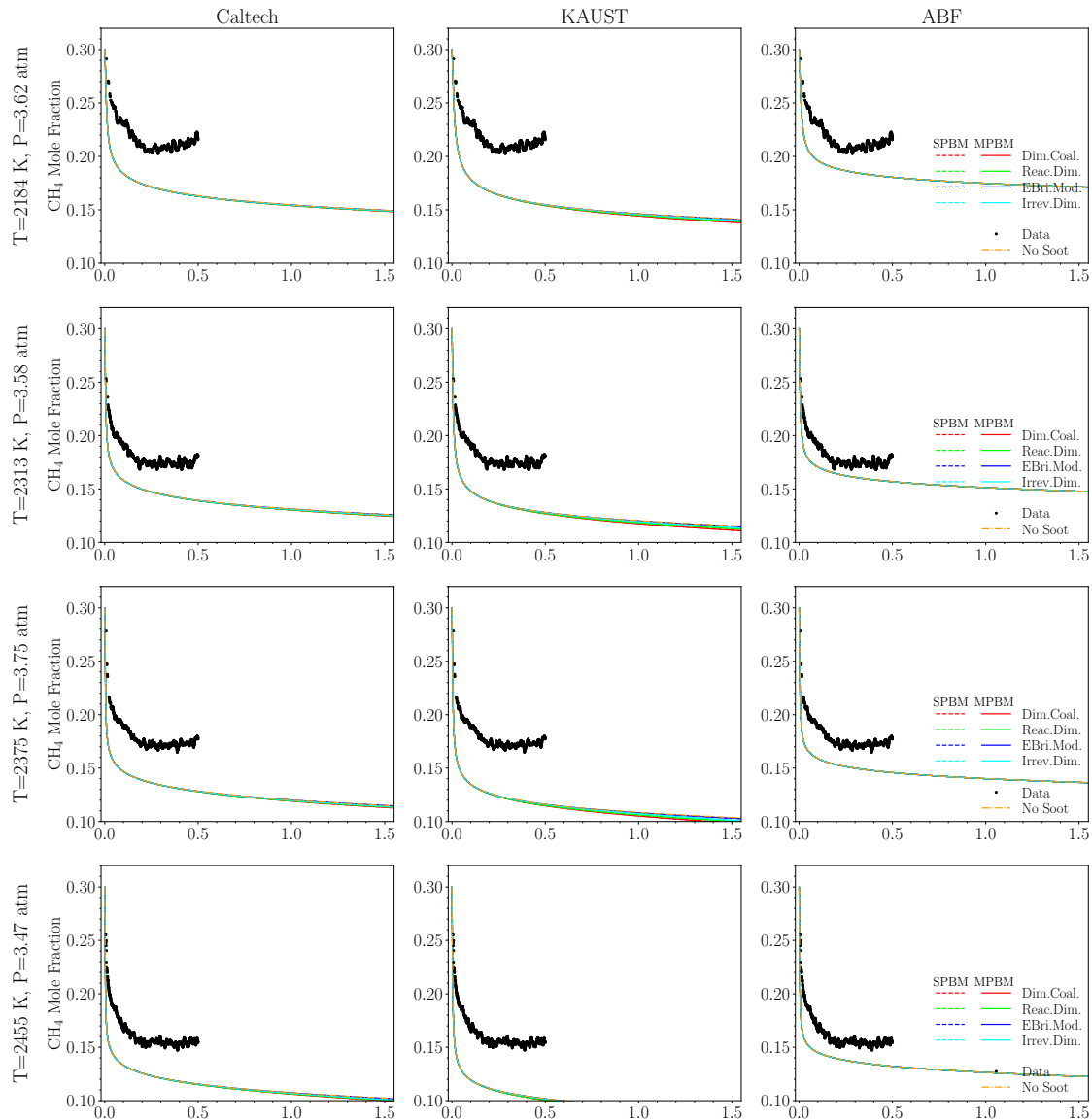


Figure B.3: The time history of CH<sub>4</sub> mole fraction of 30% CH<sub>4</sub> pyrolysis for 2184 K < T < 2455 K using Caltech, KAUST, and ABF mechanism without soot (only chemistry) and with soot modeling described by different PAH growth and particle dynamics models compared with laser diagnostic data

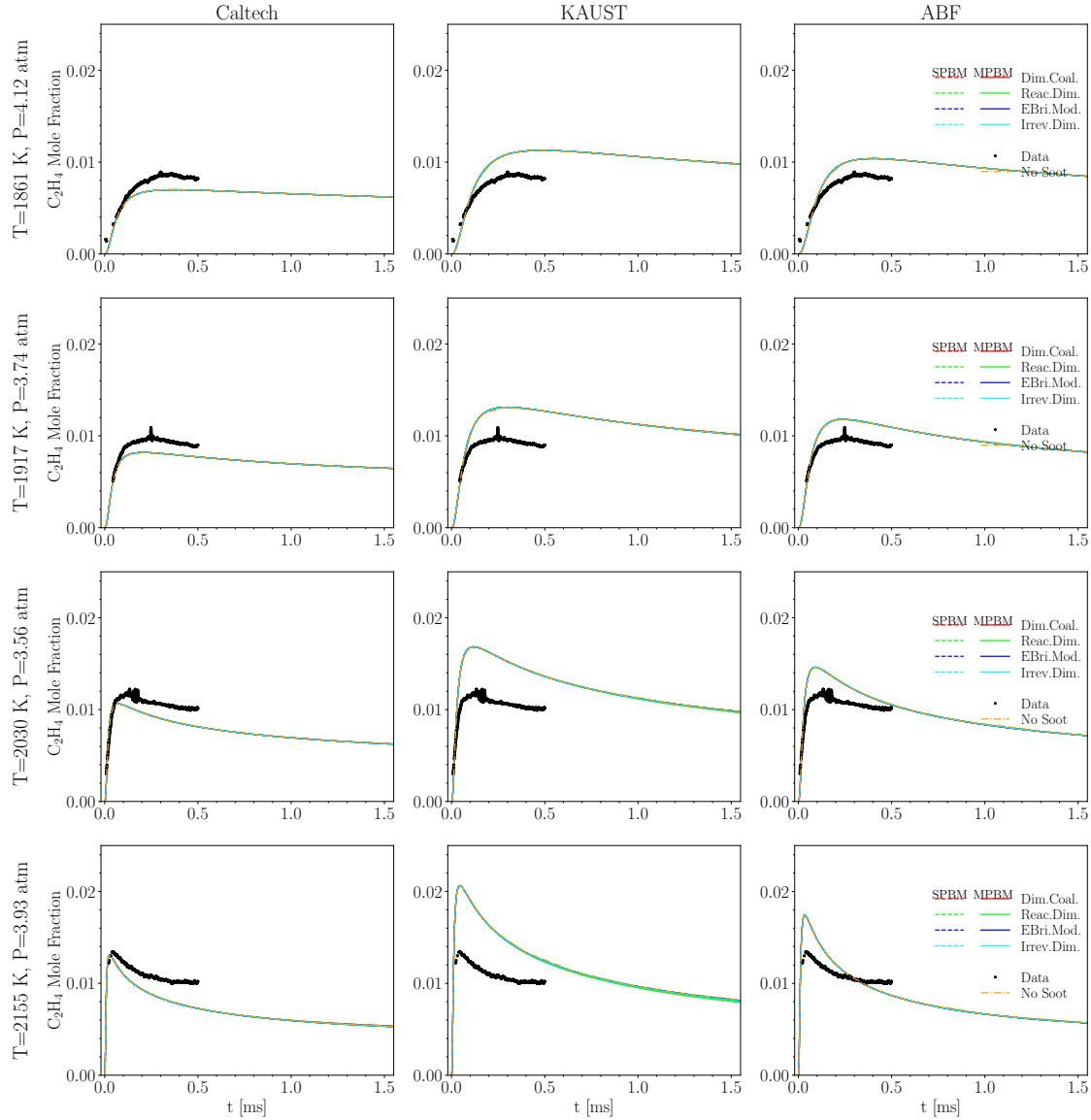


Figure B.4: The time history of C<sub>2</sub>H<sub>4</sub> mole fraction of 30% CH<sub>4</sub> pyrolysis for 1861 K < T < 2155 K using Caltech, KAUST, and ABF mechanisms without soot (only chemistry) and with soot modeling described by different PAH growth and particle dynamics models compared with laser diagnostic data

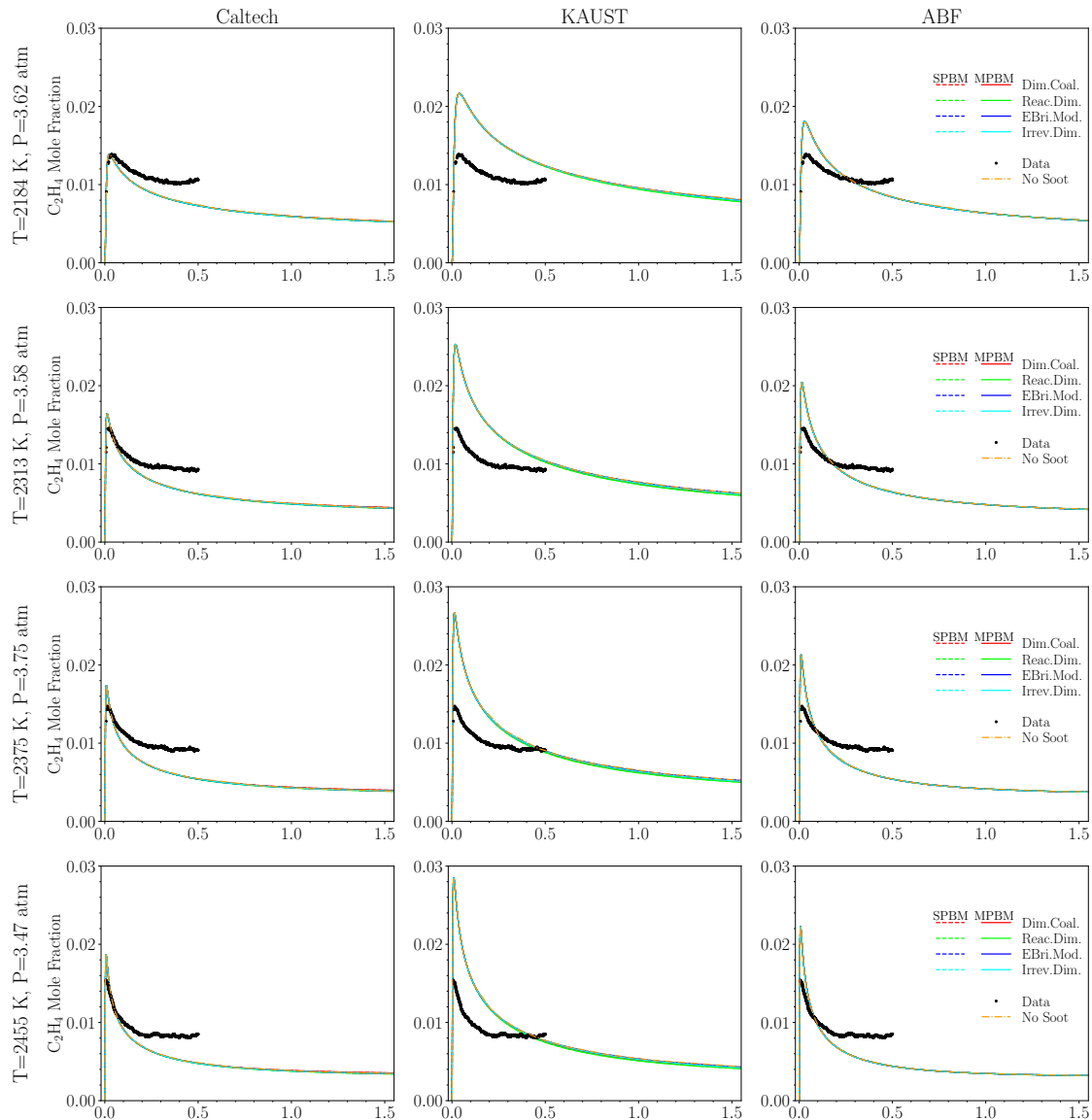


Figure B.5: The time history of  $\text{C}_2\text{H}_4$  mole fraction of 30%  $\text{CH}_4$  pyrolysis for  $2184 \text{ K} < T < 2455 \text{ K}$  using Caltech, KAUST, and ABF mechanism without soot (only chemistry) and with soot modeling described by different PAH growth and particle dynamics models compared with laser diagnostic data

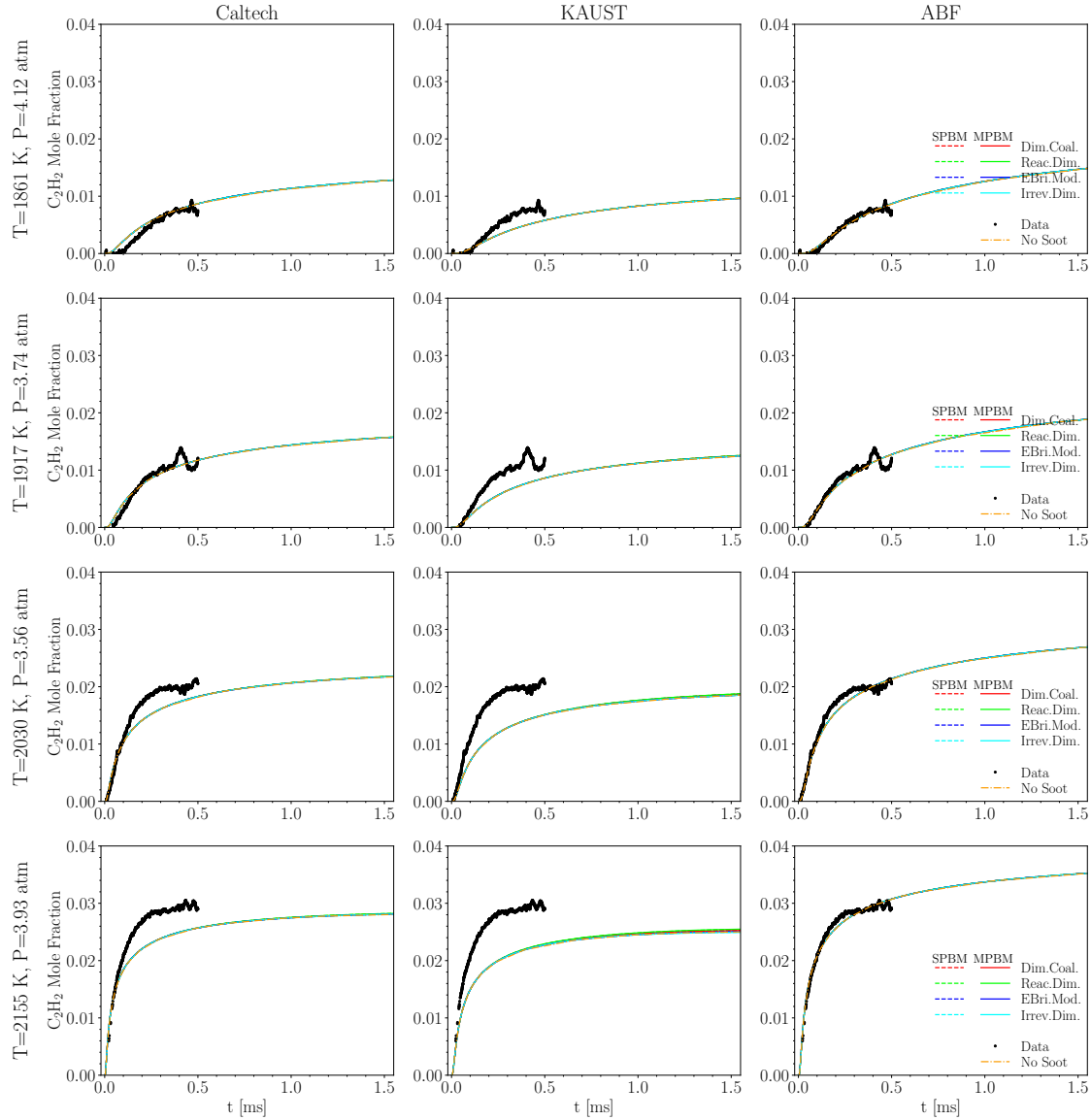


Figure B.6: The time history of  $\text{C}_2\text{H}_2$  mole fraction of 30%  $\text{CH}_4$  pyrolysis for  $1861 \text{ K} < T < 2155 \text{ K}$  using Caltech, KAUST, and ABF mechanisms without soot (only chemistry) and with soot modeling described by different PAH growth and particle dynamics models compared with laser diagnostic data

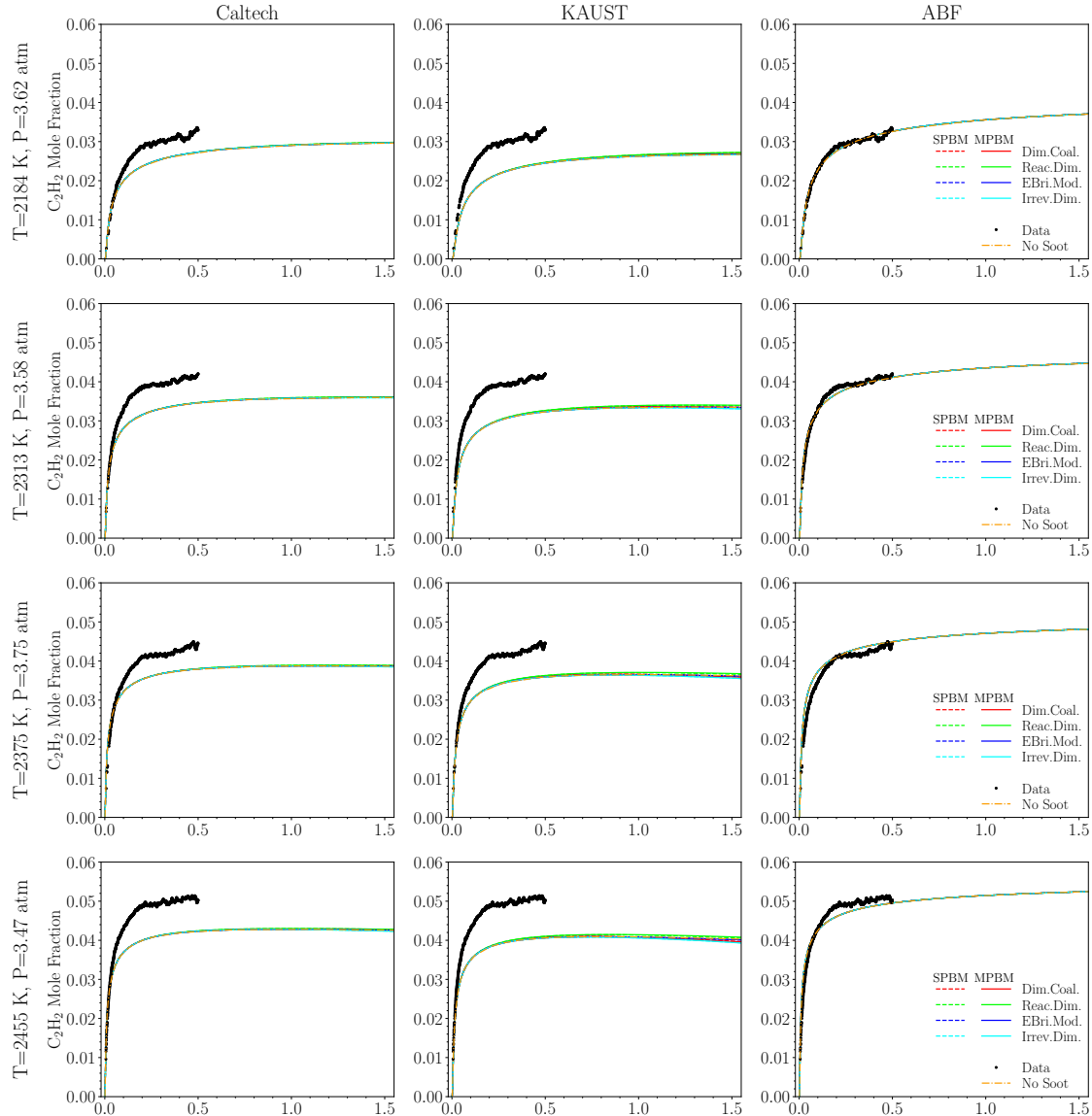


Figure B.7: The time history of  $\text{C}_2\text{H}_2$  mole fraction of 30%  $\text{CH}_4$  pyrolysis for  $2184 \text{ K} < T < 2455 \text{ K}$  using Caltech, KAUST, and ABF mechanism without soot (only chemistry) and with soot modeling described by different PAH growth and particle dynamics models compared with laser diagnostic data

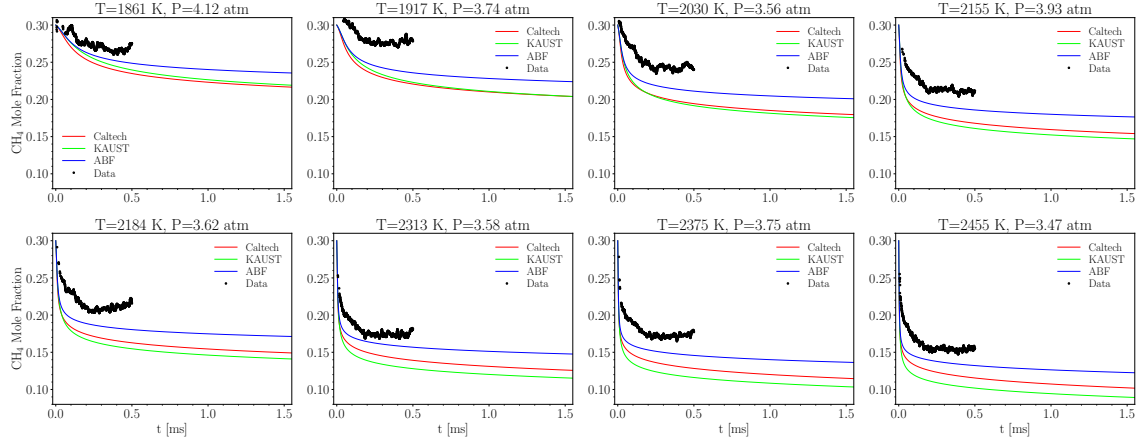


Figure B.8: The time history of  $\text{CH}_4$  mole fraction of 30%  $\text{CH}_4$  pyrolysis for  $1861 \text{ K} < T < 2455 \text{ K}$  using Caltech, KAUST, and ABF mechanisms without soot compared with laser diagnostic data

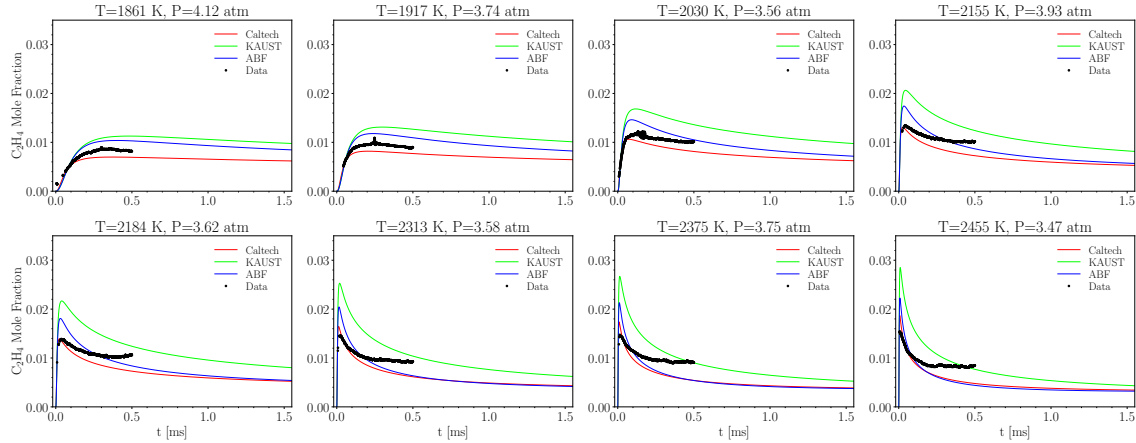


Figure B.9: The time history of  $\text{C}_2\text{H}_4$  mole fraction of 30%  $\text{CH}_4$  pyrolysis for  $1861 \text{ K} < T < 2455 \text{ K}$  using Caltech, KAUST, and ABF mechanisms without soot compared with laser diagnostic data

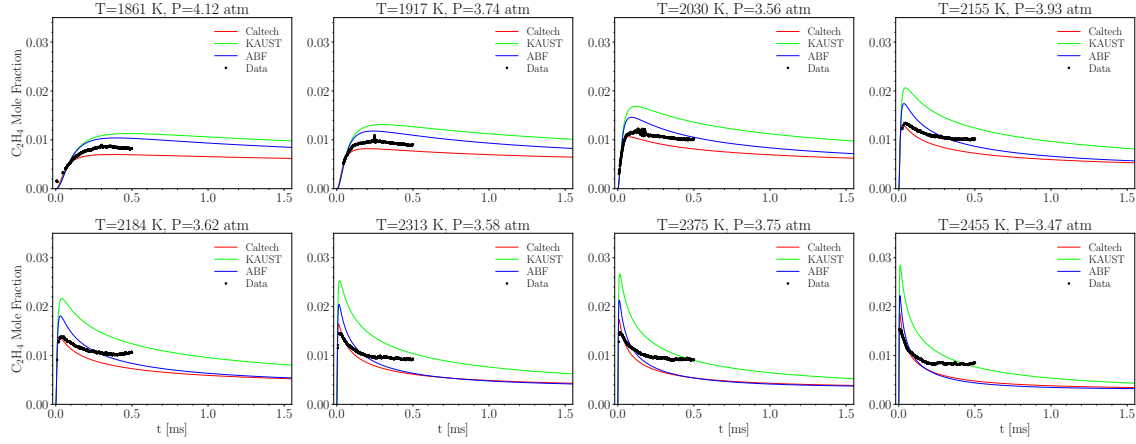


Figure B.10: The time history of  $\text{C}_2\text{H}_2$  mole fraction of 30%  $\text{CH}_4$  pyrolysis for  $1861 \text{ K} < T < 2455 \text{ K}$  using Caltech, KAUST, and ABF mechanisms without soot compared with laser diagnostic data

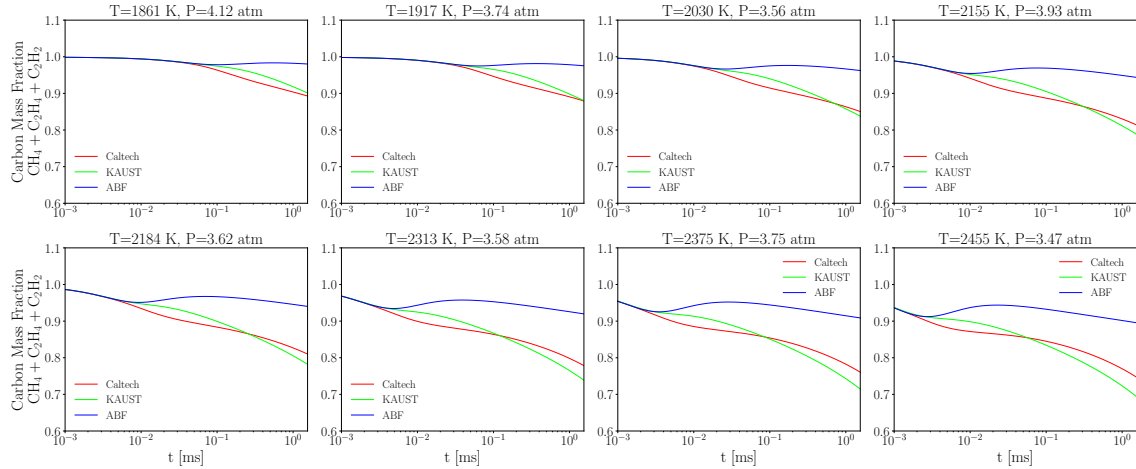


Figure B.11: The time history of carbon mass fraction of  $\text{CH}_4$ ,  $\text{C}_2\text{H}_4$ ,  $\text{C}_2\text{H}_2$  of 30%  $\text{CH}_4$  pyrolysis for  $1861 \text{ K} < T < 2455 \text{ K}$  using Caltech, KAUST, and ABF mechanisms without soot

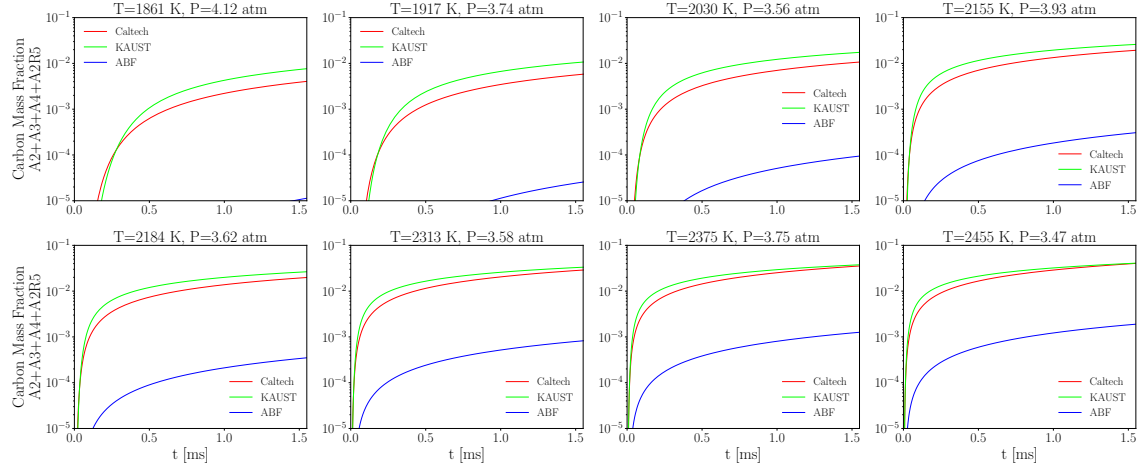


Figure B.12: The time history of carbon mass fraction of soot precursors, A2, A3, A4, and A2R5 of 30%  $\text{CH}_4$  pyrolysis for  $1861 \text{ K} < T < 2455 \text{ K}$  using Caltech, KAUST, and ABF mechanisms without soot

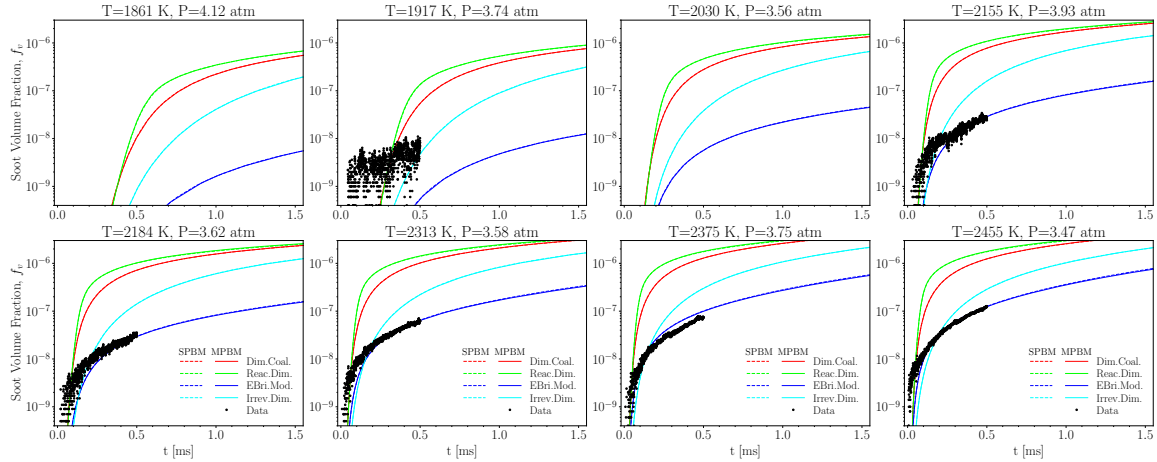


Figure B.13: The time history of soot volume fraction,  $f_v$  of 30%  $\text{CH}_4$  pyrolysis for  $1861 \text{ K} < T < 2455 \text{ K}$  using KAUST with different combinations of PAH growth and particle dynamics models compared with extinction measurements

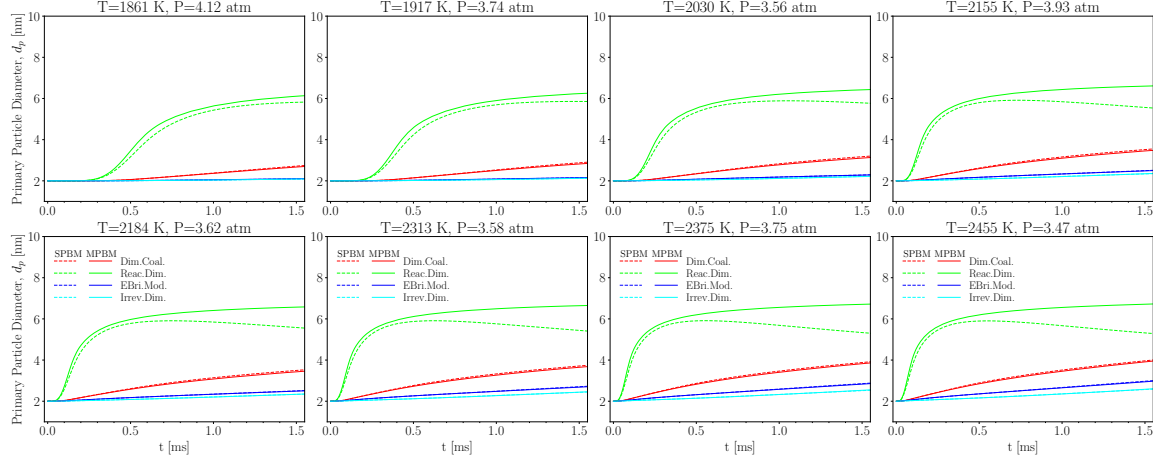


Figure B.14: The time history of primary particle diameter,  $d_p$  of 30%  $\text{CH}_4$  pyrolysis for 1861  $\text{K} < \text{T} < 2455 \text{ K}$  using KAUST with different combinations of PAH growth and particle dynamics models compared with extinction measurements

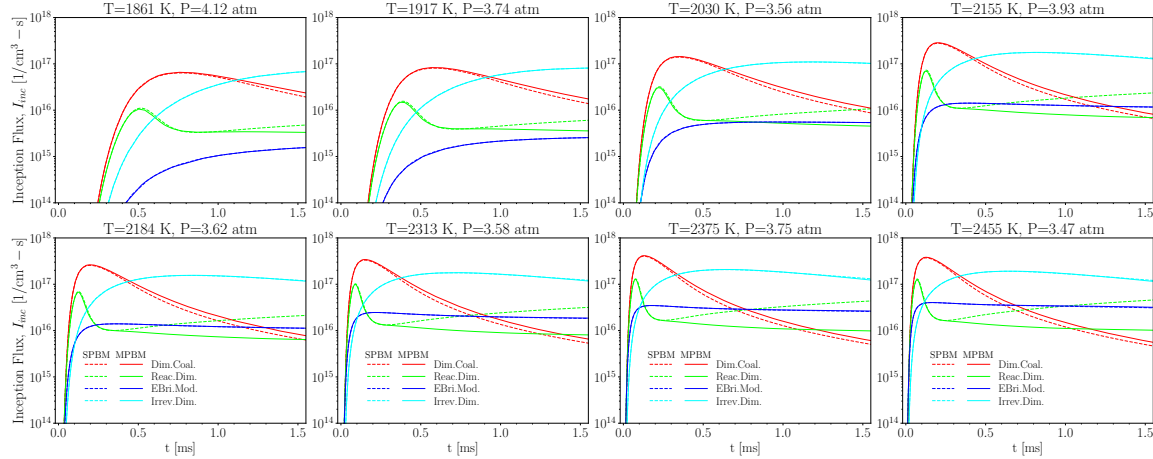


Figure B.15: The time history of inception flux,  $I_{inc}$  of 30%  $\text{CH}_4$  pyrolysis for 1861  $\text{K} < \text{T} < 2455 \text{ K}$  using KAUST with different combinations of PAH growth and particle dynamics models compared with extinction measurements

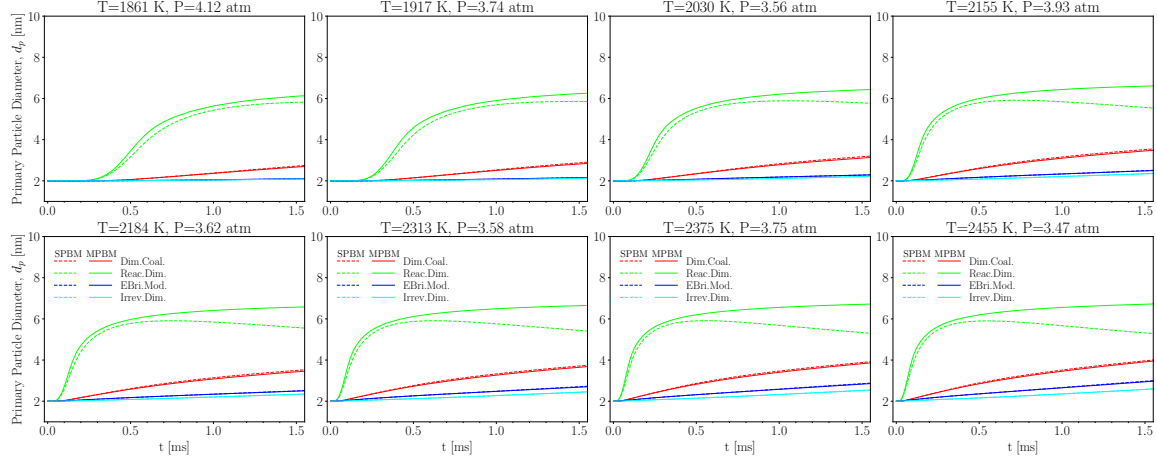


Figure B.16: The time history of mobility diameter,  $d_m$  of 30%  $\text{CH}_4$  pyrolysis for  $1861 \text{ K} < T < 2455 \text{ K}$  using KAUST with different combinations of PAH growth and particle dynamics models compared with extinction measurements

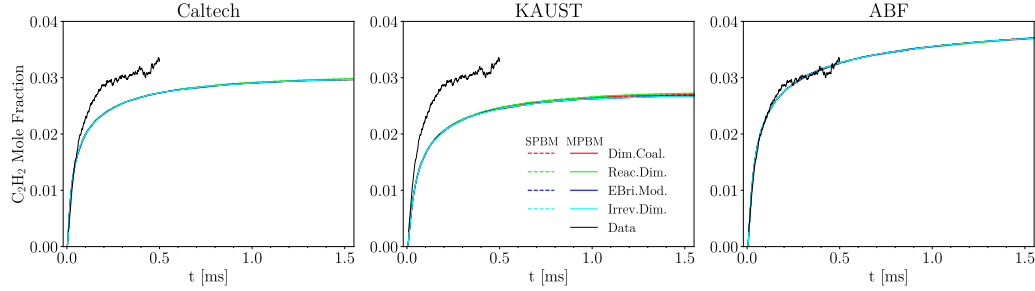


Figure B.17: The time history of  $\text{C}_2\text{H}_2$  mole fraction of 30%  $\text{CH}_4$  pyrolysis at  $T=2184 \text{ K}$  and  $P=3.62 \text{ atm}$  using Caltech, KAUST, and ABF mechanism and different PAH growth and particle dynamics models compared with laser diagnostic data

### B.1.2 10% $\text{CH}_4$ dataset

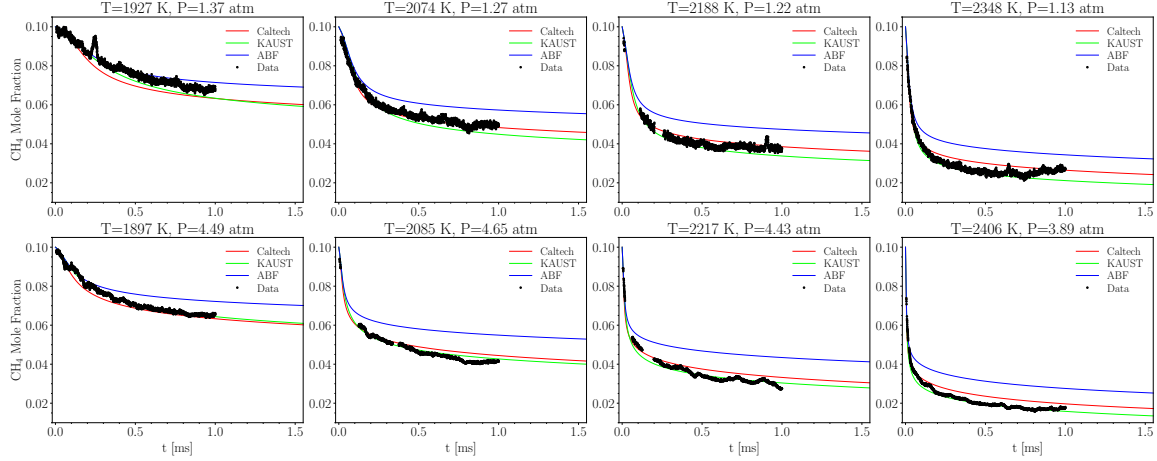


Figure B.18: The time history of  $\text{CH}_4$  mole fraction of 10%  $\text{CH}_4$  pyrolysis for  $1861 \text{ K} < T < 2455 \text{ K}$  using Caltech, KAUST, and ABF mechanisms without soot compared with laser diagnostic data

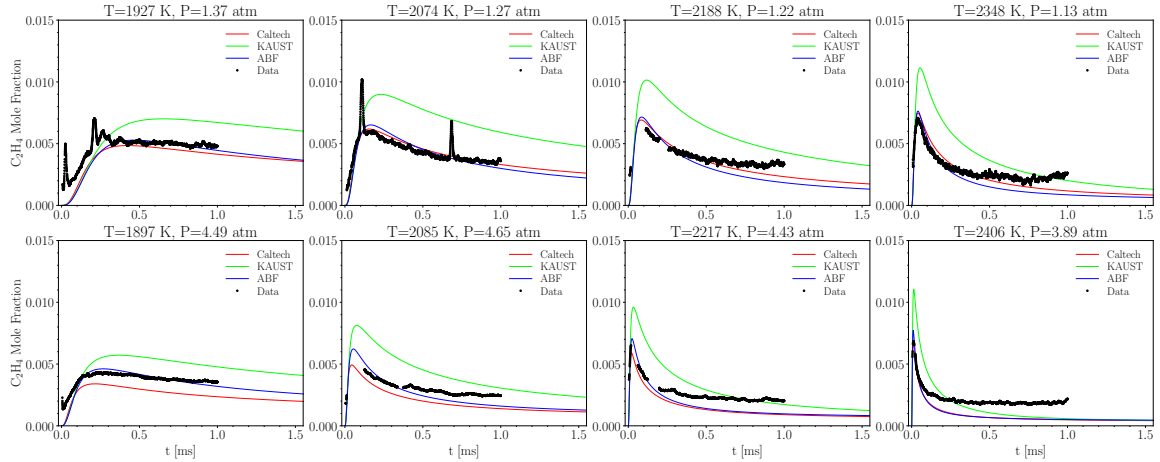


Figure B.19: The time history of  $\text{C}_2\text{H}_4$  mole fraction of 10%  $\text{CH}_4$  pyrolysis for  $1861 \text{ K} < T < 2455 \text{ K}$  using Caltech, KAUST, and ABF mechanisms without soot compared with laser diagnostic data

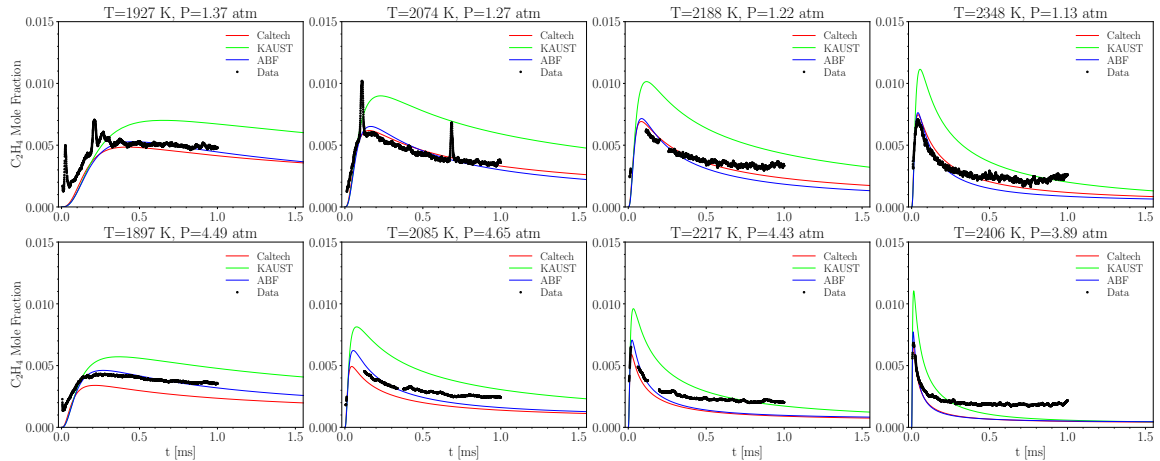


Figure B.20: The time history of  $\text{C}_2\text{H}_2$  mole fraction of 10%  $\text{CH}_4$  pyrolysis for  $1861 \text{ K} < T < 2455 \text{ K}$  using Caltech, KAUST, and ABF mechanisms without soot compared with laser diagnostic data

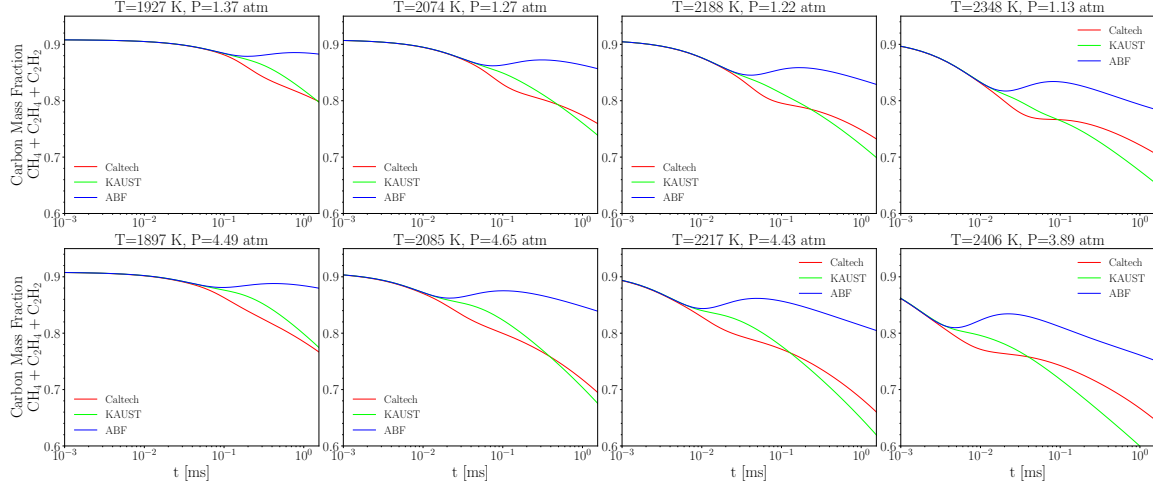


Figure B.21: The time history of carbon mass fraction of  $\text{CH}_4$ ,  $\text{C}_2\text{H}_4$ ,  $\text{C}_2\text{H}_2$  of 10%  $\text{CH}_4$  pyrolysis for  $1861 \text{ K} < T < 2455 \text{ K}$  using Caltech, KAUST, and ABF mechanisms without soot

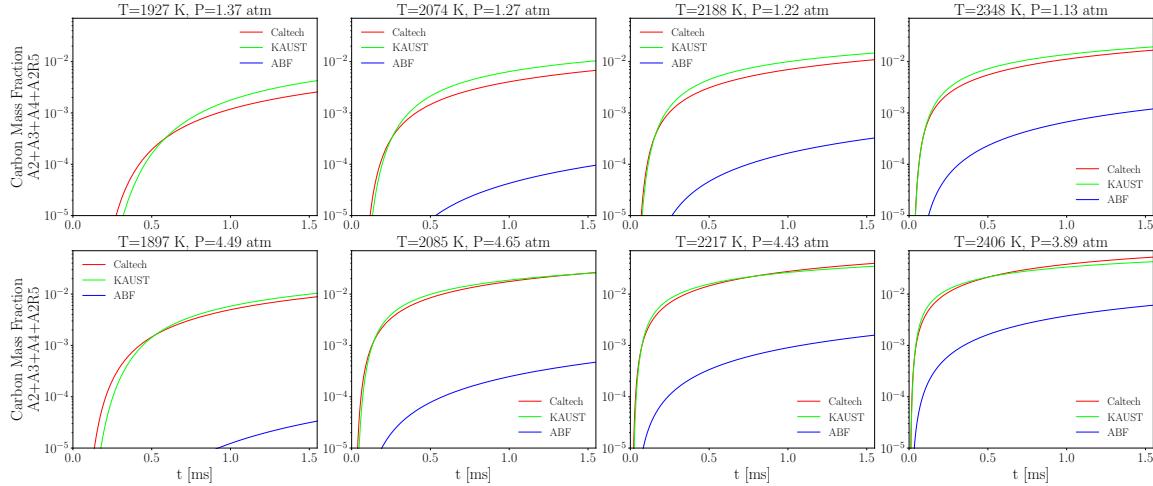


Figure B.22: The time history of carbon mass fraction of soot precursors,  $\text{A}_2$ ,  $\text{A}_3$ ,  $\text{A}_4$ , and  $\text{A}_2\text{R}_5$  of 10%  $\text{CH}_4$  pyrolysis for  $1861 \text{ K} < T < 2455 \text{ K}$  using Caltech, KAUST, and ABF mechanisms without soot

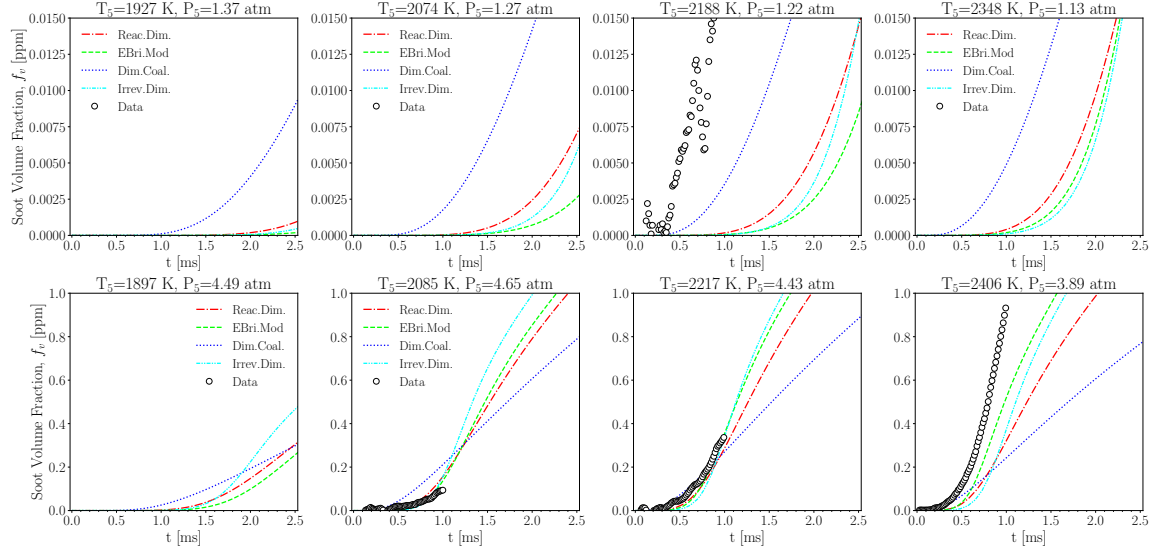


Figure B.23: The soot volume fraction,  $f_v$  over  $1800 \text{ K} < T < 2400 \text{ K}$  and  $P$  near 1 and 4 atm for 10%  $\text{CH}_4$  pyrolysis using KAUST, SPBM and optimized PAH growth models that minimizes  $f_v$  and  $d_p$  at  $T=2217$  and  $P=4.43$  atm

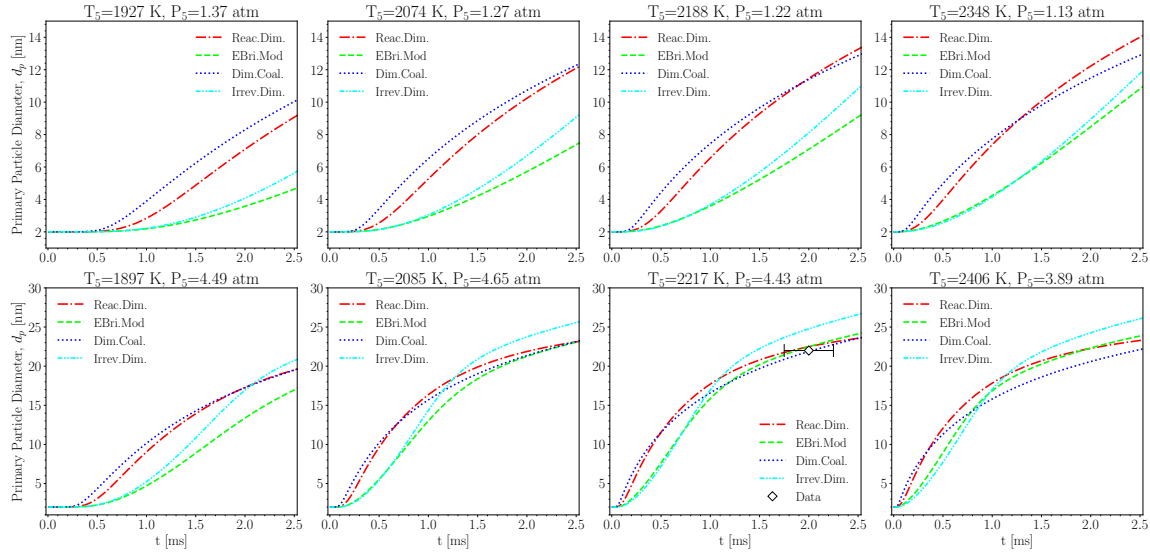


Figure B.24: The primary particle diameter,  $d_p$  over  $1800 \text{ K} < T < 2400 \text{ K}$  and  $P$  near 1 and 4 atm for 10%  $\text{CH}_4$  pyrolysis using KAUST, SPBM and optimized PAH growth models that minimizes  $f_v$  and  $d_p$  at  $T=2217$  and  $P=4.43$  atm

## B.2 Methane pyrolysis data of Agafonov et al. [1]

The pyrolysis of 5% and 10%  $\text{CH}_4$  diluted with Ar is investigated for the post-shock temperature range of 1800-3000 K and the pressure range of 4.7-7.1 bar. We assume the pressure linearly increase by temperature across the simulation cases. The obtained soot yields by were compared with the soot yield measured by Agafonov et al. [1] using a dual-beam absorption-emission technique. Agafonov et al. [1] reported yield  $\times E(m)$  at  $\lambda=632 \text{ nm}$ , and yield data was retrieved using  $E(m)=0.37$  suggested therein.

Figure B.25 depicts soot yield (SY) at  $t=1.5$  ms for 5% and 10%  $\text{CH}_4$  over the temperature range of 1800-3000 K using MPBM and SPBM and different inception model and Caltech [166] mechanism. Note that, the simulations were also performed using ABF [58] and KAUST [159] mechanisms, and the results were included in Appendix \*\*\*. The soot yield predictions exhibit a close agreement with measurements [1] considering the uncertainties in residence time from experiments. The model also successfully captures the bell-shape dependence of soot yield on temperature that has been observed in a variety of hydrocarbons in shock tube [177, 178]. The particle dynamics model has minimal effect on the predicted soot yield. In the vicinity of peak soot yield, SPBM results in slightly lower yield than MPBM, but they are indistinguishable in the rest of the temperature range.

In 5%  $\text{CH}_4$ , the SY peak temperature obtained from the model is slightly shifted towards higher temperatures ( $2300 \text{ K} < T_{peak} < 2400 \text{ K}$ ) compared to the measurements  $T_{peak} = 2200 \text{ K}$ . There are noticeable differences in the behavior of PAH growth model depending on the shock-tube initial temperature. When  $T < 2100 \text{ K}$ , Reactive Dimerization and EBridge Formation have the highest and lowest soot yield, respectively with Dimer Coalescence predicting soot yields that always falls between Reactive and Irreversible Dimerization. However, The soot yield of EBridge Formation rapidly rises with temperature and exceeds that of Reactive Dimerization and stays higher for the rest of temperature range.

The SY noticeably increases for higher initial  $\text{CH}_4$  mole fraction of 10% because more PAH and  $\text{C}_2\text{H}_2$  are formed leading to stronger carbon conversion rate to soot via inception and surface growth. The peak SY obtained from the model occurs in a higher temperature range 2600-2700 K compared to 5%  $\text{CH}_4$ . Soot yield trends can be better understood by examining carbon mass fraction of species directly contributing to soot mass. Figure B.26 depicts the bell-shape distribution of the carbon mass fraction of soot precursors (A2, A2R5, A3, and A4) over the studied temperature range. In low ( $T=1800 \text{ K}$ ) and high ( $T=2300 \text{ K}$ ) end of distribution, a low amount of precursors are formed resulting in low inception rates, particle number concentration and surface growth sites that reduces the soot yield. Additionally, 10%  $\text{CH}_4$  has a wider spread with peaks at higher temperature compared to 5%  $\text{CH}_4$  which explains the shift in peak yield temperature in Figure B.25. The effect of particle dynamics model is only noticeable in Reactive Dimerization where SPBM results in higher precursor CMF (lower consumption) due to its lower PAH adsorption rates.

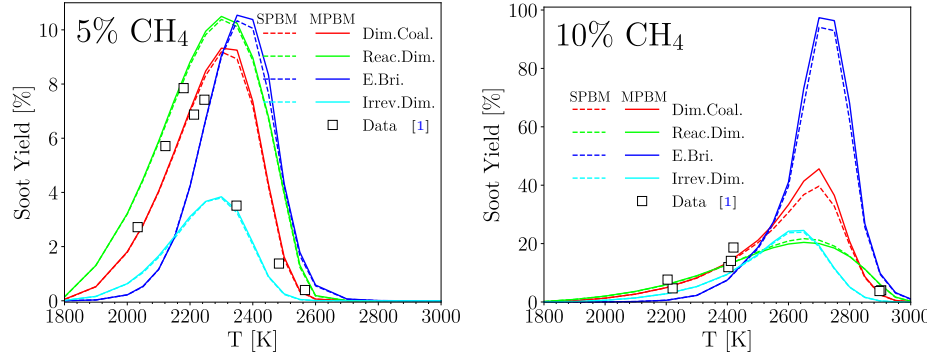


Figure B.25: The temperature dependence of soot yield during pyrolysis of 5%  $\text{CH}_4$ -Ar (left pane) and 10%  $\text{CH}_4$ -Ar (right pane) at  $P = 4.5\text{--}6.7$  bar obtained using Caltech mechanism and different inception models compared with measurements at 1.5ms [1] where the absorption function of  $E(m)=0.37$  is used to estimate soot yield.

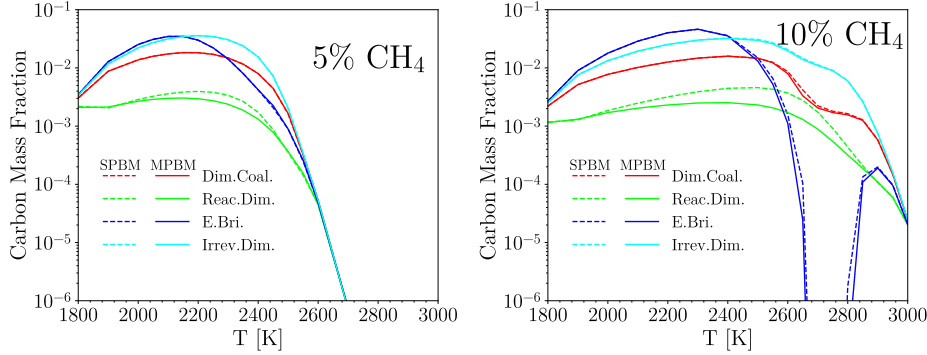


Figure B.26: The temperature dependence of carbon mass fraction of soot precursors (A2, A2R5, A3, and A4) combined during pyrolysis of 5% CH<sub>4</sub>-Ar (left pane) and 10% CH<sub>4</sub>-Ar (right pane) at P = 4.5–6.7 bar obtained using Caltech mechanism and different inception models at t=1.5 ms

EBridge Formation exhibits a similar behavior in %10 CH<sub>4</sub> simulations where it starts with the lowest SY at T<2500 K and then quickly increases reaching its peak at 100% which is significantly larger than other PAH growth models. The remarkable drop in carbon mass fraction of precursors with EBridge Formation corresponds to %100 yield meaning that all gaseous carbon including the precursors are directed towards soot particles. The higher precursor CMF with Irreversible Dimerization near the peak yield temperature region (2200–2400 K for %5 CH<sub>4</sub> and 2600–2800 K for %10 CH<sub>4</sub>) indicates less consumption of precursors via inception and PAH adsorption.

Figure B.27 shows the CMF of C<sub>2</sub>H<sub>2</sub> that has an overall increasing trend in the temperature range, but it reaches a plateau for %5 CH<sub>4</sub>. There is also a remarkable drop in C<sub>2</sub>H<sub>2</sub> CMF in 2600–2800 K due to strong mass growth rate of soot particles that drains C<sub>2</sub>H<sub>2</sub> from the gas mixture leading to high soot yield ≈ 100%.

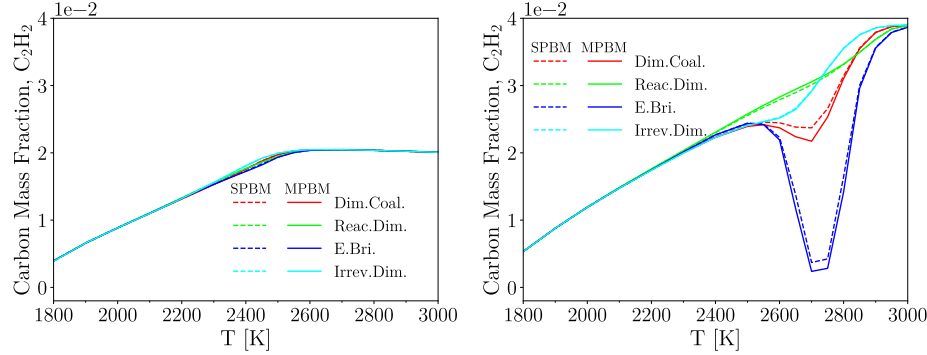


Figure B.27: The temperature dependence of carbon mass fraction of C<sub>2</sub>H<sub>2</sub> during pyrolysis of 5% CH<sub>4</sub>-Ar (left pane) and 10% CH<sub>4</sub>-Ar (right pane) at P = 4.5–6.7 bar obtained using Caltech mechanism and different inception models at t=1.5 ms

Although soot yield, and precursor and acetylene CMF are not sensitive to particle dynamics model, there is a significant difference in agglomerate morphology between SPBM and MPBM predictions. Fig. B.28 shows the average number of primary particles per agglomerate, which is larger for SPBM by the maximum factor of 5 for EBridge Formation and Dimer Coalescence in 10% CH<sub>4</sub>. SPBM predicts larger agglomerates due to accounting for polydispersity of particles that results in higher overall collision rate and faster growth by coagulation. n<sub>p</sub> follows a bell-shape trend similar to soot yield (Fig. B.25). The n<sub>p</sub> values and the difference between the particle dynamics models reaches their maximum in 2200–2400 K for %5 CH<sub>4</sub> and 2600–2800 K for %10 CH<sub>4</sub> because of a stronger inception flux leading to larger number concentration of particles and higher coagulation rate. n<sub>p</sub> is larger for Dimer Coalescence and EBridge Formation reaching the maximum of nearly

100 and 1000 in %5 and %10 CH<sub>4</sub>, respectively using SPBM. The effect of particle dynamics is minimum for Reactive and Irreversible Dimerization at 5% CH<sub>4</sub> over the whole temperature range.

Fig.B.29 shows the standard geometric deviation of mobility diameter,  $\sigma_g$  obtained by SPBM that reaches the maximum of 5 and 10 for %5 and %10 CH<sub>4</sub>, respectively indicating a significant degree of polydispersity in the generated particles at t=1.5ms.

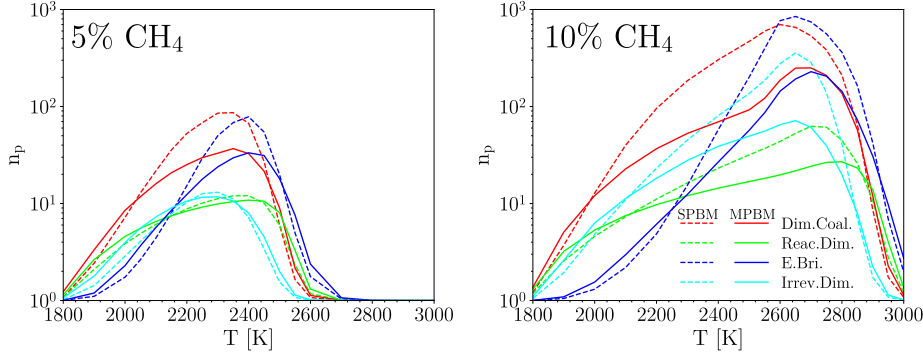


Figure B.28: The temperature dependence of average number of primary particle per agglomerate,  $n_p$  during pyrolysis of 5% CH<sub>4</sub>-Ar (left pane) and 10% CH<sub>4</sub>-Ar (right pane) at P = 4.5–6.7 bar obtained using Caltech mechanism and different inception models at t=1.5 ms

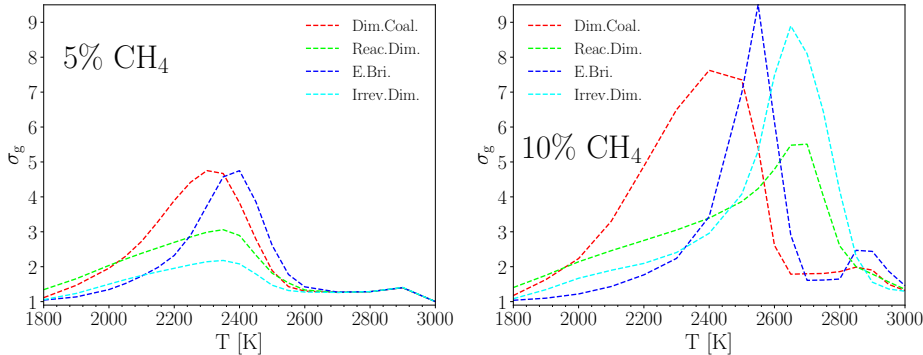


Figure B.29: The time variation of standard geometric deviation of mobility diameter,  $\sigma_g$  during pyrolysis of 5% CH<sub>4</sub>-Ar (left pane) and 10% CH<sub>4</sub>-Ar (right pane) at P = 4.5–6.7 bar obtained using Caltech mechanism and different inception models at t=1.5 ms

The  $\sigma_g$  values from the SMPS measurements of soot particles at t≈45ms in a benchmark burner-stabilized premixed are close to 1.1, which is significantly lower than values observed here. So, the evolution of  $\sigma_g$  in the studied shock tube is examined in an extended time frame up to 4 msf for 10% CH<sub>4</sub> at T=2500 and 2700 K. As shown in Fig.B.30, for all PAH growth models  $\sigma_g$  rises in the beginning due to simultaneous inception and coagulation that increases polydispersity and rapidly drops and approaches 1.5 before t=3ms when coagulation becomes dominant and inception weaken due to consumption of precursors by PAH adsorption and HACA.

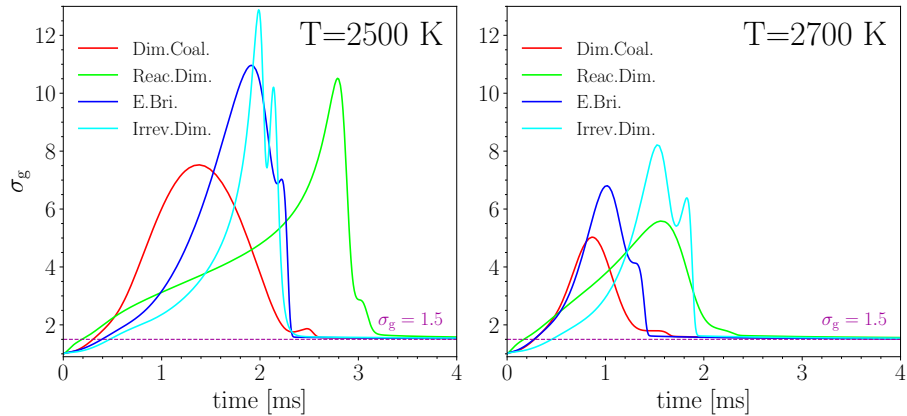


Figure B.30: The temperature dependence of standard geometric deviation of mobility diameter,  $\sigma_g$  during pyrolysis of 10% CH<sub>4</sub>-Ar at T=2500 K (left pane) and T=2700 K (right pane)